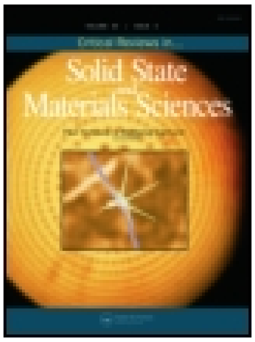

Critical Reviews in Solid State and Materials Sciences

ISSN: 1040-8436 (Print) 1547-6561 (Online) Journal homepage: http://www.tandfonline.com/loi/bsms20

Recent Advances in Friction Stir Welding/ Processing of Aluminum Alloys: Microstructural Evolution and Mechanical Properties

Z. Y. Ma, A. H. Feng, D. L. Chen & J. Shen

To cite this article: Z. Y. Ma, A. H. Feng, D. L. Chen & J. Shen (2017): Recent Advances in Friction Stir Welding/Processing of Aluminum Alloys: Microstructural Evolution and Mechanical Properties, Critical Reviews in Solid State and Materials Sciences, DOI: 10.1080/10408436.2017.1358145

To link to this article: http://dx.doi.org/10.1080/10408436.2017.1358145

Published online: 18 Sep 2017.

Submit your article to this journal

View related articles

View Crossmark data

Full Terms & Conditions of access and use can be found at
http://www.tandfonline.com/action/journalInformation?journalCode=bsms20

Download by: [University of Connecticut] **Date:** 19 September 2017, At: 03:45

CRITICAL REVIEWS IN SOLID STATE AND MATERIALS SCIENCES
2017, VOL. 0, NO. 0, 1–65
https://doi.org/10.1080/10408436.2017.1358145

Taylor & Francis
Taylor & Francis Group

Check for updates

Recent Advances in Friction Stir Welding/Processing of Aluminum Alloys: Microstructural Evolution and Mechanical Properties

Z. Y. Ma[a], A. H. Feng[b], D. L. Chen[c], and J. Shen[b]

[a]Shenyang National Laboratory for Materials Science, Institute of Metal Research, Chinese Academy of Sciences, Shenyang, China; [b]School of Materials Science and Engineering, Tongji University, Shanghai, China; [c]Department of Mechanical and Industrial Engineering, Ryerson University, Toronto, Ontario, Canada

ABSTRACT
Friction stir welding (FSW), a highly efficient solid-state joining technique, has been termed as “green” technology due to its energy efficiency and environment friendliness. It is an enabling technology for joining metallic materials, in particular lightweight high-strength aluminum and magnesium alloys which were classified as unweldable by traditional fusion welding. It is thus considered to be the most significant development in the area of material joining over the past two decades. Friction stir processing (FSP) was later developed based on the basic principles of FSW. FSP has been proven to be an effective and versatile metal-working technique for modifying and fabricating metallic materials. FSW/FSP of aluminum alloys has prompted considerable scientific and technological interest since it has a potential for revolutionizing the manufacturing process in the aerospace, defense, marine, automotive, and railway industries. To promote widespread applications of FSW/FSP technology and ensure the structural integrity, safety and durability of the FSW/FSP components, it is essential to optimize the process parameters, and to evaluate thoroughly the microstructural changes and mechanical properties of the welded/processed samples. This review article is thus aimed at summarizing recent advances in the microstructural evolution and mechanical properties of FSW/FSP aluminum alloys. Particular attention is paid to recrystallization mechanism, grain boundary characteristics, phase transformation, texture evolution, characteristic microstructures, and the effect of these factors on the hardness, tensile and fatigue properties as well as superplastic behavior of FSW/FSP aluminum alloys.

KEYWORDS
Friction stir welding; friction stir processing; aluminum alloys; microstructure; mechanical property

Table of Contents

1. **Introduction** 2
2. **Process characteristics** 4
   2.1. Severe plastic deformation 4
   2.2. Heat generation and material flow 4
   2.3. Temperature field distribution 7
   2.4. Residual stress 9
   2.5. Multi-pass FSP/FSW 10
   2.6. FSW of dissimilar alloys/metals 11
      2.6.1. Dissimilar welding of different aluminum alloys 11
      2.6.2. Dissimilar welding of aluminum to magnesium 12
      2.6.3. Dissimilar welding of aluminum to copper 13
      2.6.4. Dissimilar welding of aluminum to steel 13
   2.7. Friction stir lap/spot welding 14
3. **Microstructural characteristics** 15
   3.1. Recrystallization mechanism 17
      3.1.1. Continuous dynamic recrystallization 18

CONTACT Z. Y. Ma ✉ zyma@imr.ac.cn; A. H. Feng ✉ aihanfeng@tongji.edu.cn
Color versions of one or more of the figures in the article can be found online at www.tandfonline.com/bsms.
© 2017 Taylor & Francis Group, LLC

3.1.2. Discontinuous dynamic recrystallization 19
3.1.3. Geometric dynamic recrystallization 19
3.1.4. Twinning dynamic recrystallization 19
3.1.5. Particle-stimulated nucleation of recrystallization 20
3.2. Grain structures 20
3.2.1. Grain size 20
3.2.2. Characteristics of grain boundary 21
3.2.3. Abnormal grain growth 21
3.3. Dissolution and re-precipitation 23
3.3.1. 5xxx-series aluminum alloys 25
3.3.2. 2xxx-series aluminum alloys 25
3.3.3. 4xxx-series aluminum alloys 27
3.3.4. 6xxx-series aluminum alloys 27
3.3.5. 7xxx-series aluminum alloys 28
3.4. Characteristic microstructures 28
3.4.1. Onion-ring structure 28
3.4.2. Linear segregation band 31
3.4.3. Zigzag line 32
3.4.4. Kissing bond 33
3.5. Texture 33
4. Mechanical properties 35
4.1. Hardness 35
4.2. Tensile properties 37
4.2.1. Effect of welding parameters and tool geometry 37
4.2.2. Effect of water cooling 39
4.2.3. Effect of characteristic microstructures 40
4.3. Superplasticity 41
4.3.1. High-strain-rate superplasticity 41
4.3.2. Low-temperature superplasticity 41
4.3.3. Enhanced uperplasticity 42
4.4. Fatigue behavior 43
5. Outlooks 45
6. Conclusions 46
Funding 47
References 47

1. Introduction

Friction stir welding (FSW), invented by Thomas and his colleagues at The Welding Institute (TWI, Cambridge, United Kingdom) in 1991,[1] is a rapidly maturing solid-state joining technique, involving frictional and adiabatic heating, plastic deformation (a combination of extrusion, forging, and shearing) and solid-state diffusion. Friction stir processing (FSP) was later developed by Mishra and his co-workers[2] based on the basic principles of FSW. FSP has been proven to be an effective and versatile metal-working technique for generating fine-grained microstructures and surface composites, e.g., for modifying the microstructures of Al-based alloys and Ni-Al bronze.[3] The advances in FSW/FSP area over the past two decades or so have been critically documented in several excellent and classic review articles by Mishra and Ma in 2005,[4] Nandan et al. in 2008,[5] Ma in 2008,[6] Threadgill et al. in 2009,[7] Gan et al. in 2010,[8] Cam in 2011,[9] Simar et al. in 2012,[10] He et al. in 2014,[11] and Mehta and Badheka in 2016.[12]

The basic concept of FSW is remarkably simple. As shown schematically in Figure 1, a specially designed rotating tool (consisting of a shoulder and a pin) is first inserted into the adjoining edges of two sheets to be welded and then moved all along the joint line. During FSW, the material flows in a complex pattern around the tool from the advancing side (AS) to the retreating side (RS),[13] where the AS indicates the side at which the rotational direction and the welding direction are the same, while the RS denotes the side at which the rotational direction is reverse to the welding direction. The heat

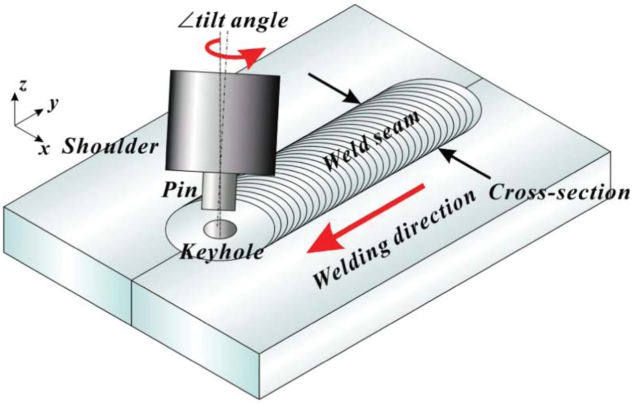

Figure 1. Schematic illustration of FSW.

generated by a rotating tool changes the material in the vicinity of the tool from a hard solid state into a soft "plastic-like" state. The material undergoes extensive plastic deformation following quite complex paths around the tool, depending on the tool geometry, process parameters, and material to be welded. The maximum temperature could approach ~0.8 T_m,[14] or even 0.95 T_m[15] in aluminum alloys (where T_m is the melting temperature in Kelvin), depending on the material, tool design, and operating conditions.[13] The material experiences severe plastic deformation (SPD) and thermal exposure, which normally leads to the formation of a fine recrystallized grain structure with more or less preferred orientation (or texture) in the nugget zone (NZ).[16]

The scientific and technical activities in the field of FSW/FSP have reached a critical juncture in terms of the number of researchers and the number of publications,[17][*] In 2008, a Viewpoint Set no. 43 "Friction stir processing" organized by Mishra in *Scripta Materialia*,[17] gives a timely overview of FSW/FSP process. A total of 11 papers have been included in the Viewpoint Set written by some of the leading researchers in this area, for example, "the nature of fully coupled thermomechanical process during FSP" by Colligan and Mishra[18]; "thermal modeling" by Schmidt and Hattel,[19] Reynolds,[20] and Arbegast;[21] "microstructual evolution ahead of the tool" by Fonda et al.;[22] "recrystallization mechanisms" by McNelley et al.,[13] and Masaki et al.;[23] "microstructural refinement and property enhancement of cast light alloys" by Ma et al.;[24] "abnormal grain growth (AGG)" by Charit and Mishra;[25] "the strength of friction stir welded and friction stir processed aluminum alloys" by Starink et al.;[26] and "corrosion of aluminum alloy friction stir welds" by Paglia and Buchheit.[27]

FSW is a promising solid-state joining technique initially developed for aluminum alloys, as it offers many advantages over the conventional fusion welding, in particular the elimination of solidification and liquation cracking, and shrinkage porosity. Recently, FSW/FSP has attracted a special attention of the aerospace and automotive industries, due to the potential weight reduction and cost saving, along with the favorable retention of properties. This technique can be used to produce a variety of forms of welds, including butt, lap, corner, T, spot, fillet, and hem joints as well as to weld hollow objects, such as tanks and tubes/pipes. Recently, near-net shape manufacturing of large titanium parts has been accomplished by combining FSW with superplastic forming (SPF).[28–30] This innovative and enabling joining technique has thus been proven to be a good alternative especially for the aerospace materials, i.e., 2xxx-, 4xxx-, 5xxx-, 6xxx-, and 7xxx-series aluminum alloys, where the welds also involve different series or dissimilar materials. The weldable materials via FSW include:

(1) aluminum and its alloys;[16,31–59]
(2) copper and its alloys;[60–71]
(3) magnesium and its alloys;[3,72–103]
(4) titanium and its alloys;[104–119]
(5) iron and steels;[120–133]
(6) nickel and its alloys;[134–140]
(7) metal matrix composites (MMCs);[141–159]
(8) dissimilar metals and alloys; and[12,160–171]
(9) dissimilar bulk metallic glasses (BMG) and metals.[172,173]

This article will be limited to the FSW/FSP of aluminum and its alloys with main focus on the microstructural evolution and mechanical properties. From 1991 until May 2017, over 4,352 papers on the FSW/FSP of aluminum alloys have been published, as shown in Figure 2. In particular, over the past 10 years or so there is a linear increase in the number of publications per year in this area. FSW has already been used in routine as well as critical applications for the joining of structural components made of aluminum and its alloys. It shows a great potential in manufacturing sectors, particularly in the aerospace, defense, marine, aircraft, automotive and railway industries. FSW has been applied for welding the fuselage, structural parts, and cryogenic tanks in the aerospace industry.[174] Joining of panels and large extruded profiles is also an interesting application for FSW, and it is now used in ship, bridge, and wagon building and in offshore industry.[174]

FSW of aluminum alloys has prompted considerable scientific and technological interest because of the difficulties and challenges of ensuring the reliability and structural integrity of joints of such lightweight alloys using traditional fusion welding processes. Extensive research in

---

[*] A search from a few authoritative databases using a key word of "friction stir" on May 7, 2017 showed: 6,113 publications from the Web of Science; 7,699 publications from the Engineering Village (Compendex only); 22,124 publications from ScienceDirect of Elsevier; or about 49,500 publications from Google Scholar so far.

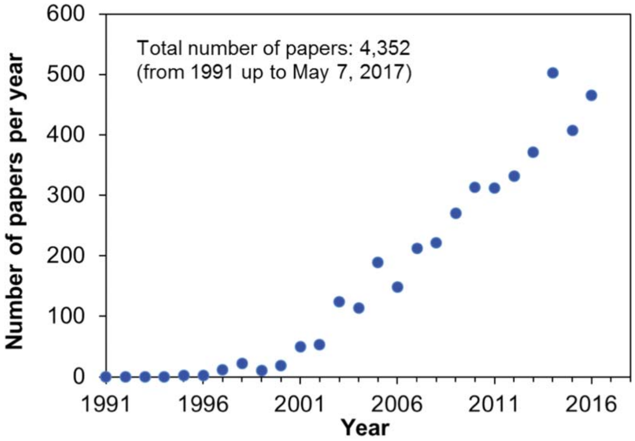

Figure 2. Number of publications per year on FSW/FSP of aluminum alloys since 1991 up to May 7, 2017, searched from the Compendex-Engineering Village database.

the FSW of aluminum alloys has been undertaken involving welding parameter optimization,[50,55,175,176] tool design,[177–182] material flow pattern,[20,21,183–189] temperature field distribution,[137,186,190–195] microstructural characterization,[31,35,38,42,54,196–199] texture,[16,39,49,200,201] residual stress,[45,202–206] mechanical response,[43,51,53,57,207–213] and thermomechanical quantities.[10,186] An integrated modeling framework devoted to the FSW of 6xxx-series aluminum alloys has been established and well documented in Simar et al.[10] in order to present routes for the optimization of the FSW process using both experiments and models. The suite of models involves an in-process temperature evolution model, a microstructure evolution model with an extension to heterogeneous precipitation, a microstructure based strength and strain hardening model, and a micro-mechanics based damage model.[10,214]

To advance FSW/FSP from the research stage into the direct applications, performance and property data are needed, which are often the bottleneck of limiting the widespread applications of FSW/FSP. Despite the potential benefits, a vast amount of research and development activities are still needed to better understand the microstructure associated with FSW/FSP. This article is therefore aimed at briefly outlining the recent research and development in the field of FSW/FSP so as to provide up-to-date information with the intention that further light-weight and cost-effective use of FSW/FSP will be facilitated.

2. Process characteristics

2.1. Severe plastic deformation

SPD is a generic term describing any metalworking techniques imparting a complex stress state, high strain typically with true strains ≥ 10,[215] and/or high shear, results in a very high dislocation density and exceptional grain refinement, producing equiaxed ultrafine grain (UFG) size (<1 μm) or even nanocrystalline structure (<100 nm).[216,217] A number of SPD processing routes have been developed to produce a bulk UFG materials, including equal channel angular pressing (ECAP),[218,219] high-pressure torsion,[220] multi-directional forging,[221] cyclic-extrusion-compression,[222] and accumulative roll-bonding.[223,224]

Because FSW/FSP generates heavy deformation at high temperatures,[225] it is now well recognized that FSW/FSP can be regarded as a type of high-temperature SPD, involving transients and steep gradients in strain, strain rate and temperature.[13,16,225] Different from conventional SPD techniques that result in the formation of highly deformed microstructures, FSW/FSP is able to create fine and equiaxed fully recrystallized grains ranging from nano-scale to micro-scale.

2.2. Heat generation and material flow

The mechanisms of FSW are highly coupled physical phenomena, i.e., the heat generation is related to material flow and frictional/contact conditions and vice versa.[11,19] Heat generation has two components: friction generated heat and bulk plasticity generated heat.[10,124,186] The heat transfer has itself two contributions: diffusion and convection via material flow.[10]

The material flow during FSW is quite complex depending on the tool geometry, process parameters, and material to be welded.[4] The flow of material around the welding tool during FSW is closely linked to many key issues related to the process.[20,226] Understanding of the flow is critical to determination of accurate thermomechanical processing conditions during FSW.[20]

Recent experimental and computational works have provided significant insight about several interesting features of materials flow in FSW and the joining process.[5] A number of approaches, such as tracer technique by markers,[185,227–230] welding of dissimilar alloys/metals,[231] and numerical simulations,[11,186] have been used to visualize material flow pattern in FSW.[4] Huang et al.[232] reported that material flow behavior during FSW of 6082Al-T6 alloy was visualized by marker insert technique, e.g., Cu foil fragments. Murr and co-workers[231] investigated the solid-state flow visualization in FSW of 2024Al to 6061Al alloys. Schmidt et al.[183] reported the material flow by traditional metallography as well as X-ray and computer tomography (CT). The 2D and 3D CT images were used in parallel with micrographs for visualization of the flow field.[183] Nandan et al.[124] calculated the non-Newtonian viscosity for the metal flow considering temperature and strain rate-dependent flow stress. Morisada et al.[233] investigated the material flow during the FSP by means of the dispersion of the

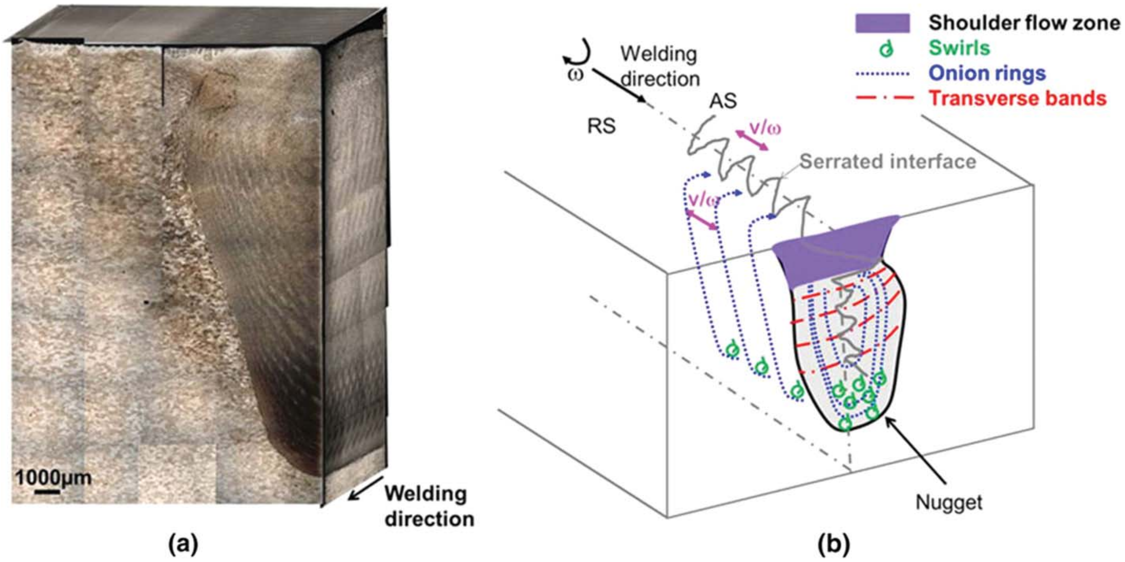

Figure 3. 3D view of the weld's AS (light microscopy) (a) and 3D representation of the global weld (b).[188] (© Springer. Reprinted with permission from Fenoel et al.[188] Permission to reuse has been obtained from the rightsholder.)

fullerence. Morisada et al.[229] reported that the material flow could be 3D visualized by X-ray radiography using a tiny spherical tungsten tracer. Figure 3 proposed a 3D representation of the material flow pattern.[188]

Apart from experimental approaches, a number of studies have been carried out to model the material flow during FSW/FSP.[11,202,234] A 3D finite element method (FEM) model has been used to show the distribution of the most important field variables, namely temperature, strain and strain rate.[184] These attempts were aimed at understanding the basic physics of the material flow occurring during FSW/FSP.

Strain, strain rate, temperature, and their distribution during FSW/FSP are the primary factors determining how microstructures evolve. These microstructural evolutions inherently affect the mechanical properties and hence the performances of the final product.[10] It would be of interest and challenging to study the relationships among the microstructural evolution and strain, strain rate, as well as temperature. Unfortunately, it is very difficult to measure quantitatively the strain, strain rate and temperature undergone by the material during FSW/FSP due to the complicated dynamic changes.

If the flow field represented by Figure 4a and 4b is substantially correct, then under conditions wherein material passes around the tool only once, the approximate strain experienced by material along a streamline which intersects the tool pin can be expressed as Eq. (1):[20]

$$\varepsilon = \ln\left(\frac{l}{APR}\right) + \left|\ln\left(\frac{APR}{l}\right)\right|, \tag{1}$$

where APR is the tool advance per revolution and l can be expressed as:[20]

$$l = 2r\cos^{-1}\left(\frac{r-x}{r}\right). \tag{2}$$

In Eq. (2), r is the pin diameter and x is the distance, perpendicular to the welding direction, from the retreating side of the tool to the streamline in question.[20]

Based on Eqs. (1) and (2), the strain as a function of position along the pin is plotted in Figure 4c for an advance per revolution of 0.5 mm and a pin diameter of 10 mm.[20]

Direct measurements of the strain in the NZ are difficult due to the movement of material around the tool during FSW. Equivalent strains in FSW were computed by Buffa et al.[235] based on thermo-mechanically coupled rigid-viscoplastic 3D FEM, and by Schimdt and Hattel[236] using solid mechanics. The maximum values of equivalent strains varied from 6[235] to 133.[236] Arora et al.[237] reported that the computed strains were in the ranges −10 to 5 during FSW of 2524Al alloy from a 3D coupled viscoplastic flow and heat transfer model.[238]

Similarly, the strain rate could not be directly estimated because it is difficult to observe the material movement during FSW.[23] Conventional hot working processes, such as rolling, extrusion and forging, generally involve strain rates in the range 10^0–10^2 s^{-1} at temperatures above 0.5 T_m, but in the absence of the transients and gradients in strain, strain rate, and temperature that characterize FSW/FSP.[13] A simulation investigation of nugget grain structures in 7010Al alloy

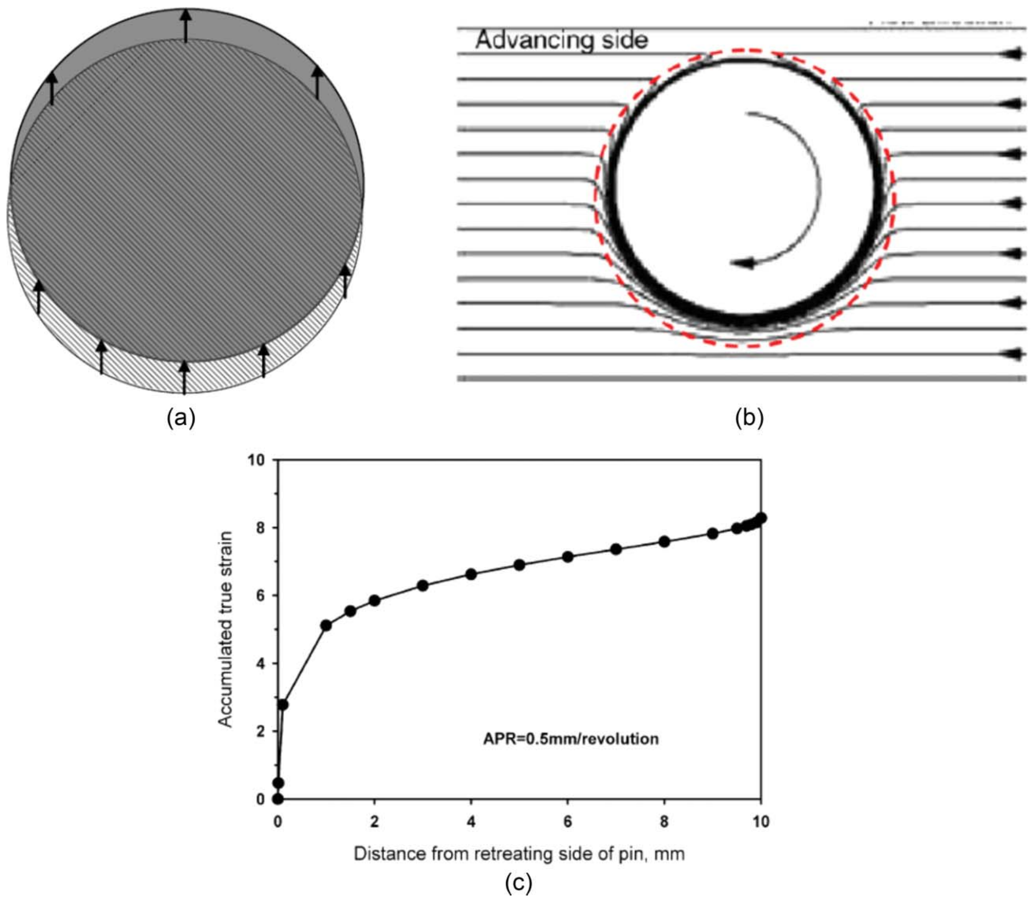

Figure 4. (a) schematic illustration of required material transfer per tool revolution, (b) streamlines from simulated pin-rounding flow field and and approximate limits of shear zone, (c) distribution of strain within the probe diameter based on Eqs. (1) and (2), an APR = 0.5 and 10 mm diameter probe. (© Elsevier. Reprinted with permission from Reynolds.[20] Permission to reuse has been obtained from the rightsholder.)

was performed by Hassan et al.[239] using high-strain torsion testing. Although they deformed the samples to very large strains (~20) at a strain rate of 0.005 s^{-1}, it is still very difficult to simulate the process of FSW/FSP. During FSW/FSP, the material that flows around the tool undergoes extreme levels of plastic deformation, reaching effective strains in excess of 40 at very high strain rates (~10 s^{-1}), as well as a complex stress-strain state.[240]

Some researchers have attempted to estimate the strain rate during FSW/FSP.[240,241] Jata and Semiatin[35] suggested that the strain rate was in the order of 10 s^{-1} during FSW of Al-Li-Cu alloy using the shear strain extrapolated from that measured in the thermomechanically affected zone (TMAZ) and the deformation time in the NZ. Additionally, in the majority of cases, grain growth in the cooling stage of FSW was not taken into consideration.[35,242] Frigaard et al.[37] estimated the strain rate during FSW of 6082Al alloy and 7108Al alloy to be between 1.6 and 17.3 s^{-1}. The effective strain rate during FSW of 1050Al alloy was estimated experimentally to be about 2–3 s^{-1} by simulating the recrystallized grains of the NZ through a combination of the plane-strain compression at various strain rates and subsequent cooling tracing the cooling cycle of FSW by Masaki et al.[23]

Reliable strain rate values can be estimated using the Zener-Hollomon relation provided that the peak temperature and average grain size in a specific location can be accurately determined.[191,192] The results indicated that the grain size of the pure aluminum in the NZ estimated by the Z parameter using the obtained strain rate shows good agreement with that observed by electron backscatter diffraction (EBSD) mapping.[243]

Morisada et al.[243] reported that the strain rate in FSW could be determined by 3D visualization of material flow using X-ray radiography. Figure 5 shows the 3D image of the material flow and calculation method for strain and strain rate.[243] The velocity of the tungsten tracer (V) can be directly calculated by the change in the coordinate for 0.002 s on the welding direction- (WD) transverse direction (TD)

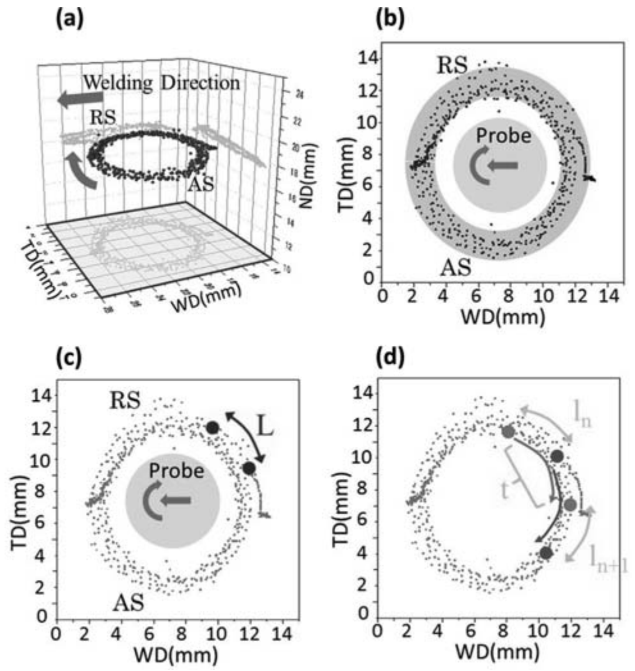

Figure 5. Locus of the tracer observed by the X-ray transmission real-time imaging systems: (a) 3D image, (b) 2D image on TD-WD plane, (c) schematic drawing of calculation method for strain, and (d) schematic drawing of calculation method for strain rate. (© Elsevier. Reprinted with permission from Morisada et al.[243] Permission to reuse must be obtained from the rightsholder.)

plane, as shown in Figure 5c using Eq. (3):[243]

$$V = L/T, \tag{3}$$

where L is the distance between the 2 plots and T is the transit time from one plot to the other plot.[243]

The strain rate can be easily calculated if the direction of the material flow is only tangential to the rotating tool, as shown in Figure 5d using Eq. (4):[243]

$$\dot{\varepsilon} = \frac{l_{n+1} - l_n}{l_n} / t, \tag{4}$$

where l_n is the distance between the 2 plots and m is the velocity of the tracer between the 2 plots and t is the deformation time. l_n can be calculated using Eq. (5):[243]

$$l_n = \frac{v_{m+1} - v_m}{\Delta t} \tag{5}$$

2.3. Temperature field distribution

In recent years, significant progresses have been made in the understanding of physical processes that take place during FSW of aluminum alloys.[37] The hardness distribution of the FSW heat-treatable aluminum alloys is mainly governed by the distribution of precipitates, which is strongly influenced by the thermal hysteresis.[34] The heat input plays a key role in determining the microstructural evolution and their mechanical properties, and is very sensitive to the welding parameters during FSW.[244]

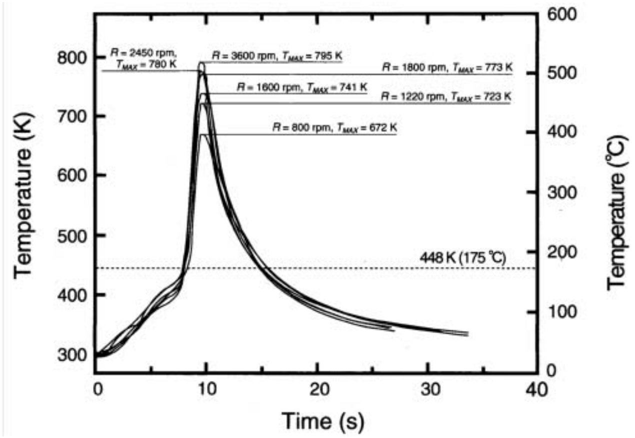

Figure 6. Thermal histories during FSW at several rotational speeds of 6063Al alloy. (© Springer. Reprinted with permission from Sato et al.[15] Permission to reuse must be obtained from the rightsholder.)

The thermal cycles in FSW could be estimated from the microstructures or measured using thermocouples,[5,245–248] and in situ neutron-diffraction where the measured lattice-distortion is related to the change in temperature.[193]

Thermal hysteresis curves during FSW at several rotational rates are shown in Figure 6.[15] Thermal cycle were measured in the NZ using an alumel-chromel thermocouple having a diameter of about 1 mm.[15] Although it is hard to accurately measure the peak temperatures in FSW, it has been reported that the maximum temperatures could reach 0.8 T_m,[14] or even 0.95 T_m[15] in the FSW of aluminum alloys. The peak temperature increases with increasing rotational rate. As with most welding processes, there is a steep thermal gradient from the weld centerline to the surrounding base metal (BM).[14] As a result, the microstructure (including grain sizes, vacancies, solutes, and precipitates) across the various regions of a FSW joint varied as a function of the local peak temperature and the duration above a given critical temperature.[14]

Frigaard et al.[37] reported that in the heat-affected zone (HAZ), the dissolution of the primary strengthening phase (i.e., β'' or η' in 6082Al and 7108Al alloy, respectively) contributed to the development of a permanent soft zone, while the growth of the nonhardening phase (β' or η) occurred during the cooling process of the thermal cycle (Figure 7).[37] Liu and Ma[175] indicated that in the FSW of 6061Al-T651 alloy, the thermal cycles experienced by the HAZ had approximately the same

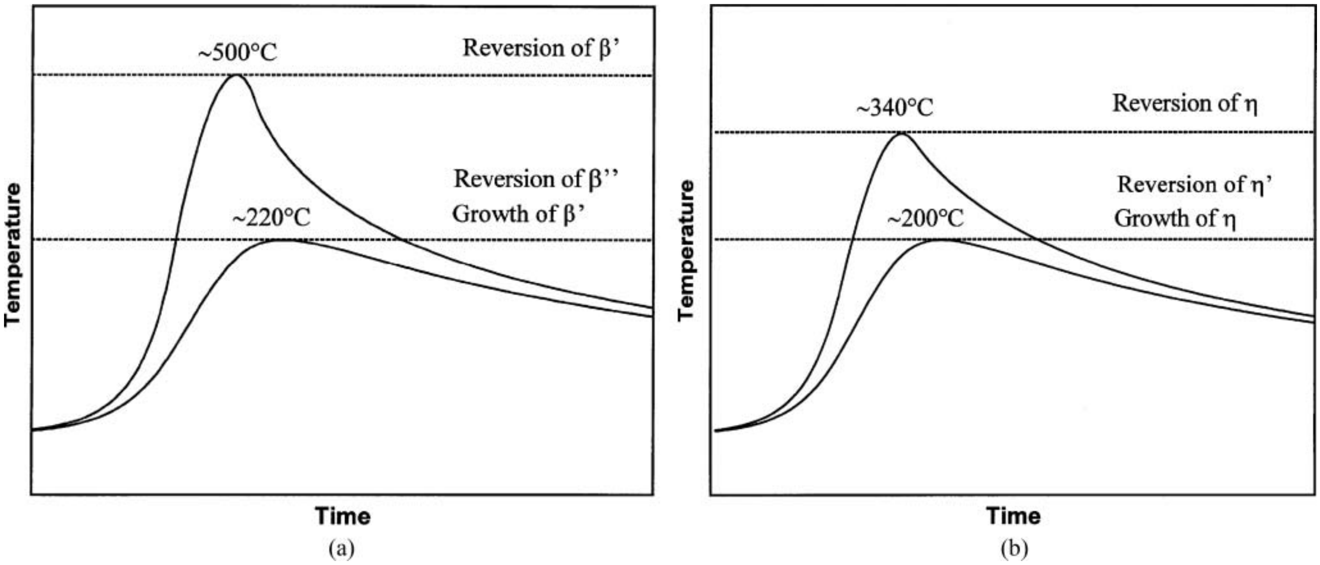

Figure 7. Schemactic diagrams showing details of microstructure evolution of age hardened aluminum alloys in HAZ during FSW: (a) 6082Al-T6 alloy and (b) 7108Al-T6 alloy. (© Springer. Reprinted with permission from Frigaard et al.[37] Permission to reuse must be obtained from the rightsholder.)

peak temperature of 360–370°C with varied durations that were governed by the welding speed. Kang et al.[249] measured the peak temperature of different positions in an FSW joint of 2219Al-T8 alloy, as shown in Figure 8. The results indicated that temperature was not a symmetric distribution to the center position of the NZ, and it was about 5–10°C lower on the RS than that on the AS.[249]

In view of the difficulty in experimentally measuring temperature history in the FSW, several models were developed to predict the temperature distribution and history during FSW.[37,124,175,190,202,247,250,251] These models can be categorized into two basic types: the models of the first type assume that all the heat generation is caused by the friction work,[37,190] while the models of the second type assume that the heat generation is caused by both the friction work and the plastic energy dissipation.[124,202]

For both types of models, the accuracy of the predicted temperature is mainly determined by the heat generation for the friction work. In the early stage of FSW investigation, the heat generation model for the friction work is simply based on the Coulomb friction law and using a constant friction coefficient.[37,252] Such a simplified model will lead to an unreasonable high temperature. To get rid of the unreasonable high temperature, a maximum temperature that is artificially defined must be set in the model.[37] Then in this model the maximum temperature is independent of the applied experimental conditions.[37] Later, the heat generation model for the friction work that takes into account both the sliding and sticking friction conditions was developed.[124,190] As shown in Figure 9, the predicted temperature profiles agree well with the experimentally determined weld shapes.[238,253] However, for this type of model, it is difficult to evaluate the relative speed between the tool and the work-piece for estimating the fractions of sliding friction and sticking friction. Up until now, an empirical equation that was obtained from the rolling tests was applied to estimate the relative speed between the tool and the work-piece.[124]

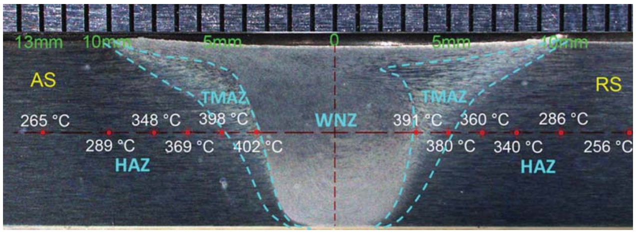

Figure 8. Peak temperature of different positions of an 2219Al-T8 alloy FSW joint. Each division in the scale represents 1 mm. (© Springer. Reprinted with permission from Kang et al.[249] Permission to reuse must be obtained from the rightsholder.)

In recent years, the inverse solution framework is increasingly used to estimate the heat generation during FSW. Zhang et al.[250,251] proposed an equivalent friction coefficient-based heat generation model for FSW thermal modeling and simulation. The equivalent friction coefficient depends on temperature and is determined via an inverse solution framework. Since the equivalent friction coefficient is a function of temperature, the total heat generation is not an explicit input parameter as in most of other thermal models, but is implicitly determined during the thermal modeling process. Using this model, one does not have to manually specify a maximum

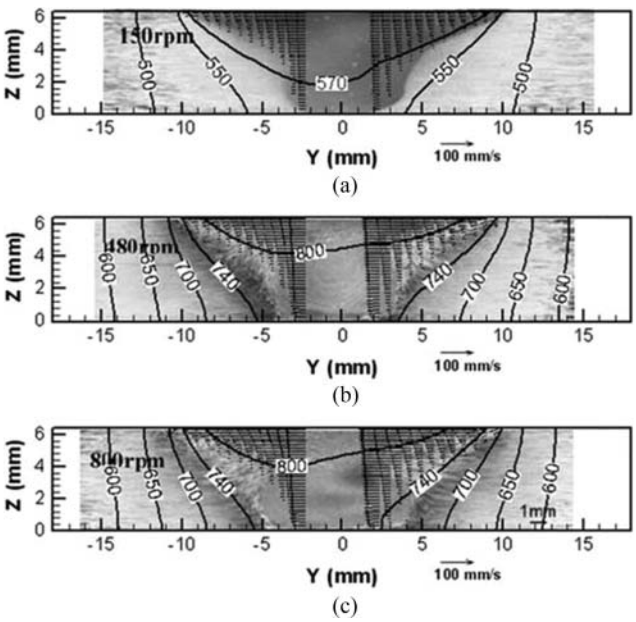

Figure 9. Comparison of predicted temperature (K) and velocity profiles with experimental weld shapes at a welding speed of 127 mm/min with varied rotational rate: (a) 150 rpm, (b) 480 rpm, and (c) 800 rpm. (© Elsevier. Reprinted with permission from Arora et al.[238] Permission to reuse must be obtained from the rightsholder.)

temperature, which is actually determined automatically from the model due to a self-consistency mechanism. Zhang et al.[250,251] showed that this model was robust and the predicted maximum temperature agreed very well with the reported experimental data[15] and the empirical Arbegast-Hartley model,[254] as shown in Figure 10.[15,175,250,251,254] Meanwhile, the predicted temperature histories agreed very well with the measured data in various welding conditions.[175,251] It is also shown that the temperature contour moves away from the butting surface with increasing rotational rate and shoulder diameter, and decreasing welding speed.[250,251] Besides, this thermal model can also been used for predicting the fracture locations of FSW 6061Al-T651 joints, as shown in Figure 11.[175,251]

2.4. Residual stress

Residual stresses were inherently introduced into materials through thermal or severe thermomechanical deformation, such as welding, forming, coating, and heat treatments.[255] Excessive tensile residual stresses are known to be detrimental to the integrity and performance of components. Although FSW offers various advantages for joining lightweight metals, significant residual stresses are inevitable.[120,159,256] The residual stress of the weld negatively affects its fatigue properties[45,202,203] and fracture toughness.

The residual stresses across the FSW joints have been studied by the hole-drilling-method,[206,257,258] X-ray diffraction (i.e., $\sin^2\psi$ method),[202,259] neutron diffraction,[163,204,205,255,256,260,261] high-energy synchrotron

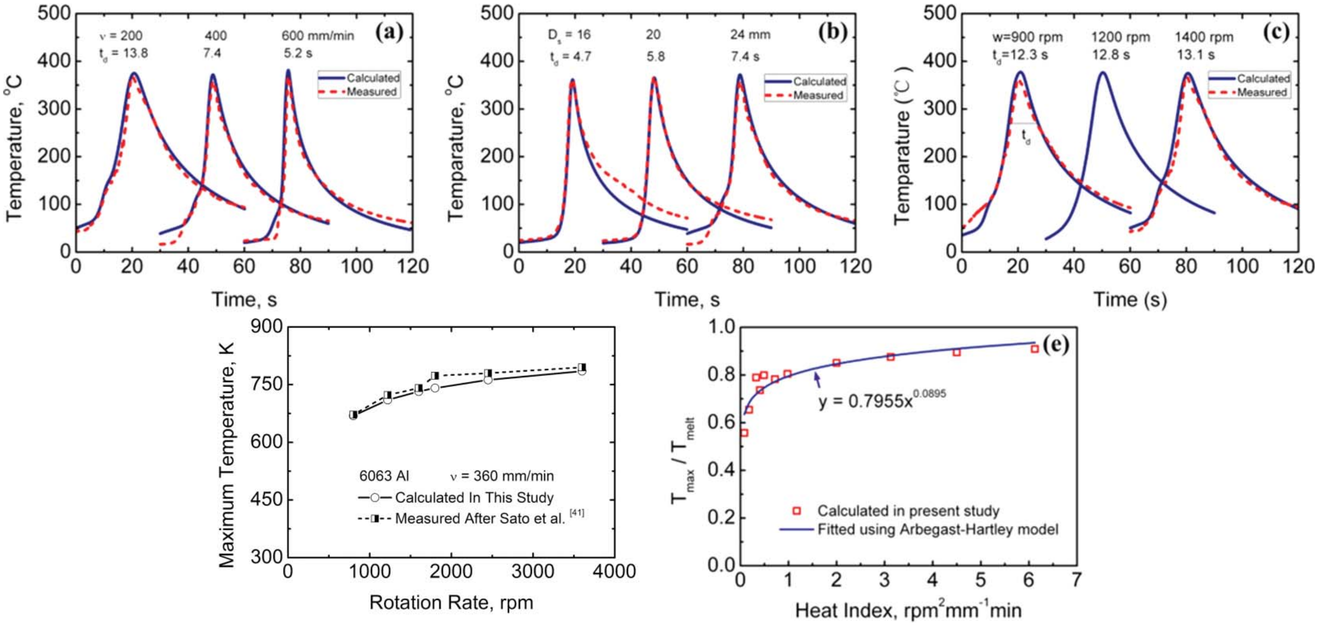

Figure 10. Comparison between (a)–(c) the predicted and measured thermal histories,[251] (d) the predicted maximum temperature near the bottom of the welding butt face and the reported experimental results,[250] and (e) the predicted maximum temperature and the empirical Arbegast-Hartley model.[254] (© Springer. Reprinted with permission from Zhang et al.[251] Permission to reuse has been obtained from the rightsholder.) (© Springer. Reprinted with permission from Zhang et al.[250] Permission to reuse has been obtained from the rightsholder.) (© ASM International. Reprinted with permission from Arbegast & Hartley.[254] Permission to reuse has been obtained from the rightsholder.)

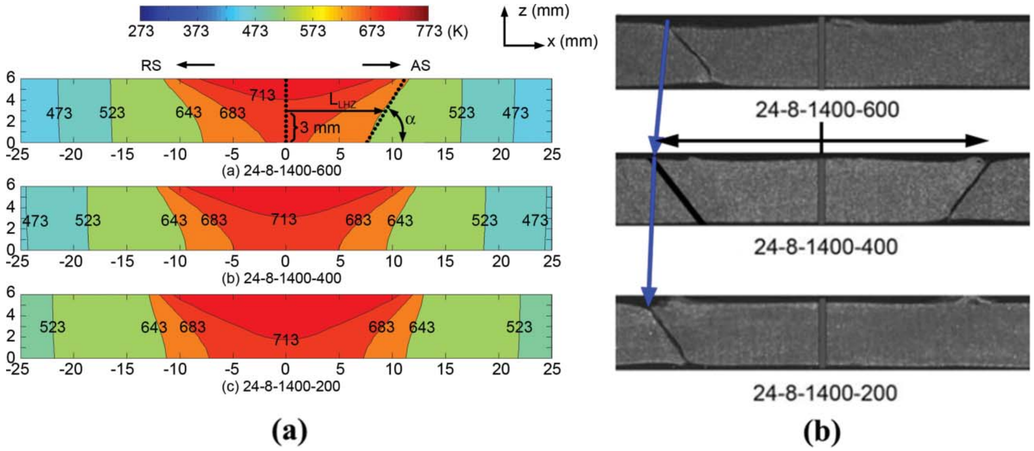

Figure 11. Comparison between (a) predicted locations of low hardness zone with peak temperature of about 370°C and (b) experimental location of fractures. Note that in "24-8-1400-400" of (b), fracture on RS is artificially created by mirror imaging of real fracture on AS. (© Springer. Reprinted with permission from Zhang et al.[251] Permission to reuse has been obtained from the rightsholder.) (© Springer. Reprinted with permission from Liu & Ma.[175] Permission to reuse has been obtained from the rightsholder.)

radiation,[262,263] and the cut compliance technique.[264] These investigations revealed the following findings.[4] First, the residual stresses in all the FSW joints were quite low compared with those in fusion welded joints, due to the relatively lower peak temperatures which do not reach or exceed the melting point of materials that is required in the fusion welding. Woo et al.[261] indicated that the predominant source of the residual stress is frictional heating from the tool shoulder. Second, longitudinal (parallel to welding direction) residual stresses were generally tensile and transverse (normal to welding direction) residual stresses were compressive. The low residual stress in the NZ was attributed to the lower heat input during FSW and recrystallization accommodation of stresses. Third, both longitudinal and transverse residual stresses exhibited an "M"-like distribution across the weld, as shown in Figure 12.[265]

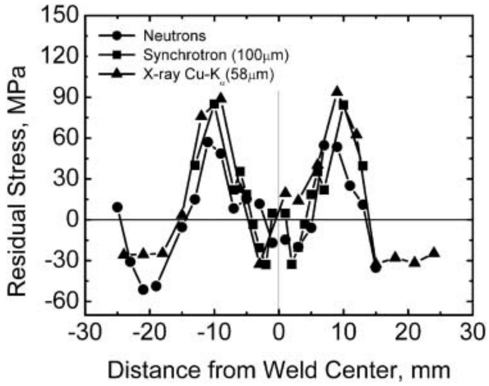

Figure 12. Longitudinal residual stress distribution in FSW 6013Al-T4 alloy joints determined by different measurement methods (tool rotational rate: 2500 rpm, traverse speed: 1,000 mm/min, tool shoulder diameter: 15 mm).[265]

2.5. Multi-pass FSP/FSW

Single-pass FSP resulted in a narrow-processed zone, which might not be suitable for practical engineering applications. In this case, multi-pass FSP with a certain level of overlap between the successive passes is a desirable consideration for microstructure modification and mechanical property improvement.[266,267] Ma et al.[266] studied five-pass FSP, with 50% overlap, in FSP cast A356, as shown in Figure 13. It was indicated that overlapping FSP did not exert a significant effect on the size and distribution of the Si particles.[266] Meenia et al.[267] reported that multi-pass FSP of Al-Si alloy resulted in particle and grain refinement.

In some situations, such as repair or crossing weld beads, it may be necessary to perform in-situ multi-pass FSW.[264] Brown et al.[264] conducted in situ five-pass FSW on 7050Al-T7451 alloys. It was indicated that the overall reduction in the transverse tensile strength from pass one to pass five was 7%.[264] The strain map and fracture path for FSW 7050Al-T7451 alloy joints with different passes are shown in Figure 14.[264] It was noted that with increasing the FSW passes, the fracture locations moved from the HAZ to the NZ.

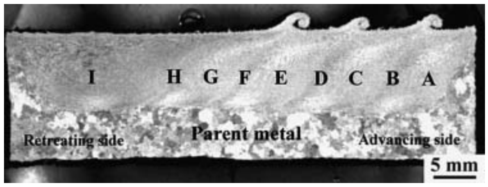

Figure 13. Macrographs showing nugget and transitional zones of five-pass FSP A356 alloy. (© Elsevier. Reprinted with permission from Ma et al.[266] Permission to reuse has been obtained from the rightsholder.)

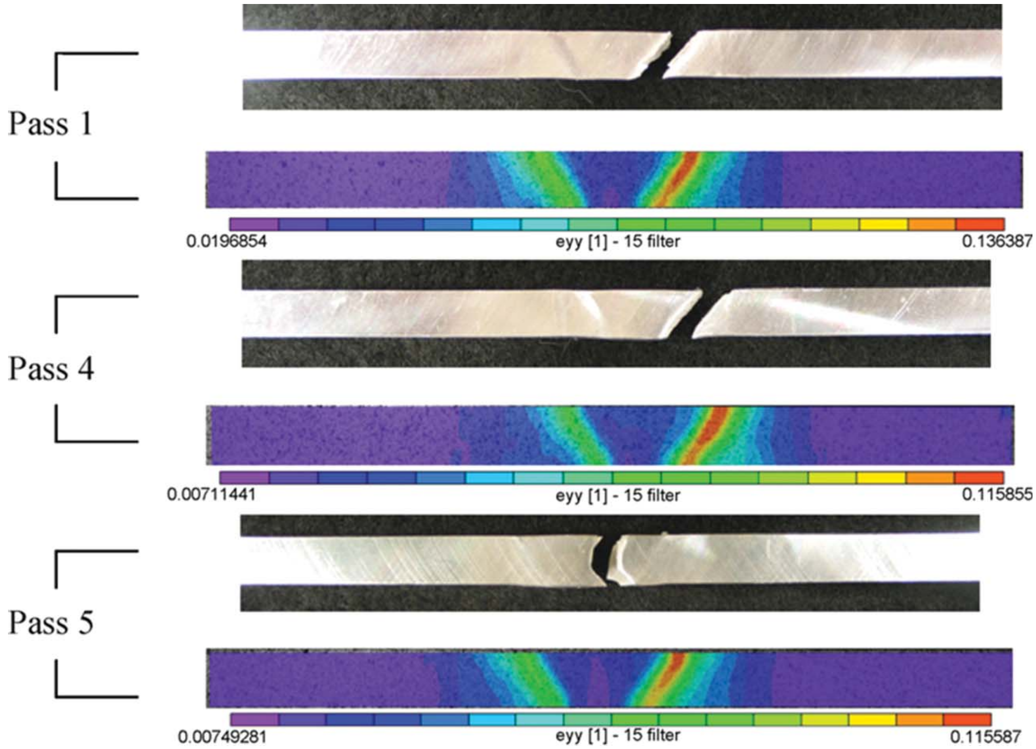

Figure 14. Image correlation strain maps near fracture load and corresponding, fractured tensile specimens. (© Elsevier. Reprinted with permission from Brown et al.[264] Permission to reuse must be obtained from the rightsholder.)

2.6. FSW of dissimilar alloys/metals

Conventional structural components are normally built up using discrete components of various metals/alloys.[163] The welding of dissimilar metals are necessary in applications that require different material properties within the same component, e.g., dissimilar aluminum alloys, and aluminum to other metals for weight reduction, electric connections, etc.[268] However, FSW of dissimilar metals is very difficult due to the enormous differences in mechanical and metallurgical properties.[12,269] In the earlier studies, FSW of dissimilar metals/alloys was used to visualize solid-state material flow pattern.[4,231]

Recently, FSW has been successfully and increasingly employed to join dissimilar alloys due to its technical and economic advantages, such as aluminum to other aluminum alloys,[270–277] to magnesium,[161,278–280] to copper,[12,281] to steel,[162,169,170,282–292] to BMG,[172] to titanium,[293] or to silver.[164] Detailed studies on the material flow, interface configurations,[294] parameters, and mechanical properties characteristics of dissimilar FSW joints are required before implementation in structural applications.[272,295]

2.6.1. Dissimilar welding of different aluminum alloys

FSW offers a sufficiently feasible solutions in dissimilar combinations among high strength, good formability, and weldability, such as 2xxx to 5xxx-series aluminum alloys,[276] 2xxx to 6xxx-series aluminum alloys,[231,272,296] 2xxx to 7xxx-series aluminum alloys,[163,270,274,297,298] 1xxx to 6xxx-series aluminum alloys[299] 4xxx to 6xxx-series aluminum alloys,[271,300] 5xxx to 6xxx-series aluminum alloys,[263,269,301–306] 5xxx to 7xxx-series aluminum alloys,[307–309] 6xxx to 7xxx-series aluminum alloys.[273,275,295,310–313]

Peel et al.[263,302] reported the so-called processing window and residual stress of the dissimilar FSW 5083Al-6082Al alloys. Giraud et al.[312] reported that the dissimilar FSW of 7020Al-T651 to 6060Al-T6 alloys as shown in Figure 15. Severely deformed grains were observed in the TMAZ-HAZ in the AS.[312] Li et al.[231,296] provided vivid images illustrating flow visualization and complex flow patterns in dissimilar FSW of 2024Al to 6061Al alloys. Post-weld heat treatment (PWHT) was used to restore the mechanical properties of dissimilar FSW of 7075Al-O to 6061Al-O alloys.[295]

It should be emphasized that prediction of the amount of heat generation, material flow, and mechanical properties of the dissimilar FSW joints by means of theoretical analysis is difficult.[304] Zhang et al.[314–316] developed valuable models for predicting heat generation, grain growth during FSW of 6xxx to 2xxx-series aluminum alloys.

Zhong et al.[317] reported that ultrasonic vibration could improve material flow in dissimilar FSW of

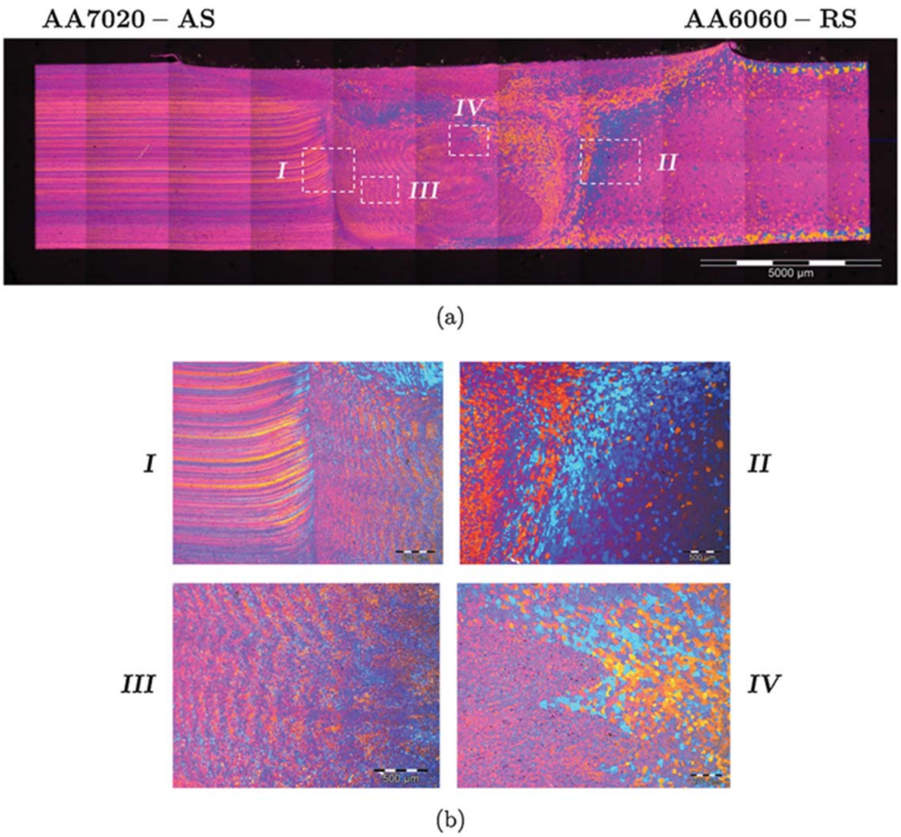

Figure 15. (a) Optical micrograph (OM) of cross-section of BW7 (R ratio is 0.15 mm/rev); (b) details of cross-weld: I–transition between TMAZ nugget on 7020Al alloy side, II–transition between TMAZ and nugget on 6060Al side, III–banded structure in the nugget on 7020Al alloy side, IV–both side of dissimilar nugget. (© Elsevier. Reprinted with permission from Giraud et al.[312] Permission to reuse must be obtained from the rightsholder.)

6061Al-T6 to 2024Al-T3 alloys. Miles et al.[269] focused on the formability of FSW joint of dissimilar 5xxx to 6xxx-series aluminum alloys, which might be used in "tailored blanks" considering the engineering requirements. So far, FSW of dissimilar aluminum castings to wrought plates has found increasingly applications in fabricating airframe and missile components due to high design efficiency and low processing cost.[160,294,300]

2.6.2. Dissimilar welding of aluminum to magnesium

Magnesium is the lightest structural metals with a density two-thirds that of aluminum and one-quarter that of steel.[318] Dissimilar welding of aluminum and magnesium alloys would achieve weight reduction by a substitution of magnesium alloys for aluminum alloys.[161] However, it is known that a variety of attempts to weld aluminum/magnesium alloys failed by using arc welding, electron beams and laser beams, due to the formation of coarse grains and large numbers of brittle intermetallic compounds in the weld during welding.[161,279]

FSW has a high possibility of making high-quality dissimilar welds of aluminum and magnesium alloys.[161] It was shown previously[278,280] that dissimilar FSW of aluminum to magnesium led to dynamic recrystallization (DRX) in the NZ with an intercalated, chaotic microstructure. Firouzdor et al.[268] studied the effect of material position, travel speed, and rotational rate on dissimilar FSW of 6061Al alloy to AZ31 magnesium alloy. The results indicated that the optimum FSW window was significantly larger with magnesium on the AS and tool offset toward to the magnesium side.[268] The heat input was a key variable governing the effect of welding condition on the joint strength.[268]

Dissimilar FSW of aluminum to magnesium resulted in the formation of brittle intermetallic compounds, leading to poor mechanical properties, especially the fracture toughness.[319,320] A large volume of intermetallic compounds were identified as $Al_{12}Mg_{17}$ in a dissimilar FSW of 1050Al alloy to AZ31 magnesium alloy,[161] Al_3Mg_2 and $Al_{12}Mg_{17}$ in the dissimilar welding of 6061Al alloy to AZ31B magnesium alloy,[320] and AZ31 magnesium alloy to 1060Al alloy[279] Although FSW is considered as a solid-state welding process, liquid formation is likely to occur in FSW of aluminum to magnesium in view of rather low eutectic temperatures of

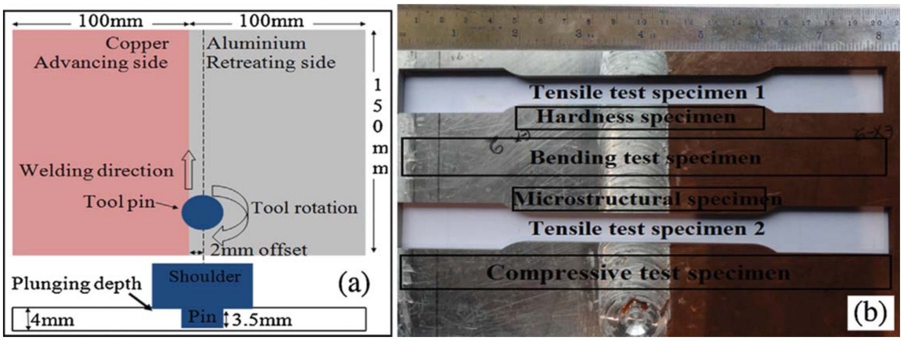

Figure 16. Dissimilar FSW of copper and aluminum alloys: (a) Tool offset and plunging depth scheme, (b) scheme of extraction of specimen from FSWed plate. (© Elsevier. Reprinted with permission from Sahu et al.[322] Permission to reuse has been obtained from the rightsholder.)

437°C and 450°C in the binary Al-Mg phase diagram,[320] resulting in easy formation of intermetallic compounds.

2.6.3. Dissimilar welding of aluminum to copper

Joints of dissimlar aluminum to copper, are extensively used in various industries, such as electricity supply systems and heat exchangers.[12,294,321] However, it is quite difficult to achieve defect-free FSW for a dissimilar aluminum to copper system, due to different chemical and physical characteristics. In addition to conventional FSW parameters such as rotational rate, welding speed, and plunge depth,[322] tool offset parameter is the main factor for determing the welding quality in a dissimilar weld.[281] Sound defect-free dissimilar FSW joints of aluminum and copper could be obtained under specific critical offset toward the aluminum side.[167,322,323] Sahu et al.[322] showed the tool offset and plunging depth scheme in Figure 16. Safi et al.[324] found that preheating of aluminum to copper dissimilar joints up to 125°C could improve the mechanical properties of the welds.

It should be emphasized that brittle intermetallic compounds with low melting point eutectics, such as AlCu, Al_2Cu and Al_4Cu_9, were easy to form in dissimilar FSW aluminum to copper joints.[12,165,325] Xue et al.[325] pointed out that a thin layer of intermetallic compounds ($\sim$1 μm) in the interface between aluminum and copper was the key to obtain high-quality FSW Al-Cu joints and such a intermetallic compound layer consisted of two sub-layers Al_2Cu and Al_4Cu_9, as shown in Figure 17. Zhang et al.[326] revealed that underwater friciton stir lap welding (FSLW) of aluminum to copper could hinder the development of intermetallic compounds.

2.6.4. Dissimilar welding of aluminum to steel

Desirable combination of aluminum and stainless steel is promising to execute the sophisticated function and structural designs in aerospace and automotive industries for superior fuel efficiency, increased fly range, low-weight-products, and better air pollution control.[287,327] However, FSW of aluminum and steel is always a global challege due to their large difference of melting points, and heat transfer.[162,287] Hussein et al.[327] presented a systematic review of the FSW of aluminum to steel.

Zheng et al.[328] reported dissimilar FSW of 6061Al alloy to 316 stainless steel using Zn as a filler metal. Fei et al.[288] used Ni and Zn as filling material during laser-assisted FSW of Q235 steel to 6061Al-T6 alloy. Kannan et al.[329] reported that the influence of silver interlayer in dissimilar 6061Al-T6 MMCs to 304 stainless steel.

Uzun et al.[162] reported the dissimilar FSW of 6013Al-T4 alloy to X5CrNi18-10 stainless steel. The results indicated that the fatigue properties of dissimilar joints were approximately 30% lower than that of the 6013Al-T6 alloy BM.[162] Yazdipour et al.[291] studied the effect of rotational and traverse speeds on the dissimilar butt FSW of 5083Al-H321 alloy to 316L stainless steel. The results indicated that with increasing the rotational speed, the

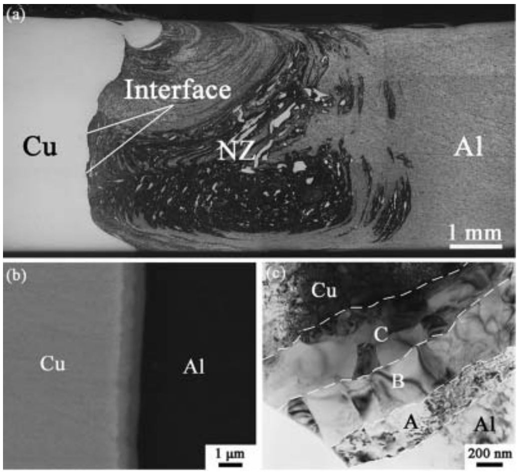

Figure 17. (a) OM of as-FSW aluminum to copper joint, microstructure of Al-Cu interface for (b) SEM back scattered electron image (BSEI) and (c) TEM bright field image. (© Springer. Reprinted with permis sion from Xue et al.[325] Permission to reuse has been obtained from the rightsholder.)

tensile strength of the dissimilar joints increased up to a maximum value and then decrease.[291]

For dissimilar FSW of aluminum to steel, a complicated interfacial region formed due to the complex deformation and the lack of diffusion time. Similar to conventional fusion welding methods, the formation of brittle iron-aluminum intermetallic compound layer represents the main issue in dissimilar FSW of aluminum to steel.[327] It was reported that the FSW interface of aluminum and stainless steel contained Fe_2Al_5, $FeAl_3$, Fe_3Al, FeAl, and Al_4Fe.[284,286,287,291,292,330] Lee et al.[284] indicated that the interfacial reaction layers in the FSW joints of 304 steel and 6056Al alloy consisted of UFG grains and the Al_4Fe intermetallic compounds.

Tanaka et al.[285] reported the the joint strength in dissimlar FSW of 7075Al-T6 alloy to mild steel increased with reduction in thickness of the inermetallic compound at the weld interface. The sound joints between dissimilar FSW of aluminum to steel enable the multi-material design methodologies.[286] So far, Honda developed a new robotic FSW machine for obtaining sound FSW joints of aluminum to steel.[327]

2.7. Friction stir lap/spot welding

FSLW is of importance from the industrial application point.[331,332] Two sheets were lap combined with an overlap area and then FSWed along the center line of the overlap area, as shown in Figure 18.[333] Yue et al.[333] found that lap width of the joint using the reverse-threaded pin was much bigger than that of the full-threaded pin in the FSLWed alclad 2024Al alloy, as shown in Figure 19.

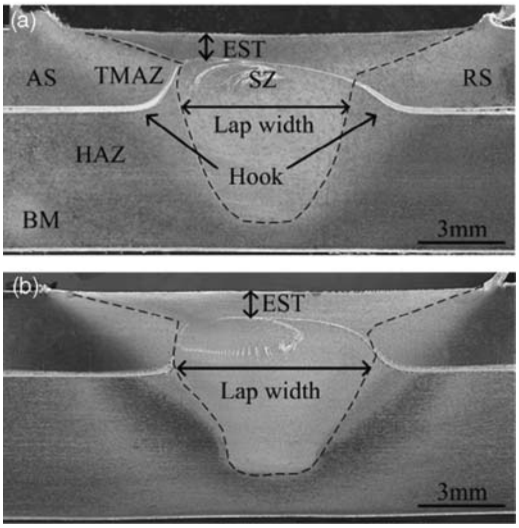

Figure 19. Cross-section of FSLW joints using different tools: (a) full-threaded pin; (b) reverse-threaded pin. (© Elsevier. Reprinted with permission from Yue et al.[333] Permission to reuse must be obtained from the rightsholder.)

Chen et al.[334] reported that a conversion zone existed between the NZ and the lower sheet metal which contained intermetallic compounds $Al_{12}Mg_{17}$, Al_3Mg_2, and Mg_2Si in FSLW of Al-Si alloy and AZ31 magnesium alloy. Firouzdor et al.[320] observed the formation of intermetallic compounds, which were identified as Al_3Mg_2 and $Al_{12}Mg_{17}$, in dissimilar FSLW of 6061Al alloy to AZ31 magnesium alloy, as shown in Figure 20. A novel self-riveting FSLW technique was developed by the prefabricated holes to realize effective joining of 6082Al-T6 alloy to QSTE340TM steel, as shown in Figure 21.[335]

Friction stir spot welded (FSSW) joint is made by plunging the rotating tool into and out of two overlapping sheets at a single location.[191,192] When the pin penetrates into the contacting sheets, a NZ is formed comprising DRX material and a keyhole region is left in the welded component when the rotating tool is retracted.[192] A low-magnification overview of the cross-section of FSSW joint was shown in Figure 22.[336] D'Urso and Giardini[337] reported how the FSSW process parameters affected the thermal distribution

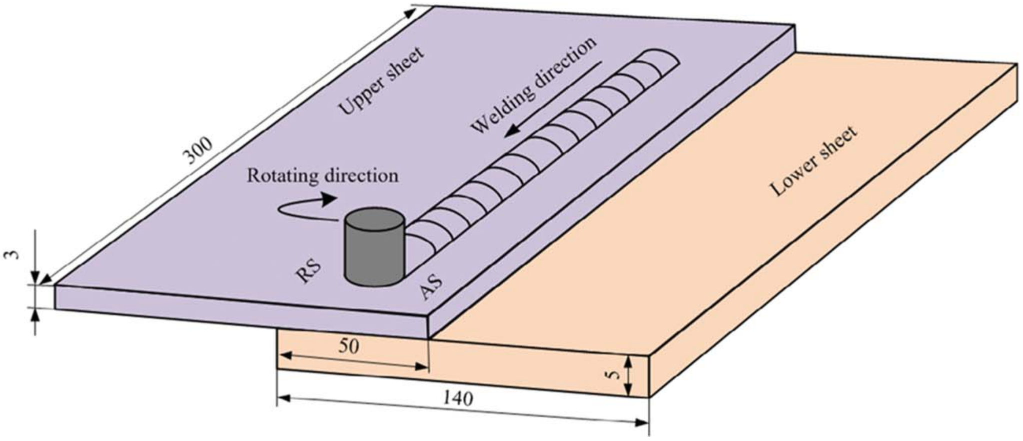

Figure 18. Schematic of friction stir lap welding (FSLW). (© Elsevier. Reprinted with permission from Yue et al.[333] Permission to reuse has been obtained from the rightsholder.)

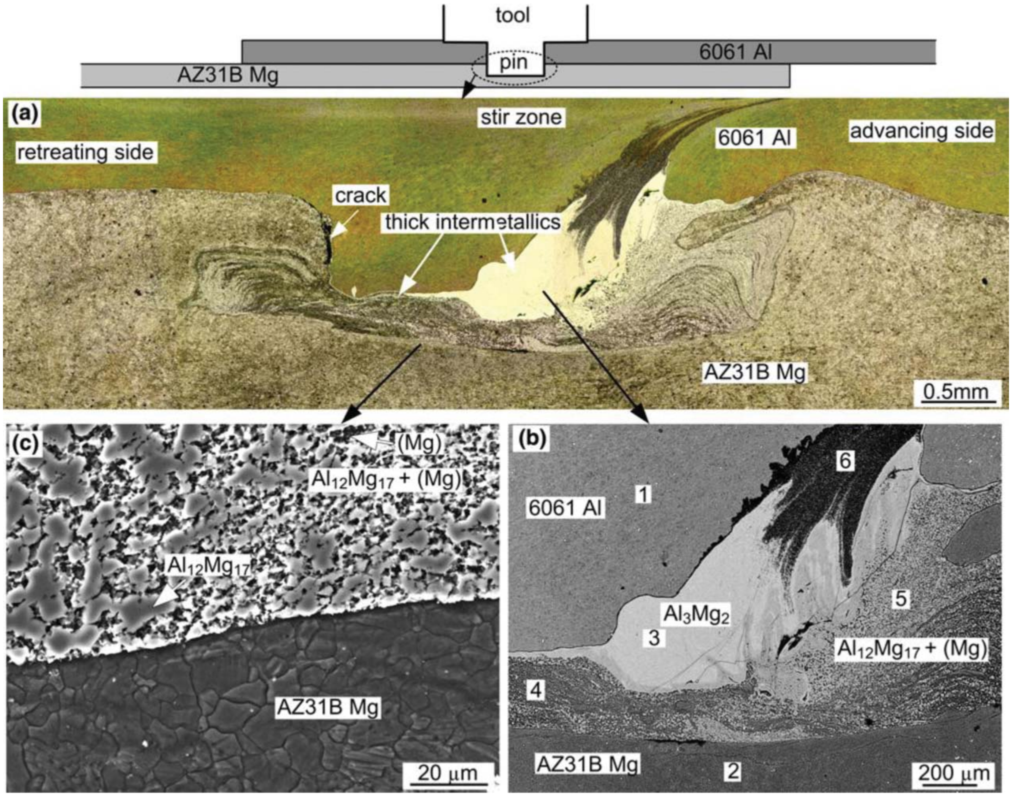
tool
6061 Al
pin
AZ31B Mg
(a)
stir zone
retreating side
6061 Al
advancing side
crack
thick intermetallics
AZ31B Mg
0.5mm
(c)
(Mg)
Al12Mg17 + (Mg)
Al12Mg17
AZ31B Mg
20 µm
(b)
6061 Al
1
6
Al3Mg2
3
5
Al12Mg17 + (Mg)
4
AZ31B Mg
2
200 µm

Figure 20. Transverse cross section of a lap weld: (a) OM, (b) and (c) SEM-BSE images of intermetallic compounds. (2.3 mm pin length, 1400 rpm-38 mm/min). (© Springer. Reprinted with permission from Firouzdor et al.[320] Permission to reuse must be obtained from the rightsholder.)

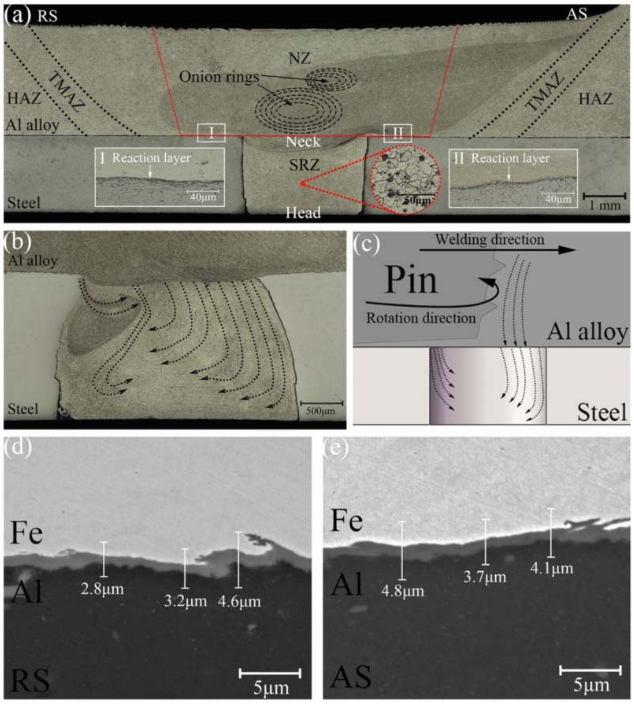
(a) RS
AS
NZ
Onion rings
TMAZ
HAZ
Al alloy
TMAZ
HAZ
I
II
Neck
SRZ
Head
I Reaction layer
II Reaction layer
Steel
40µm
50µm
40µm
1 mm
(b)
Al alloy
Steel
500µm
(c)
Welding direction
Pin
Rotation direction
Al alloy
Steel
(d)
Fe
Al
2.8µm
3.2µm
4.6µm
RS
5µm
(e)
Fe
Al
4.8µm
3.7µm
4.1µm
AS
5µm

Figure 21. Optical macrograph of (a) joint cross-section and (b) self-riveting structure of longitudinal-section; (c) flow model; joint interface on (d) RS and (e) AS. (© Elsevier. Reprinted with permission from Huang et al.[335] Permission to reuse must be obtained from the rightsholder.)

in the welding region, the welding forces and mechanical properties of the FSSW 7050Al alloys. Tozaki et al.[338] reported a newly developed tool without probe for FSSW of 6061Al-T4 alloy. Jedrasiak et al.[339] successfully predicted the thermal histories for a range of process conditions of similar Al-Al and dissimilar Al-steel FSSW.

In order to solve the size limitation problem and to extend the application field of BMGs, Shin et al.[340,341] studied the characteristic of FSSW of Zr-based BMG sheets and dissimilar FSSW of Zr-based BMG to 5xxx-series aluminum alloys. The results indicated that the tool geometry influenced the welding performance of the BMG alloy to aluminum alloys at small tool plunge depth and the extent of BMG particles penetrated onto the aluminum alloy side.[341]

Lambiase et al.[342] studied the effect of tool geometry on loads developing in FSSW of polycarbonate sheets. The transparency of polycarbonate was exploited to capture the material flow during FSSW process, as shown in Figure 23.[342]

3. Microstructural characteristics

Murr et al.[343] reported the adiabatic shear structures and DRX in FSW/FSP, where the SPD and heat input

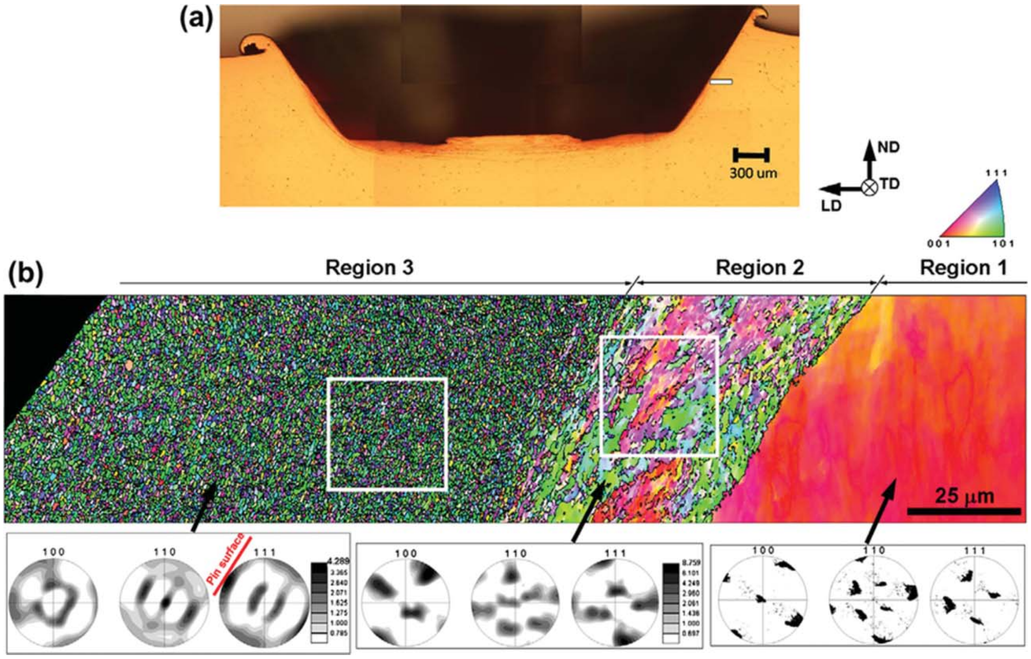
(a)
300 um
ND
TD
LD
111
001
101
(b)
Region 3
Region 2
Region 1
25 µm
100
110
111
Pin surface

Figure 22. Pin-plunging step: low-magnification overview (a) and EBSD map with superimposed HAGBs (black lines) (b). (© Elsevier. Reprinted with permission from Kooi et al.[336] Permission to reuse has been obtained from the rightsholder.)

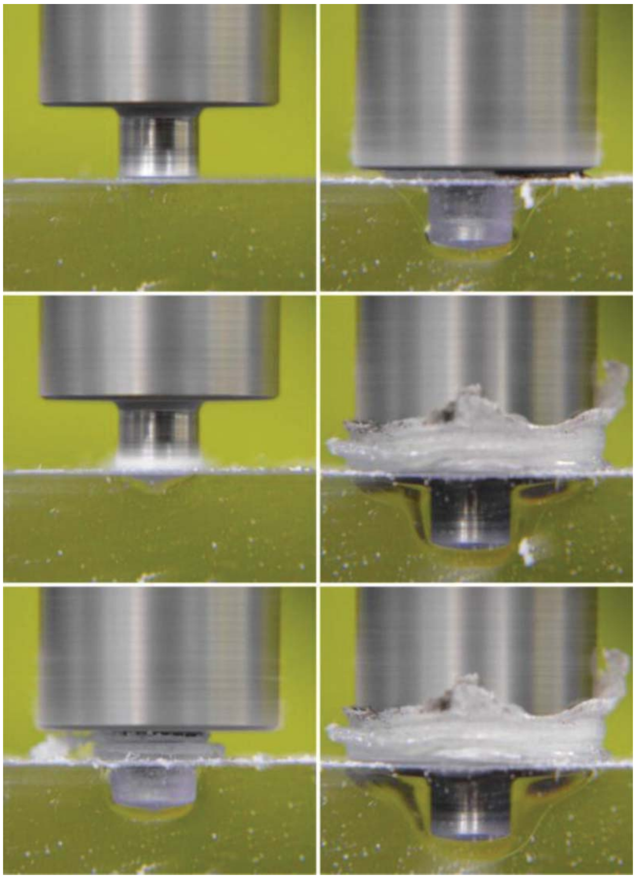

Figure 23 .Macrograph of material flow during FSSW of polycarbonate. (© Springer. Reprinted with permission from Lambiase et al.[342] Permission to reuse must be obtained from the rightsholder.)

produced fine equiaxed grains by DRX. The solid-state nature and the gradient in the strain, strain rate, and temperature in the FSW/FSP process resulted in a highly characteristic microstructure, which can be divided into the following zones, as shown in Figure 24.[10,344]

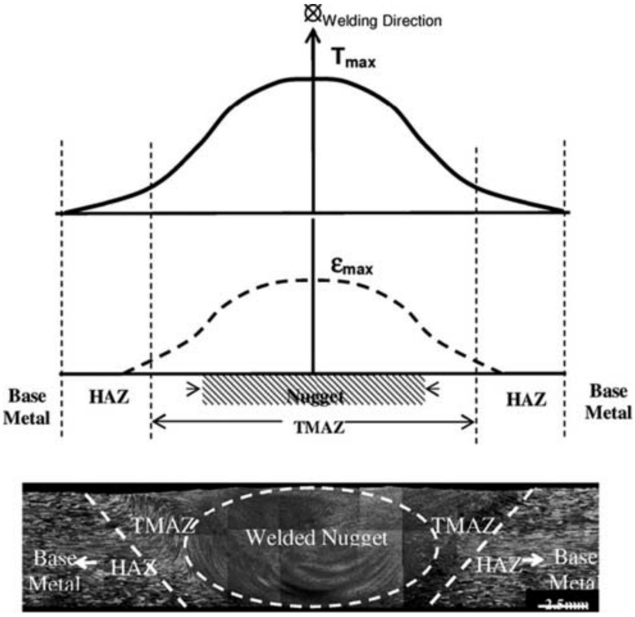
Welding Direction
Tmax
εmax
Base Metal
HAZ
Nugget
TMAZ
HAZ
Base Metal
TMAZ
Welded Nugget
TMAZ
Base Metal
HAZ
HAZ
Base Metal
2.5mm

Figure 24. Schematic of the temperature distribution, strain distribution and macrograph showing the microstrcutral zones in a FSW. (© Elsevier. Reprinted with permission from Simar et al.[10] Permission to reuse must be obtained from the rightsholder.) (© Springer. Reprinted with permission from Gallais et al.[344] Permission to reuse must be obtained from the rightsholder.)

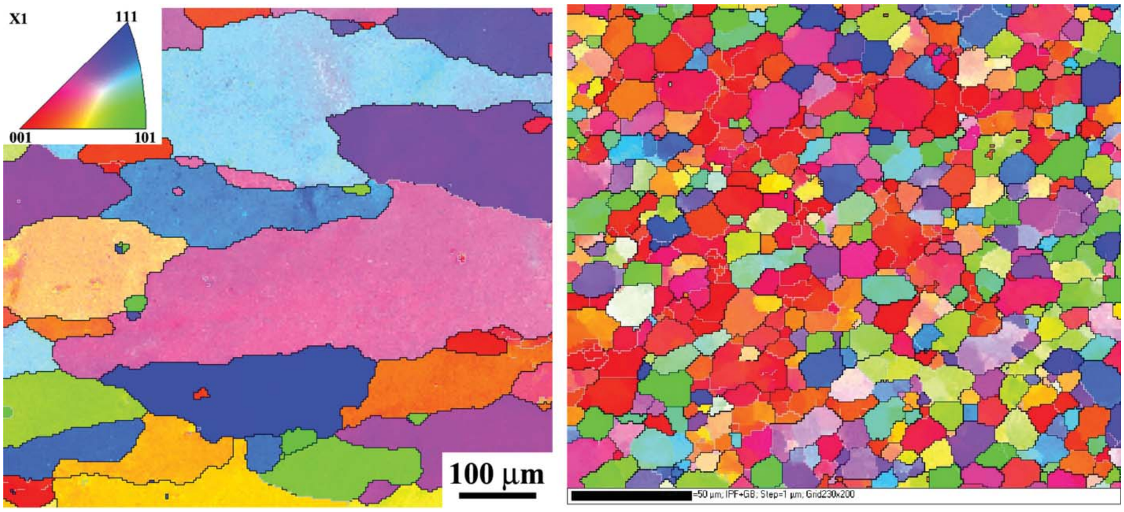

(a) (b)

Figure 25. Microstructure of 6061Al-T651 alloy: (a) EBSD orientation map of BM and (b) EBSD orientation map of NZ (our unpublished data). (© Springer. Reprinted with permission from Feng et al.[212] Permission to reuse must be obtained from the rightsholder.)

(1) *Nugget zone (NZ, also called stir zone (SZ))*

The NZ, located in the center of the weld, is characterized by a fine and equiaxed recrystallized grain structure. For instance, the large, elongated, pancake-shaped grains in the 6061Al-T651 alloy have been refined into fine recrystallized grains (Figure 25).[212] It is believed that the NZ material experienced SPD at a high strain rate of 10^0–10^2 s^{-1} and a cumulative strain of up to ~40[74,345] and peak temperatures in this region could reach a range of 0.8–0.95 T_m, depending on the material, tool design and operating conditions.[15,31,346] Under intense plastic deformation and high temperature exposure, DRX occurred in the NZ, resulting in the formation of fine and equiaxed grains.

(2) *Thermomechanically affected zone (TMAZ)*

The TMAZ experiences a lesser extent of strains and strain rates as well as a lower peak temperature. In this region, DRX usually does not occur or only partially occur. The characteristic elongated grains in the TMAZ exhibit a flow pattern around the NZ.

(3) *Heat-affected zone (HAZ)*

The HAZ, which is adjacent to the TMAZ, experiences only a thermal cycle, without undergoing any plastic deformation. It is similar to the HAZ in other types of welding.

(4) *Base metal (BM)*

The BM is the unaffected material, far from the weld seam, which experiences neither the thermal cycles nor plastic deformation.

3.1. Recrystallization mechanism

Recovery, recrystallization and grain growth are an evolving and important topic in the area of FSW/FSP. It remains a very active research area. During FSW/FSP, the material that flows around the tool undergoes SPD at elevated temperatures, thereby inducing the occurrence of DRX. It is now well recognized that DRX results in the generation of fine and equiaxed grains ranging from nano-scale to micro-scale in the NZ of FSW/FSP aluminum alloys,[42,225,347,348] magnesium alloys,[3,74,79,86,91,349] copper alloys,[62] steel,[121,126] NiAl bronze,[350] titanium alloys,[104,105,109,351,352] and MMCs.[152,153] The DRX mechanisms during FSW/FSP have received a considerable attention and have been widely investigated on the basis of microstructural evolution and dislocation processes:[35,42,86,225,353]

(1) *Continuous DRX (CDRX)*:

CDRX involves the formation of arrays of low angle boundaries (LAGBs) and a gradual increase in the boundary misorientations during hot deformation, finally leading to the development of new grains.

(2) *Discontinuous DRX (DDRX)*:

DDRX occurs by nucleation and growth of new grains.

(3) *Geometric DRX (GDRX)*:

GDRX, resulting from the impingement of serrated grain boundaries, can occur when grains are extremely elongated by severe hot deformation.

(4) *Twinning DRX (TDRX)*:

TDRX is an important mechanism for plastic deformation in hexagonal close-packed (hcp) metals, e.g., magnesium alloys.[86] TDRX mechanism involves the three elementary process: nucleation, transformation of twin boundaries into random boundaries, and grain growth.[354]

(5) *Particle-stimulated nucleation (PSN) of recrystallization*

> PSN has been widely observed in many alloys, including aluminum, iron, copper, nickel, and MMCs.[152,355,356]

It should be emphasized that CDRX and DDRX were attributed to a phenomenological categorization. CDRX may occur uniformly, so that the microstructures evolve gradually without identifiable nucleation and growth stages. Alternatively, DDRX may occur heterogeneously throughout the material, and they may be described in terms of nucleation and growth stages.[355] Interestingly, these mechanisms can occur synchronously and their respective contributions are difficult to be isolate on the basis of experimental data.[353] Furthermore, it is worth mentioning that all the proposed recrystallization mechanisms during FSW/FSP have been based on the observations of the final structure.[225]

Static recovery and recrystallization can occur very rapidly at elevated temperatures, and there is a considerable time lapse after the NZ material has been deformed until the weld has cooled, which could easily confuse microstructural interpretation.[200] In this case, some of the nuclei probably increased their size by high-angle grain boundary (HAGB) migration. The final grain size is generally determined by the ratio of the rate of nucleation to the rate of growth of the new grains.[357] It was reported that deformation efficiency for DRX depends on the composition, crystal structure, deformation history, and stacking-fault energy (SFE) of an alloy.[358] Table 1 lists the summary of the SFE of some alloys.[355,359–362]

In an attempt to provide a better understanding of the material flow and grain structure formation during FSW, the so-called "stop-action" technique has been developed by Colligan,[363] and popularized by Prangnell and Heason[200] and Suhuddin et al.[364] Recently, in-situ time-resolved neutron diffraction measurements were performed during FSW of 6061Al-T6 alloy by Woo et al.[199]. The results indicated that the subgrain size was about 160 nm and the dislocation density was approximately 3.2×10^{15} m^{-2} during FSW, which was 7 times higher than the initial dislocation density of 4.5×10^{14} m^{-2} in the BM.[199]

3.1.1. Continuous dynamic recrystallization

DRX, which occurs during straining, has long been considered to be restricted to low SFE metals, e.g., copper, α-brass, γ-iron, and austenitic steels. In the case of low SFE metals, dislocation climb is difficult, and little recovery of the dislocation structures normally occurs prior to recrystallization.[355] In the high SFE metals, e.g., aluminum, α-iron, ferritic steels, where the dislocation mobility was much larger, dynamic recovery (DRV) was assumed to be the only operating mechanism.[355,365] However, recent studies indicated the presence of fine dynamically recrystallized grains in FSP 2024Al which had predominant HAGBs.[43]

Table 1. Characteristics of metallic materials based on Al, Mg, Cu, Fe, and Ti.[355,359–362]

	Al	Mg	Cu	Fe	Ni	Ti
Melting temperature, °C	660	649	1085	1538	1455	1668
Room temperature E, GPa	72	45	115	215	200	103
Density, g/cm^3	2.7	1.8	8.9	7.9	8.9	4.5
Stacking fault energy, mJm^{-2}	~170	60–78	~80	~20	128	310

Restoration of aluminum alloys by DRV and DRX has been well documented in Doherty et al.[366] Several mechanisms of CDRX by which subgrains rotate and achieve a high misorientation have been proposed, including lattice rotation associated with slip, lattice rotation associated with boundary sliding, and subgrain growth.[355]

A CDRX mechanism has been proposed to involve the absorption of dislocations by subgrain boundaries, under conditions where the subgrains are pinned by second-phase particles preventing growth, which increase the misorientation until they become HAGBs at the extremely high strain levels seen in FSW.[200] However, high-strain torsion tests on aluminum alloys showed that during hot deformation subgrain misorientations generally reach a saturation state at a relatively low levels of ~3° and do not increase significantly with further straining. The increase in the misorientation of a subgrain θ in a homogeneously deformed crystal, due to dislocation adsorption, has been estimated by Pantleon[367] as a function of shear strain, γ:

$$\theta = \sqrt{\gamma b \,/\, d} \tag{6}$$

where b is the Burgers vector and d is the cell size. This relationship predicts that θ increases very slowly even at large strains. For example, for a typical value of b/d of $\sim 10^{-4}$, θ is only 3.7° at $\gamma = 40$, and a strain amount as high as nearly 10^3 can merely bring in a misorientation of 15° required to form a HAGB.[200]

The CDRX was proposed as an operative dynamic nucleation mechanism during FSW of 6061Al-T6 alloy[368] and Al-Li-Cu alloys.[35] Jata and Semiatin[35] suggested a dislocation glide assisted subgrain rotation model. In their model, dislocation glide gives rise to a gradual relative rotation of adjacent subgrains. However, it is important to note that many recrystallized grains in the NZ are finer than the original subgrains. Thus. Su et al.[42] suggested a CDRX model on the basis of DRV. Fratini and Buffa[369] reported a model on CDRX in a FSW 6082Al-T6 alloy by a neural-network-based approach. Buffa et al.[370] further developed two analytical models aimed to determine the average grain size due to

CDRX phenomena in the FSW of 7075Al-T6 alloys, which have been implemented in a 3D FEM model, and numerical analyses of the welding processes have been performed to verify their effectiveness.

3.1.2. Discontinuous dynamic recrystallization

Alternatively, DDRX has been recently proposed as an operative mechanism for dynamic nucleation process in FSW/FSP aluminum alloys.[225,347,348] During CDRX new grains develop via a gradual increase in misorientation between subgrains.[225] In contrast, during DDRX new grains exhibiting HAGBs evolve, i.e., dynamic nucleation followed by grain growth from the migration of HAGBs. Su et al.[225] reported that DDRX is the mechanism responsible for the nanocrystalline creation in the FSW/FSP aluminum alloys. It is apparent that the nanocrystalline structures are the result of DDRX under very large strain and very high strain rate at elevated temperatures.[225] While the mechanism and kinetics of the process are not clear, the formation of nano-grained structure suggests a very high nucleation rate during DRX.[225] A condition for the initiation of DDRX may be given by[13]:

$$\rho_m^3 \dot{\varepsilon} > \frac{2\gamma_b}{KLMGb^5} \tag{7}$$

where ρ_m is the mobile dislocation density, $\dot{\varepsilon}$ is the strain rate, γ_b is the grain boundary energy, K is a constant fraction of the dislocation line energy that is stored in the newly formed grains, L is the mean slip distance of dislocations in these grains, M is the boundary mobility, G is the shear modulus, and b is the Burgers vector.

The inequality suggests a strong dependence of the conditions for DDRX on the mobile dislocation density:[13] a low SFE tends to suppress recovery, leading to high values of ρ_m. In contrast, for the materials of high SFE, recovery reduces ρ_m, thereby precluding DDRX, especially at high strain rates.

3.1.3. Geometric dynamic recrystallization

GDRX occurs when grain boundaries start to impinge during deformation because of the geometric requirements of strain.[371] The onset of GDRX may be observed as the strain increases during DRV when the separation of prior boundaries approaches a subgrain size.[13,355,366] Giles et al.[372] reported that the persistence of a shear type deformation texture in the NZ reflected DRV and GDRX during FSP of 2099Al-T8 alloy. Robson et al.[373] developed a new model for grain formation in the NZ based on GDRX followed by the grain growth to predict the grain size in a FSW 2524Al alloy.

GDRX mechanism requires a certain degree of boundary mobility, which allows wavy boundaries to develop and pinch off driven by the equilibration of boundary tensions.[200] If GDRX occurs when the boundary spacing approaches one subgrain width, the strain for the onset of GDRX in plane strain compression can be predicted by the following equation:[374]

$$\varepsilon_{cri} = \ln\left(Z^{1/m} D_0\right) + C, \tag{8}$$

where Z is the Zener-Holloman parameter, which determines the subgrain size for a given temperature and strain rate, D_0 is the original grain size and m and C are constants.

GDRX is thus more likely at high temperatures and low strain rates.[200] However, pinning particles will delay GDRX to higher strains than predicted by Eq. (8), due to their effect on reducing boundary mobility.[374] The theoretical reduction of a homogeneously deformed grain in a simple shear can be calculated from[375]

$$d = \frac{d_0}{\left(\sqrt{1+\gamma^2}\right)} \tag{9}$$

where d_o is the initial grain width and d is the grain width after a shear strain, γ.

3.1.4. Twinning dynamic recrystallization

Twinning is an important deformation mode in face-centered-cubic (fcc) metals with $\gamma_{SFE} < 25$ mJm^{-2} (γ_{SFE} is SFE of metals) and in all hcp metals.[355] It may also occur in fcc metals with high values of γ_{SFE} and in body-centered-cubic (bcc) metals if deformation occurs at low temperatures or high strain rates.[355]

Murr[376] measured the energy of a coherent twin boundary in a pure aluminum at 450°C to be 0.23 of the energy of a HAGB. Humphreys and Ferry[377] indicated that annealing twins may be formed during PSN at large second-phase particles in aluminum alloys.

The recrystallization is a nucleation and growth process. Favored sites for the recrystallization nuclei include grain boundaries, phase interfaces, twin boundaries, deformation bands, and the surface of the materials, which are characterized as regions of heavy distortion, high dislocation density, or strong orientation gradients.[378] Nucleation with low to medium SFEs can occur frequently by twinning.[379,380] subgrain rotation,[381] and bulging.[382,383] Generally, twinning takes place at the early stage of plastic flow. Despite the limited contribution of twinning itself to the overall plasticity, the abrupt change in the orientation due to twinning would facilitate the reactivation of other slip systems.[384] Such a “twin” DRX was associated with the following processes.[379]

(1) The nucleation occurred either through the intersection of various systems or variants of twins or the rearrangement of lattice dislocations within the twin lamellae.
(2) The twin boundaries were changed into random HAGBs at high strains due to their interaction with mobile dislocations.

3.1.5. Particle-stimulated nucleation of recrystallization

In MMCs, DRX nucleated in regions of very high dislocation density in the vicinity of reinforcement particles.[385] Inem[386] reported that the SiC particles provided more nucleation sites for the new recrystallized grains by increasing local strain in the matrix and causing lattice misorientation. The particles play an important role in controlling the recrystallized grain size by PSN.[152] If each particle produces one recrystallized grain, the resultant grain size D would be directly related to the volume fraction F_v and the diameter of particles d by:

$$D \approx d{F_v}^{-1/3} \tag{10}$$

3.2. Grain structures

A grain boundary, characterized by five degrees of freedom,[355] is defined as the surface between any two grains that have the same composition and crystal structure but different orientations. Based on the symmetry operation, four types of grain boundaries can be specified:[387] twist, tilt, mixed, and twin. Grain size and the characteristics of the grain boundaries play a key role in determining various physical and mechanical properties.[388]

3.2.1. Grain size

Rhodes et al.[348] reported that the initial sizes of newly recrystallized grains are on the order of 25–100 nm in a FSP 7050Al alloy by using a mixed coolant of dry ice with isopropyl alcohol, which is significantly smaller than the size of the pre-existing sub-grains, typically 12 μm.[348] It is, therefore, postulated that the 2–5 μm grains usually observed in the FSW/FSP aluminum alloys arise as a result of nucleation and growth within a heavily deformed structure.[240]

The nanocrystalline structures, produced using the FSP technique combined with rapid cooling by Su et al.,[225,347] consisted of HAGBs and were free of dislocation cell structures. However, dislocations and recovery structures were observed in the large grains of samples at slower cooling rates.[225] Similarly, Gerlich and Shibayanagi[389] reported that the NZ in a friction stir spot welded Al-4.3Cu-1.4Mg alloy contained random boundaries, where grains with a dimension of <250 nm were free of dislocations, and grains having an average dimension of >500 nm possessed high dislocation densities. The intragranular strain during grain boundary sliding (GBS) decreases with decreasing grain size and accounts for the low frequency of dislocations within grains having a diameter of <250 nm.[389]

Jata and Semiatin[35] and Commin et al.[85] tried to explain the relationship between the processing parameters and the resulting microstructure in FSW Al-Li-Cu alloy and AZ31 magnesium alloys, respectively, via a temperature-compensated strain rate Z:

$$Z = \dot{\varepsilon}\exp\left(Q/RT\right), \tag{11}$$

where $\dot{\varepsilon}$, Q, R, and T are the strain rate, activation energy, gas constant, and absolute temperature, respectively.

It is well known that the size of dynamically recrystallized grains is related to the Z value when the strain introduced into the material is high. The Z is routinely used to explain the development in the structure-property relationships of hot deformed metals. The relationship between the NZ temperature and the processing parameters (mainly rotational rate ω and welding speed ν) for the aluminum alloys could be expressed as Eq. (12):[85]

$$\frac{T}{T_m} = K\left(\frac{\omega^2}{\nu\times 10^4}\right)^a \tag{12}$$

where T_m is the melting point in Kelvin, K and α are two constants, where the exponent α was reported to range from 0.04–0.06, the constant K is between 0.65 and 0.75.

This means that $\dot{\varepsilon}$ and T during FSW are important factors for understanding the microstructural evolution of the NZ.

Sato et al.[15] reported that the recrystallized grain size of the NZ increased exponentially with increasing maximum temperature. The relationship between the grain size and the maximum temperature followed the static grain-growth equation:

$$D^2 - D_0^2 = A\exp(-Q/RT)t \tag{13}$$

where in Eq. (13), D_0 and D are the initial grain size and residual recrystallized grain size, A is a constant, Q is the appropriate activation energy for grain growth, R is the gas constant, T is the absolute temperature, and t is the time.

The effect of strain rate on the grain size in FSW of 1050Al alloy is summarized in Figure 26.[23] It is seen that the grain size decreases exponentially with increasing strain rate, where the strain rate during FSW was

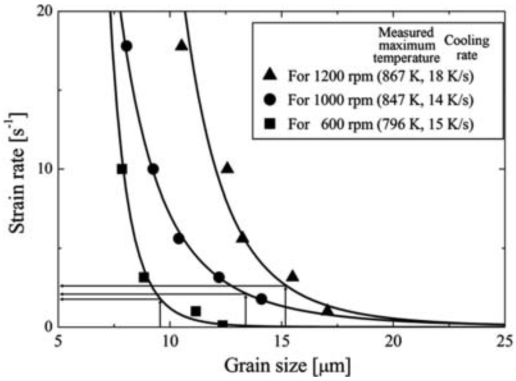

Figure 26. Relationship between grain size after thermomechanical treatments and effective strain rate after FSW. The grain sizes of NZ at three rotational speeds are shown with arrows on the corresponding curves. (© Elsevier. Reprinted with permission from Masaki et al.[23] Permission to reuse must be obtained from the rightsholder.)

estimated to be between 1.7 and 2.7 s^{-1}, which was hardly affected by the rotational rate.[23]

3.2.2. Characteristics of grain boundary

The grain boundary character is usually quantified using the misorientation angle across grain boundaries.[390] Generally, grain boundaries are divided into LAGBs, where the misorientation is less than a certain angle, typically 10–15°, and HAGBs where the misorientation is greater than 10–15°.[355] It has long been recognized that the mobility of LAGBs is significantly lower than that of HAGBs.[355] Compared with the LAGBs, the incoherent HAGBs exhibit a higher surface energy, typically about 0.3–0.5 J/m^2.

The HAGBs in the NZ were first reported in a FSP 7075Al alloy by Mishra and Mahoney,[391] and later in a FSP 2024Al alloy by Charit and Mishra.[43] (Figure 27). Similar results have also been reported in other FSW/FSP aluminum alloys,[200,392] magnesium alloy,[86] copper,[63] and MMCs.[153] The fraction of HAGBs in FSP aluminum alloys could reach as high as 85–97%.[392] This is significantly higher than that obtained in conventional thermomechanically processed aluminum alloys, with a typical ratio of 50–65%.[393]

The HAGBs are typically of non-equilibrium nature in a high-energy state in the aluminum alloys produced by ECAP.[394,395] The physical width of a grain boundary is determined by the degree of the non-equilibrium state of grain boundary structure.[395] The boundaries produced through SPD are good sinks for dislocations.[390] Kang et al.[396] reported that compared with the BM, the TMAZ exhibits a high fraction of LAGBs which might be due to the SPD without recrystallization.

It is interesting to note that the misorientation distribution developed during FSW approaches a theoretical distribution for random orientations of fully annealed grains in cubic materials derived by Mackenzie,[397] as shown in Figure 28.[398] Similar results have been observed by Motohashi et al.[399]

3.2.3. Abnormal grain growth

AGG, sometimes called secondary recrystallization,[355] frequently occurs in the NZ of FSW/FSP aluminum alloys,[25,44,52,400,401] magnesium alloys,[78] composite,[402,403] and steel,[404] because the fine-grained structure was inherently instable, which was explained by the theory of cellular microstructure proposed by Humphreys.[405] AGG has been recognized as a critical issue during the post-processing heat treatment and superplastic forming of FSW/FSP aluminum alloys.[25,28,406,407] AGG would deteriorate the strength of FSW/FSP heat-treatable high-strength aluminum alloys[406] and steel.[404] The stability of the fine-grained microstructure at high temperatures should be an important consideration.

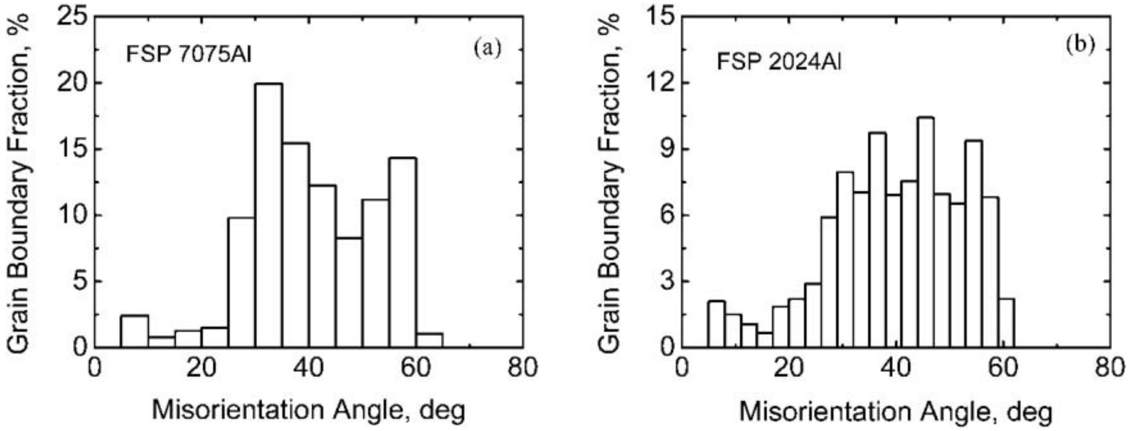

Figure 27. Grain boundary misorientation distribution in FSP aluminum alloys: (a) 7075Al alloy and (b) 2024Al alloy, indicating formation of a larger fraction of HAGBs. (© Elsevier. Reprinted with permission from Charit & Mishra.[43] Permission to reuse must be obtained from the rightsholder.)

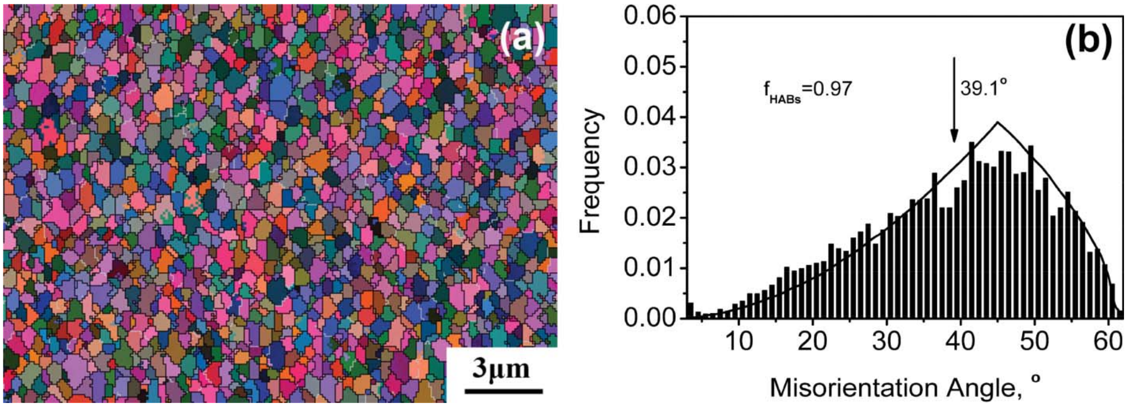

Figure 28. Microstructure of FSP Al-Mg-Sc alloy: (a) EBSD map and (b) grain boundary misorientation angle distribution. (© Elsevier. Reprinted with permission from Liu et al.[398] Permission to reuse must be obtained from the rightsholder.)

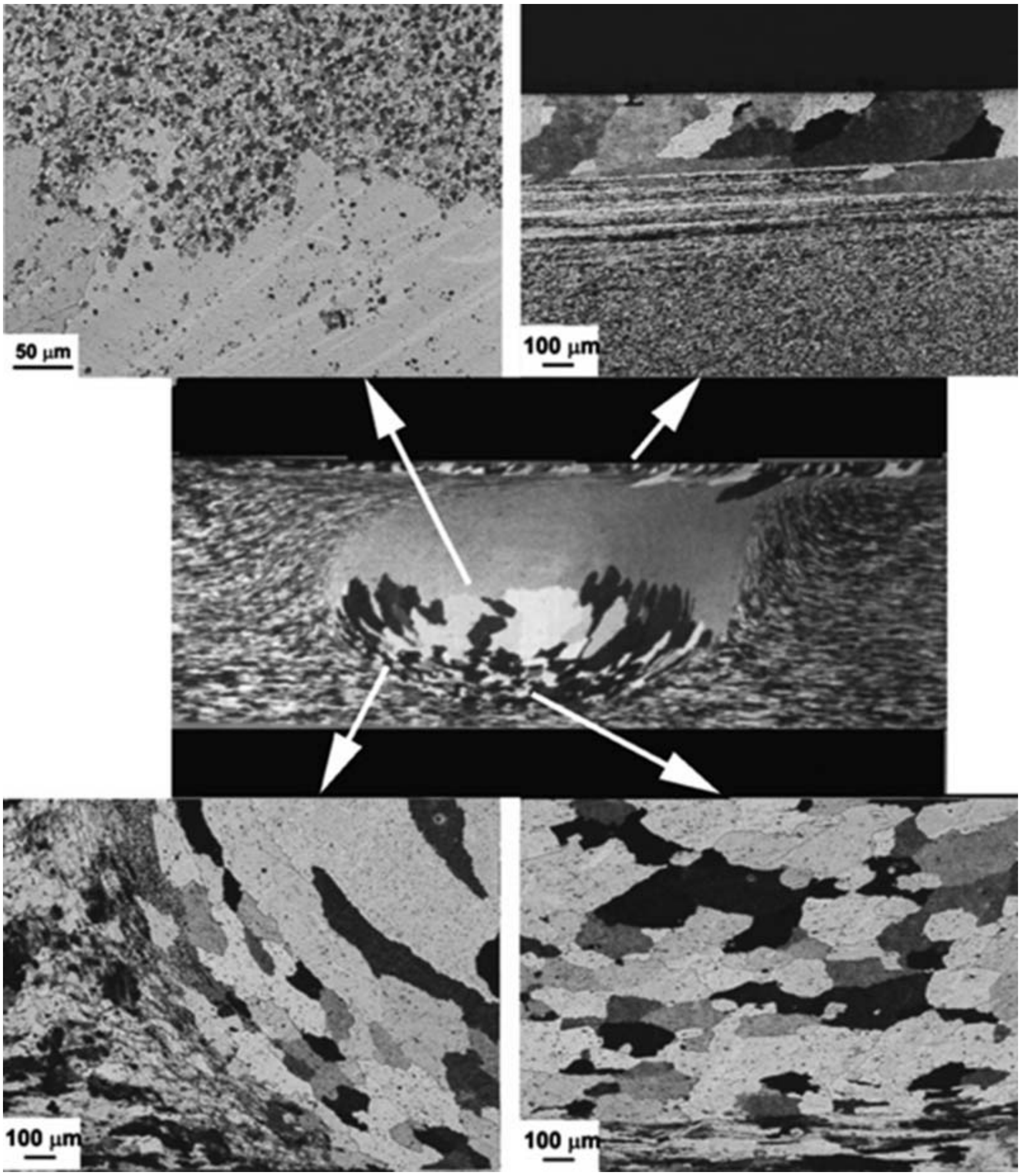

Figure 29. OMs showing the extent of AGG in a 7075Al alloy heat-treated at 490°C for 1 h. (© Elsevier. Reprinted with permission from Charit & Mishra.[25] Permission to reuse must be obtained from the rightsholder.)

Figure 29 shows the optical micrographs of a heat-treated FSP 7075Al alloy with AGG features.[25] AGG was also observed in all three FSW 6063Al, 6% B_4C/6063Al, and 10.5% B_4C/6063Al joints, as shown in Figure 30.[403] Mironov et al.[78] reported that thermal stability in different parts of the NZ was very different, grain growth was fairly abnormal and directional and the shapes of developed grains resembled flow patterns inherent to the FSW structure. They showed that all peculiarities of the grain growth behavior could be explained in terms of heterogeneous distribution of second phase particles resulting from FSW/FSP.[78] Grain coarsening often initiated at the peripheral regions around the NZ of FSW materials,[44,406] and the size of abnormally coarse grains can vary significantly across the NZ.[44,46] Development of these grains was heavily influenced by the onion ring structure,[28,44,46,406] and the growth front was macroscopically uniform while it had some extent of fluctuation from the microscopic view.[44,406] The main factors that can affect the onset of AGG are as follows:[46]

1. anisotropy in grain boundary energy and mobility;
2. reduction in pinning forces due to coarsening and/or dissolution of particles; and
3. thermodynamic driving forces due to grain size distribution.

The temperature of microstructural instability in a FSP Al-Zn-Mg-Sc alloy could be related to the dissolution of all the "metastable" Mg-Zn precipitates (shown by an arrow in Figure 31) that started dissolving before 390°C, and finally disappeared at 440°C.[46] A detailed analysis of the influence of particle coarsening and dissolution on AGG has been conducted by Humphreys.[408] The AGG was possible when the pining parameter, P, is $0.25<P<1$ ($P=\alpha F_v\overline{R}\,/\,d$, where α is a constant 3 or 6 depending on whether the particle is incoherent or coherent with the matrix, respectively, F_v the total volume fraction of particles, $\overline{R}$ the average grain radius, and d the particle diameter).[355] Charit and Mishra[46] indicated that the dissolution of Mg-Zn precipitates at the grain boundaries would gradually reduce the dimensionless pinning parameter (P), and thus the evolving microstructure moved to the regime where AGG dominates.

Attallah et al.[406] found that FSW parameters appreciably affected the extent of AGG. Mironov et al.[400] revealed that the dominated Brass {110}<112>, R {124}<211>, and S {123}<634> texture components were produced by AGG in FSW 1050Al alloy. Jana et al.[409] reported that single FSP pass runs showed some extent of AGG, whereas multi-pass runs were more resistant to AGG. Therefore, the microstructural uniformity is one key aspect for avoiding AGG.[25] FSW/FSP aluminum alloys often underwent AGG in the PWHT.[406] In order to inhibit AGG, careful attention must be given to the PWHT processing routes for FSW/FSP aluminum alloys.[407,410,411]

3.3. Dissolution and re-precipitation

Aluminum alloys are roughly classified into precipitation-hardened alloys and solid-solution-hardened

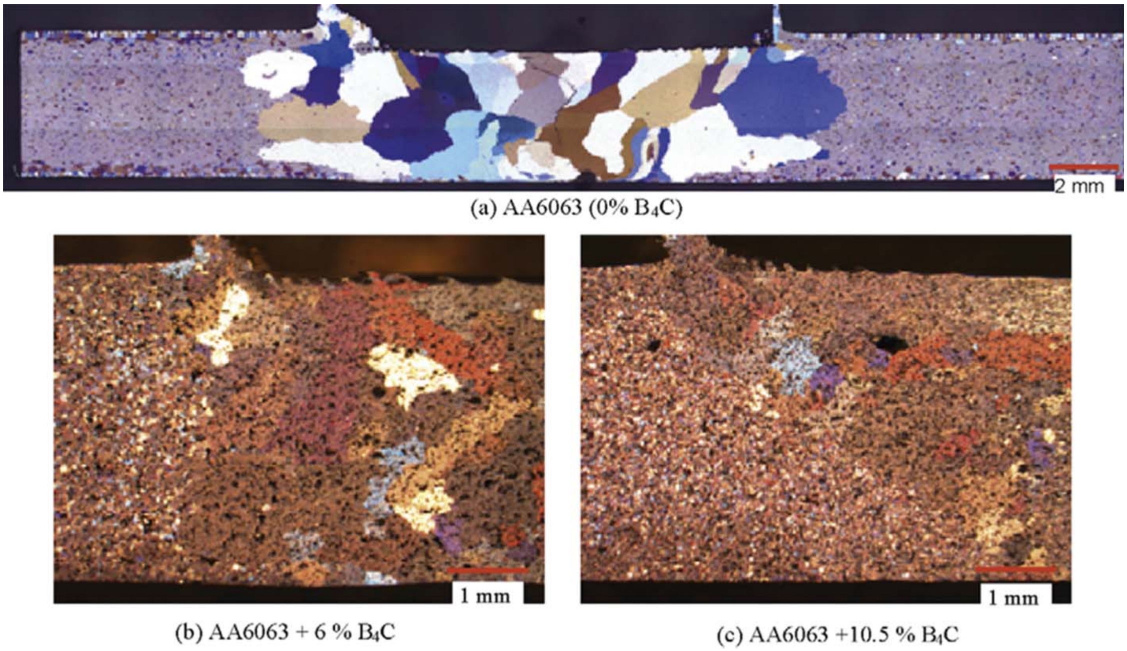

Figure 30. AGG in NZ after T6 heat treatment. (© Elsevier. Reprinted with permission from Chen et al.[403] Permission to reuse must be obtained from the rightsholder.)

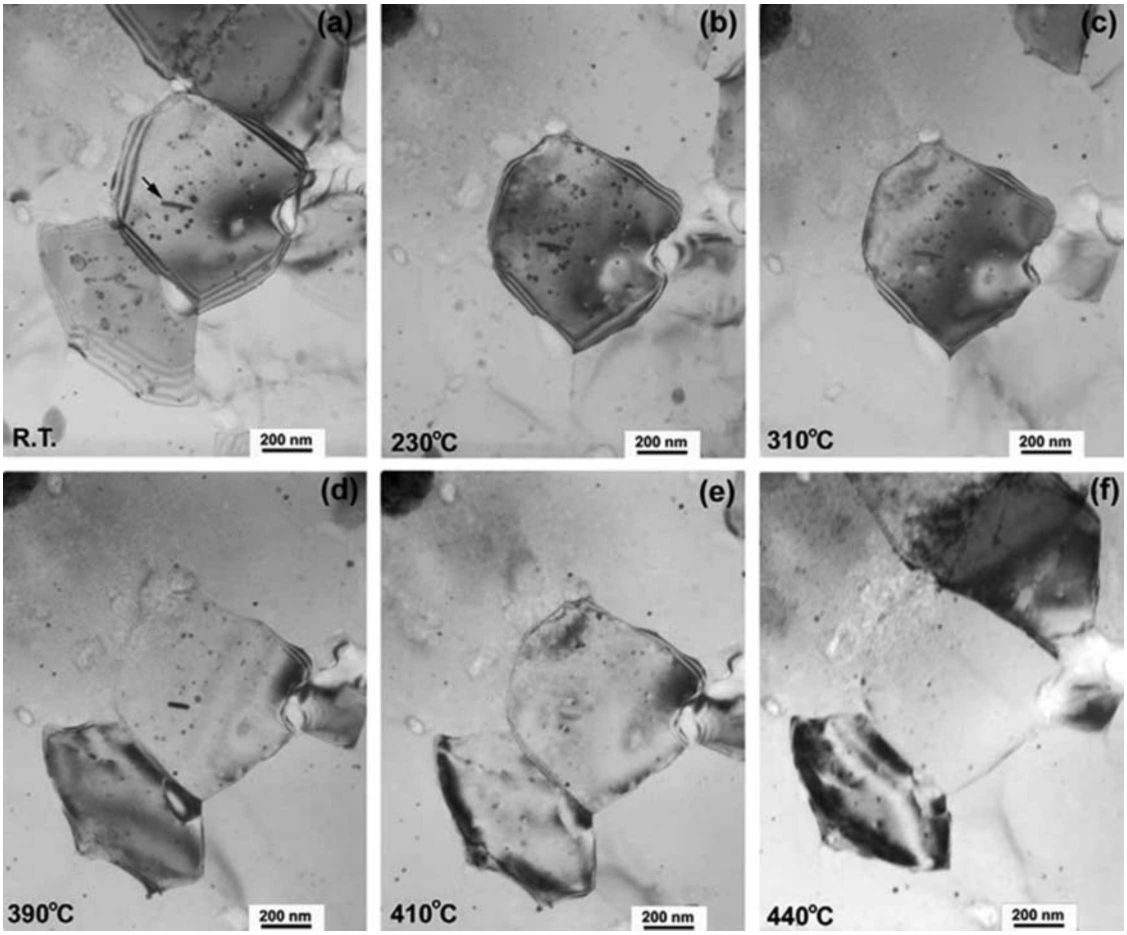

Figure 31. Bright field TEM images captured during in situ TEM heating experiment of a representative foil of FSP Al-Zn-Mg-Sc alloy sample at (a) room temperature, (b) 230°C, (c) 310°C, (d) 390°C, (e) 410°C, and (f) 440°C. (© Elsevier. Reprinted with permission from Charit & Mishra.[46] Permission to reuse must be obtained from the rightsholder.)

alloys.[40] FSW creates a softened region around the weld center in the precipitation-hardened aluminum alloys.[40,412,413] FSW could be considered as a local hot-working process. The resulting temperature gradient produced a range of precipitates from the center of the NZ to the BM.[32] A solid-state type of phase transformation occurred during cooling of the weld.[36] The precipitate distribution was strongly influenced by the thermal hysteresis.[34,42] As mentioned earlier, the maximum temperature could approach ~0.8 T_m or even 0.95 T_m[15,31] which would well exceed the solvus temperature of many precipitation-hardened aluminum alloys. As a result, the microstructure across the weld would exhibit various degrees of partial solution treatment.[14]

The aging precipitation sequences in precipitation-hardened aluminum alloys begin with the formation of intermediate phases, i.e., Guinier-Preston (GP) zones and metastable phases.[14] Two types of precipitation occur in C curves in aluminum alloys (Figure 32).[414] One is the precipitation of copper, magnesium, zinc atoms at lower temperatures (20–400°C), contributing to the age hardening. The other is the precipitation of zirconium, chrominum, manganese atoms at higher temperatures (350–550°C), contributing to inhibiting grain growth. Starink et al.[26] reported that in FSW/FSP materials, the mechanisms

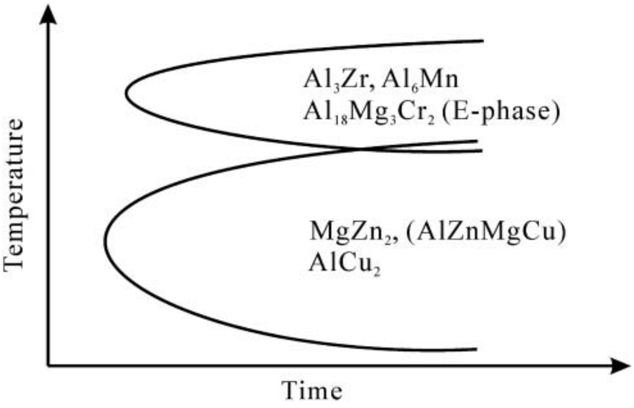

Figure 32. C-curves for precipitation in aluminum alloys. (© Trans Tech Publications. Reprinted with permission from Yoshida.[414] Permission to reuse must be obtained from the rightsholder.)

for increasing the critical resolved shear stress (CRSS) of the slip systems are:

(a) precipitation strengthening;
(b) solid solution strengthening;
(c) dislocation strengthening;
(d) grain boundary strengthening; and
(e) crystallographic orientations of grains.

Each of these factors can have a substantial influence on the strength. However, in heat-treatable alloys, the strength is generally dominated by precipitation strengthening.[26] Many types of models are available for modeling the precipitation evolution taking place during non-isothermal processes in metallic alloys.[10] These analytical models use the Johnson-Mehl, Avrami, Kolmogorov (JMAK) formalism for the nucleation and growth of the precipitates and the Whelan formalism for the dissolution process.[10]

3.3.1. 5xxx-series aluminum alloys

5xxx-series aluminum alloys, with magnesium as a major constituent up to ∼5% in solid solution,[415] are non-heat-treatable and have high strength with good ductility through cold working, together with excellent corrosion resistance and weldability.[416] Magnesium atom is larger than the parent aluminum atom in a solid solution, and this induces lattice distortion and stress field, thus increasing work-hardening rate, yield, and tensile strengths compared with commercially pure aluminum.[417]

Generally, FSW does not result in softening in the solid-solution hardened aluminum alloys.[412] Svensson et al.[418] note that the hardness profile mainly depends on the dislocation density, because the main hardening mechanism is strain hardening in this series of alloys. Since the solid-state FSP does not result in a loss of solute atoms by evaporation and segregation via solidification, solute atoms are even more homogeneously distributed in the weld, producing the homogeneous hardness profiles in FSW 5xxx-series aluminum alloys.[40]

Unlike the age hardenable aluminum alloys, the microstructure in 5xxx-series aluminum alloys is basically composed of the Al-Mg phase with small amounts of Mg_2Si, Al_3Fe, and $Al_6(Mn,Fe)$.[412,419,420] The dissolution of the iron intermetallic phases at above 320°C and the re-precipitation below 300°C suggest that the grain growth is limited either by iron solute segregation at the grain boundaries or by the Zener drag action if the solutes heterogeneously precipitate.[421] The solvus temperatures of $Al_6(Fe,Mn)$ and Mg_2Si are reported to be approximately 635°C and 637°C, respectively. These temperatures are higher than the solidus temperature of 5083Al (575°C).[40] Thus, only a nucleation, growth, and coarsening process could result in the formation of $Al_6(Fe,Mn)$ precipitates during FSP.[422]

3.3.2. 2xxx-series aluminum alloys

2xxx-series Al-Cu-(Mg) aluminum alloys are precipitation-hardened alloys with several metastable phases formed in its phase-decomposition process.[423] It is widely accepted that the phase decomposition in the Al-Cu-Mg alloys is as follows: $SSS \rightarrow GP\ zone \rightarrow \theta'' \rightarrow \theta' \rightarrow \theta$ phase (Al_2Cu)[362,424] and $SSS \rightarrow GP\ zone \rightarrow S' \rightarrow S$ phase (Al_2CuMg),[425] where SSS stands for the supersaturated solid solution. The hardening phase in the Al-Cu-Mg alloys depends on the Cu-to-Mg ratio.[198] Although, the complete precipitation sequence is still under debate, it is generally accepted that the microstructure of the Al-Cu-Mg alloys in the T351 state consists of the GP or Guinier-Preston-Bagaryatskii (GPB) zones.[198]

Genevois et al. 198 indicated that in the NZ of FSW 2024Al alloy, the high temperature results in a smaller fraction of coarse S' (S) and a high level of available solutes. Consequently, the GPB zones could nucleate after welding, leading to a higher hardness.[198] In addition, the hardness profile greatly depends on the precipitate distribution and only slightly on the grain and dislocation structures.[198]. Jones et al.[196] reported that an inner HAZ hardness minimum was a result of an overaged S phase, whereas an outer minimum was believed to be due to the dissolution of precipitates in a FSW 2024Al-T351 alloy joint.

Litynska et al.[426] reported that in a FSW Al-6Cu-0.75Mg-0.65Ag (wt.%) alloy, the primary strengthening phase previously existent in the BM was dissolved in the NZ, while those in the HAZ coarsened considerably, causing softening inside the HAZ. Precipitates of the Ω (Al_2Cu) phase grew up to 200–300 nm in the HAZ, but their density decreased, which co-existed with θ'' (Al_2Cu), S' (Al_2CuMg), θ (Al_2Cu), and σ ($Al_5Cu_6Mg_2$) phases.[426]

Recently, Zhang et al.[56] conducted a detailed investigation on the microstructural evolution of FSW 2024Al-T351 joints during welding and subsequent natural aging. Similar to Jones et al.'s report,[196] two low-hardness zones (LHZs) were identified in the HAZ on both AS and RS. The LHZs near and far from the NZ were defined as LHZ I and LHZ II, respectively. It was found that LHZ I experienced an overaging process with the dissolution of GPB zones and solute clusters, as well as the formation and coarsening of S phases, whereas the dissolution of the GPB zones and the decomposition of solute clusters occurred in LHZ II (Figure 33).[56] During the long-term post-weld natural aging, no formation of the GPB zones were detected in both LHZ I and LHZ II, however, the number densities of Cu-Mg, Cu, and Mg clusters increased in LHZ II, as verified by atom probe tomographic (APT) analyses S (Figure 34), resulting in a slow recovery of hardness.[56]

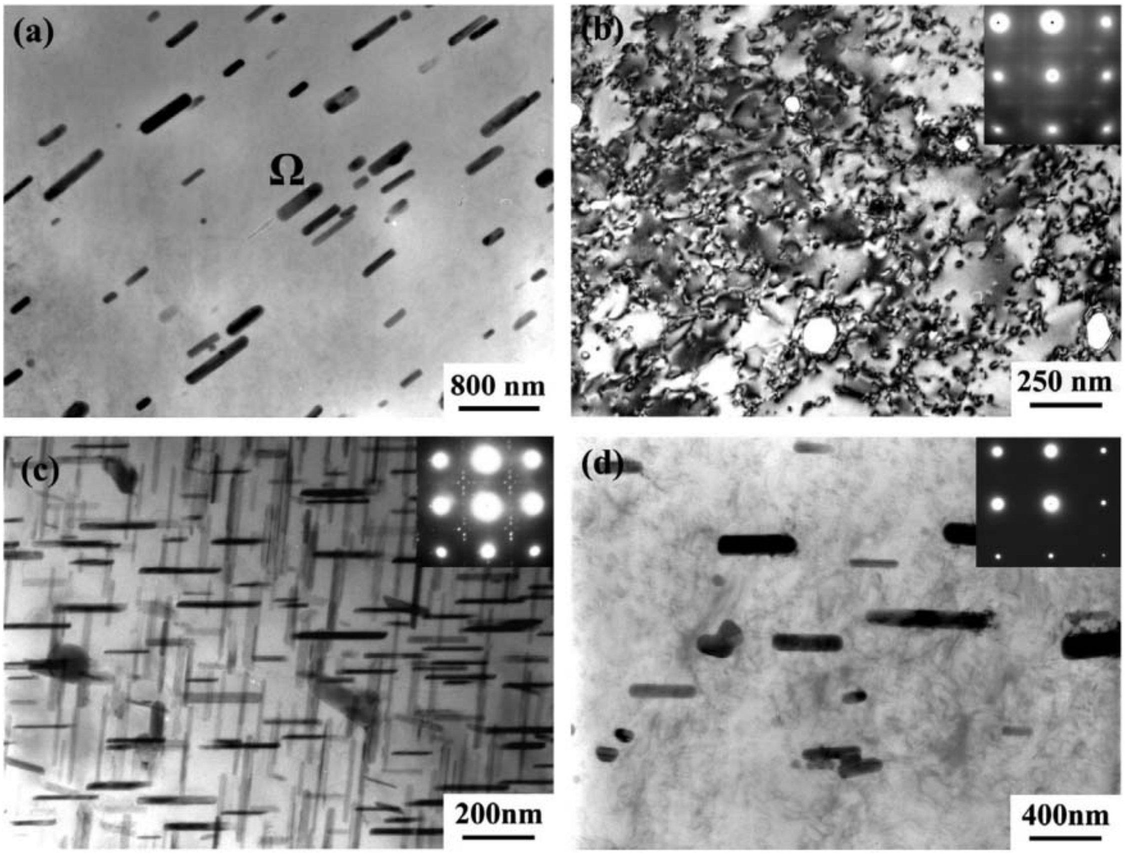

Figure 33. Bright-field TEM micrographs and associated diffraction patterns of FSW 2024Al-T351 alloy joint (800 rpm-100 mm/min) with a [100] zone axis: (a) and (b) BM, (c) LHZ I, and (d) LHZ II. (© Elsevier. Reprinted with permission from Zhang et al.[56] Permission to reuse must be obtained from the rightsholder.)

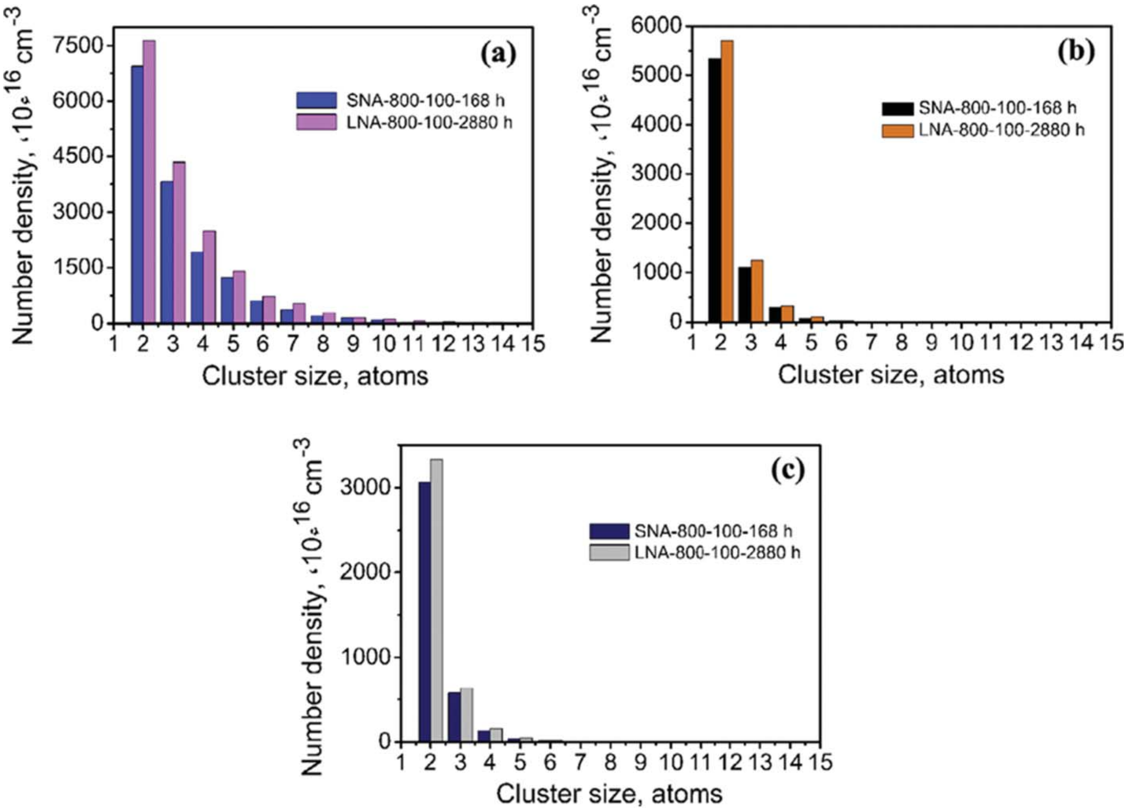

Figure 34. Effect of aging time on number densities of clusters of samples FSW 2024Al-T351 alloy joint (800 rpm-100 mm/min): (a) Cu-Mg clusters, (b) Cu clusters, and (c) Mg clusters. (© Elsevier. Reprinted with permission from Zhang et al.[56] Permission to reuse must be obtained from the rightsholder.)

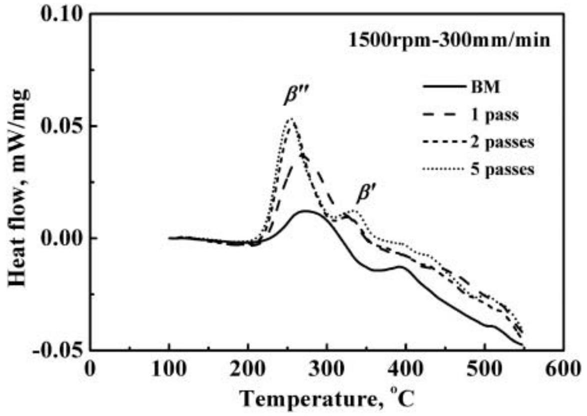

Figure 35. DSC curves of as-cast and multiple-pass FSP A356 samples at a rotational rate of 1500 rpm and a travel speed of 300 mm/min. (© Springer. Reprinted with permission from Cui et al.[438] Permission to reuse must be obtained from the rightsholder.)

The third-generation Al-Li alloys are highly promising aerospace materials due to their low density, high specific strength, excellent corrosion resistance and super plasticity.[427–429] The typical strengthening precipitates of third-generation Al-Li alloys are Al$_2$CuLi (T1), Al$_2$Cu (θ'), Al$_3$Zr (β'), Al$_3$Li (δ'), and Al$_2$CuMg (S') phases.[428,430,431] Sidhar and Mishra[431] reported the aging kinetics of FSW 2195 and 2199 Al-Li alloys. The results indicated that Ag containing alloy 2195 showed faster aging response compared to Ag-free alloy 2199.[431] Liu et al.[432] found that with increasing the rotational rate, material in the TMAZ on the RS was extended increasingly to the NZ for FSW 2060-T8 Al-Li alloy.

3.3.3. *4xxx-series aluminum alloys*

Al-Si cast alloys exhibit high wear resistance, strength, thermal conductivity, and low thermal expansion coefficient, and good casting characteristics.[433] Magnesium and copper are usually the main alloying elements of the Al-Si alloy. It is well accepted that two precipitation sequences are mainly responsible for the precipitation hardening of Al-Si-Mg and Al-Si-Cu alloys, respectively, i.e., $SSS \rightarrow GP\ zone \rightarrow \beta'' \rightarrow \beta' \rightarrow \beta$ phase (Mg$_2$Si) and $SSS \rightarrow GP\ zone \rightarrow \theta'' \rightarrow \theta' \rightarrow \theta$ phase (Al$_2$Cu). Al$_2$Cu and Mg$_2$Si are the principal strengtheners in the peak aged condition.[434] Besides these two phases, some other precipitate phases co-exist in aged Al-Si-Cu-Mg alloys, i.e., W (Al$_x$Cu$_4$Mg$_5$Si$_4$) and S (Al$_2$CuMg) phases.[435]

The as-cast structure of Al-Si-Mg-(Cu) alloys is characterized by the presence of porosity, coarse acicular Si particles, and coarse primary aluminum dendrites.[6] FSP resulted in the significant breakup of coarse acicular Si particles and coarse primary aluminum dendrites, the closure of casting pores, and the uniform distribution of broken Si particles in the aluminum matrix.[436,437] In addition, most of the Mg$_2$Si precipitates dissolved during the short period of the FSP cycle, which was attributed to significantly accelerated diffusion rates and shortened diffusion distances of the solutes resulting from intense plastic deformation and material mixing.[6,24,436]

Cui et al.[438] investigated the effect of multi-pass FSP on the Mg$_2$Si precipitates of as-cast A356 at a rotation rate of 3,000 rpm and a travel speed of 300 mm/min. It was reported that two precipitation peaks corresponding to β''-Mg$_2$Si phase and β'-Mg$_2$Si phase, respectively, were identified in the DSC curves of the as-cast and multi-pass FSP A356 samples (Figure 35).[438] It is noted that the β'-Mg$_2$Si peak in the 5-pass FSP sample was slightly higher than that in the 2-pass FSP sample, but far higher than that in the single-pass sample, and all of these peaks were apparently higher than that in the BM. This indicates that the amount of dissolved Mg atoms during FSP increased as the FSP passes increased. This has been attributed to that FSP resulted in an increase in the strength of the BM, the process temperature of subsequent FSP passes would increase due to a higher deformation resistance, which led to an increase in the amount of dissolved Mg atoms.[438]

3.3.4. *6xxx-series aluminum alloys*

In 6xxx-series aluminum alloys, magnesium and silicon as the major alloying elements, render precipitation strengthening.[212,439] Alloying elements such as silicon, manganese, iron, *etc.*, could have a significant influence on the formation of intermetallic phase.[440–442] Various coarse intermetallic particles (typically 1 pct) with sizes ranging from $-10\ \mu$m depending on the alloy chemical composition, were identified as Al$_7$Cu$_2$Fe, Al$_5$FeSi, Al$_{12}$(Fe,Cr,Mn)$_3$Si, or stable β (Mg$_2$Si) phase in 6xxx-series alloys.[443–446] Typically, chromium, manganese and zinc were added to aluminum alloys to control recrystallization and grain structure.[447] The presence of grain-refining element chromium resulted in the precipitation of Al$_{12}$Mg$_2$Cr dispersoids.[443,448]

It was generally recognized that the precipitation sequence of the Al-Mg-Si alloys was as follows:[439,449] SSS → atomic clusters[450] → initial β''[450,451] → (pre-β'' [450,452]/needle-shaped β'' precipitate[453–455]) → (rod-shaped precipitates β'/-lath-shaped B' precipitates[456,457]/U1, U2[458]) → (β-Mg$_2$Si,[457,459]/Si[458]).

As an example, Figure 36a shows a scanning transmission electron microscopy (STEM) image of a high density of fine needle-shaped precipitates and the coarse dispersoids in a 6061Al-T651 as indicated by a white arrow, which consisted of aluminum, chromium, manganese, iron, and silicon as revealed by the energy dispersive X-ray spectroscopy (EDS) spectrum inserted at the upper-right corner on the

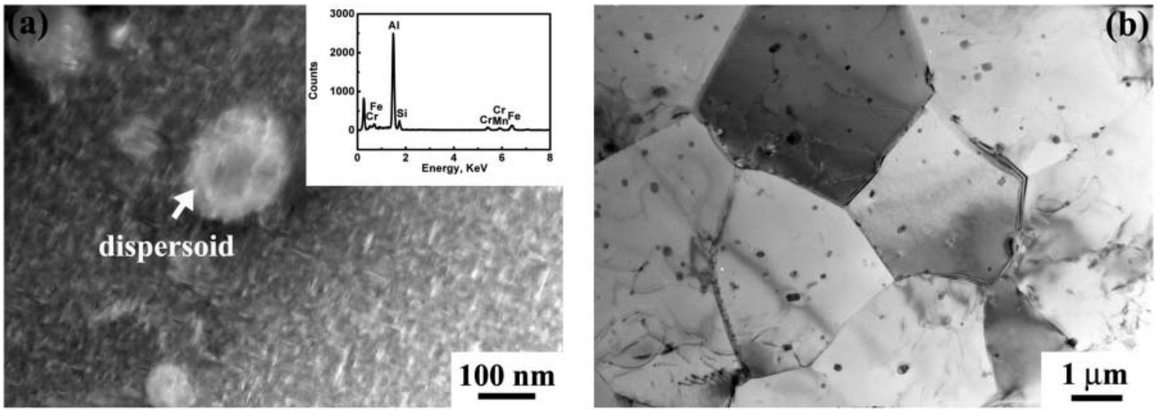

Figure 36. Microstructure of FSW 6061Al-T651 alloy: (a) STEM image showing coarse dispersoids and uniformly distributed tiny precipitates in BM (insert showing EDS spectrum of coarse dispersoid as indicated by a white arrow) and (b) TEM image showing fine and equiaxed grains in NZ. (© Springer. Reprinted with permission from Feng et al.[212] Permission to reuse must be obtained from the rightsholder.)

image.[212] After FSW, the NZ of the FSW 6061Al-T651 alloy was characterized by fine and equiaxed recrystallized grain structure and the fine needle-shaped precipitates were completely dissolved into the aluminum matrix. However, the coarse dispersoids were still seen in the NZ due to high thermal stabilization stemming from high melting point of the dispersoids (Figure 36b).[212]

3.3.5. 7xxx-series aluminum alloys

The 7xxx-series aluminum alloys are precipitation-hardened Al-Zn-Mg-(Cu) alloys. Zinc and magnesium are the main alloying elements. The undesirable iron and silicon impurities are present in the form of coarse constituent particles, i.e., Al_7Cu_2Fe, Al_2CuMg, and Mg_2Si.[51,460,461] Zirconium or chromium is added to retard recrystallization and control the grain size.[42] The usual precipitation sequence of the 7xxx-series aluminum alloys can be summarized as: SSS → GP zone → metastable η' (Mg(Zn,Al,Cu)$_2$) → stable η ($MgZn_2$).[462]

After FSW, the NZ was characterized by a fine and equiaxed recrystallized grain structure.[51,463] No fine precipitates were observed via transmission electron microscopy (TEM) examinations (Figure 37).[51] This indicates that FSW resulted in the dissolution of fine η' phase. Similar results have also been observed by Mahoney et al.[32] Dumont et al.[464] reported that although complete dissolution occurred in the NZ, it recovered some hardness upon cooling and subsequent natural aging. During this period, GP zones nucleated and grew in regions in which supersaturation was sufficient.[464]

However, Rhodes et al.[31] reported a high density of randomly oriented intragranular precipitates of $Mg_{32}(Al,Zn)_{49}$ with sizes of 60–80 nm that reprecipitated during the FSW process. Charit et al.[28] reported that there were two main types of particles in FSW 7475Al alloy, i.e., plate-shaped $MgZn_2$ precipitates and the chromium-rich spherical $Mg_3Cr_2Al_{18}$ dispersoids that remained almost unchanged. The transients and gradients in the strain, strain rate, and temperature were inherent in the thermomechanical cycles of FSW.[13] Therefore, the distribution, size, and types of precipitates were characterized as sharp spatial gradients in the transition from the BM to the center of the NZ.

3.4. Characteristic microstructures

In the FSW joints, characteristic microstructures, including onion-ring structure, segregation band, zigzag line, and kissing bond, are formed in the NZ, which are attributed to the unique and complex deformation mode in FSW/FSP. These characteristic microstructures usually exert significant influences on the mechanical properties and fracture behavior of the FSW joints of aluminum alloys and therefore attract significant research efforts.

3.4.1. Onion-ring structure

On the transverse cross-section of the NZ, periodic flow pattern consisting of concentric “onion rings”, named as onion-ring structure, were often observed.[188,465,466] Recently, 3D material flow in thick dissimilar Airware^{TM} 2050 fiction-stir butt welds and the coexistence of onion rings and serrated interface were reported in Fenoel et al.[188] These rings are also evident in other cross-section orientations through the NZ.[467] The NZ can be sectioned along three orientations, i.e., transverse section (XOZ), longitudinal section (YOZ), and horizontal section (XOY) (Figure 38).[466] These onion rings represent a typical feature of the NZ in the FSW/FSP materials. The formation of the onion rings has been explained by the geometrical effect[466,467] the periodic variations in grain sizes,[468] particle-rich bands,[152,242,392,469,470] grain orientation,[471] and texture variations.[49,471]

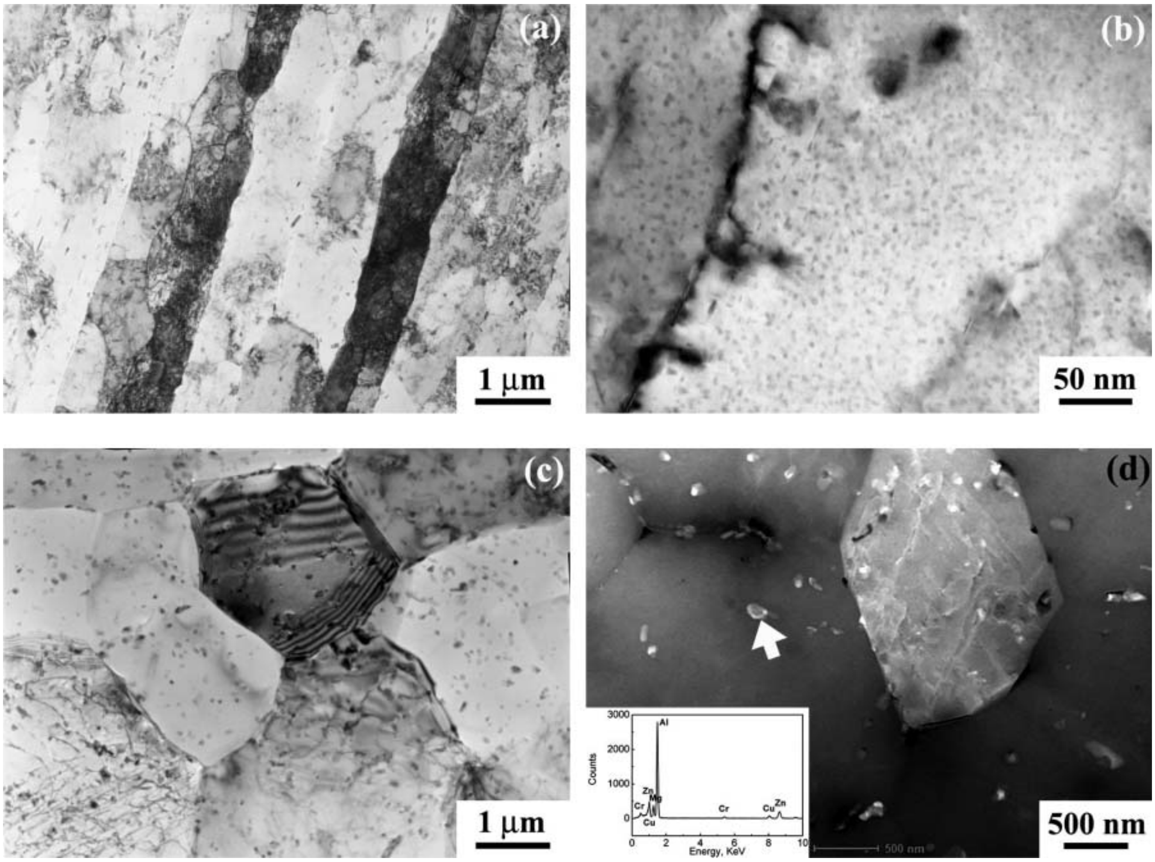
(a)
1 μm
(b)
50 nm
(c)
1 μm
(d)
500 nm
Counts
Energy, KeV
Al
Zn
Mg
Cr
Cu
Cr
Cu
Zn
500 nm

Figure 37. TEM images of FSW 7075Al-T651 alloys showing (a) subgrain structure and (b) tiny and uniformly distributed precipitates in BM; (c) grain structure and (d) second-phase particle with EDS spectrum in NZ. (© Springer. Reprinted with permission from Feng et al.[51] Permission to reuse must be obtained from the rightsholder.)

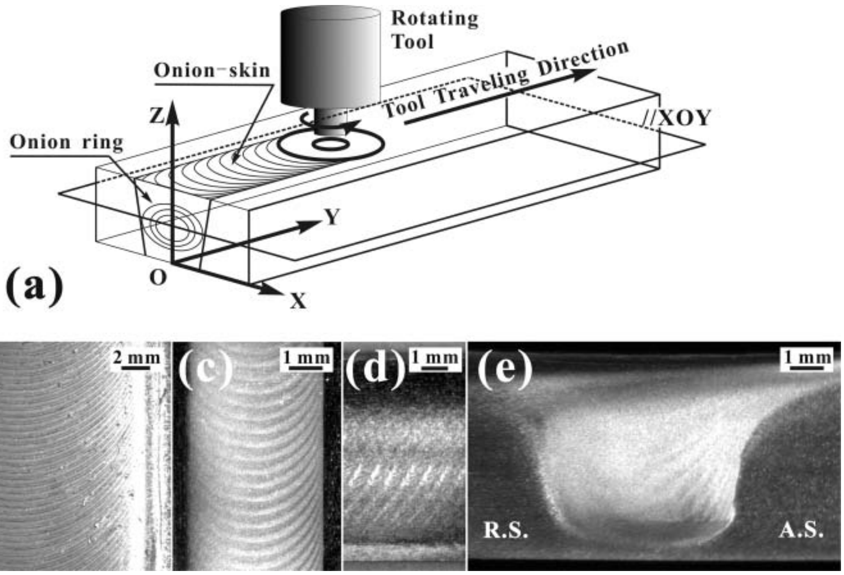
Rotating Tool
Onion-skin
Tool Traveling Direction
//XOY
Onion ring
Z
Y
O
X
(a)
(b)
2 mm
(c)
1 mm
(d)
1 mm
(e)
1 mm
R.S.
A.S.

Figure 38. (a) schematic illustration of FSP and macroscopic images of SZ in FSP 5083Al alloy, (b) onion skin on top surface of FSP sample, (c) onion rings in plane XOY, (d) onion rings in longitudinal section (YOZ), and (e) onion rings in transverse section (XOZ). (© Elsevier. Reprinted with permission from Cui et al.[466] Permission to reuse must be obtained from the rightsholder.)

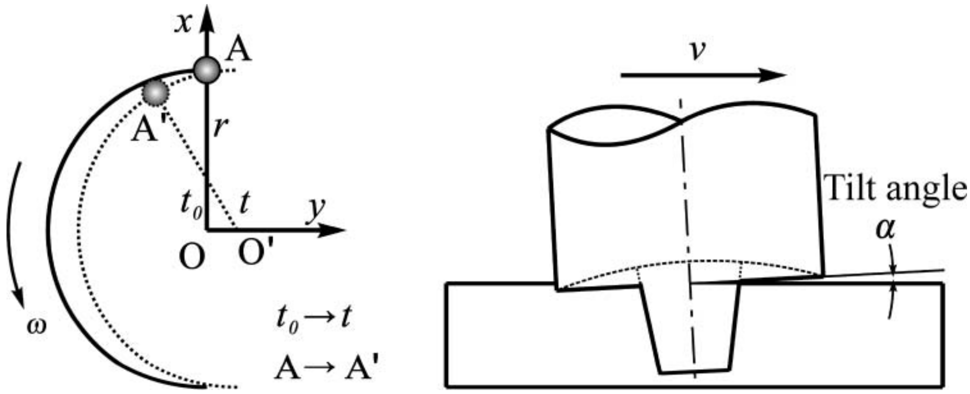

Figure 39. Schematic drawing for deriving Eq. (14) (© Elsevier. Reprinted with permission from Cui et al.[466] Permission to reuse must be obtained from the rightsholder.)

Based on the flow characteristics of material during FSW/FSP, Cui et al.[466] proposed a set of equations to describe the horizontal onion ring patterns in the form of

$$x = r\cos\omega t_m$$

$$y = (vt_m - r\sin\omega t_m)\cos\alpha \quad \left(t_m = t + 2(n-1)\pi/\omega,\ 0 \le t \le \pi/\omega,\ n = 1, 2, 3\ldots\right), \tag{14}$$

where x and y are the coordinates of the pattern, r is the radius of the tool shoulder (for onion-skin) or the radius of the onion ring, v is the welding speed (mm/min) of the tool, ω is the rotational rate (rpm) of the tool, α is the tilt angle of the tool, and t_m is the time for formation of the onion skin/ring.

As shown schematically in Figure 39,[466] trace point A will move to trace point A' as the time increases from t_0 to t. The pattern in the NZ is actually a three-dimentional configuration. Therefore, the observed pattern is the projection of the 3D configuration on the plane parallel to XOY (Figure 38a).[466] Since the tilt angle α is in the YOZ plane, the coordinate of the pattern along the Y direction should be modified by $\cos\alpha$ as shown in Eq. (9).

Two main factors that may cause such a periodic oscillation in the deformation are threads on the rotating tool and the eccentricity of the tool.[472] Figure 40b reveals that the bands observed in Figure 40a correlate to a periodic variation in the average grain orientation aligned with the plate normal direction.[472] The grain orientations vary between

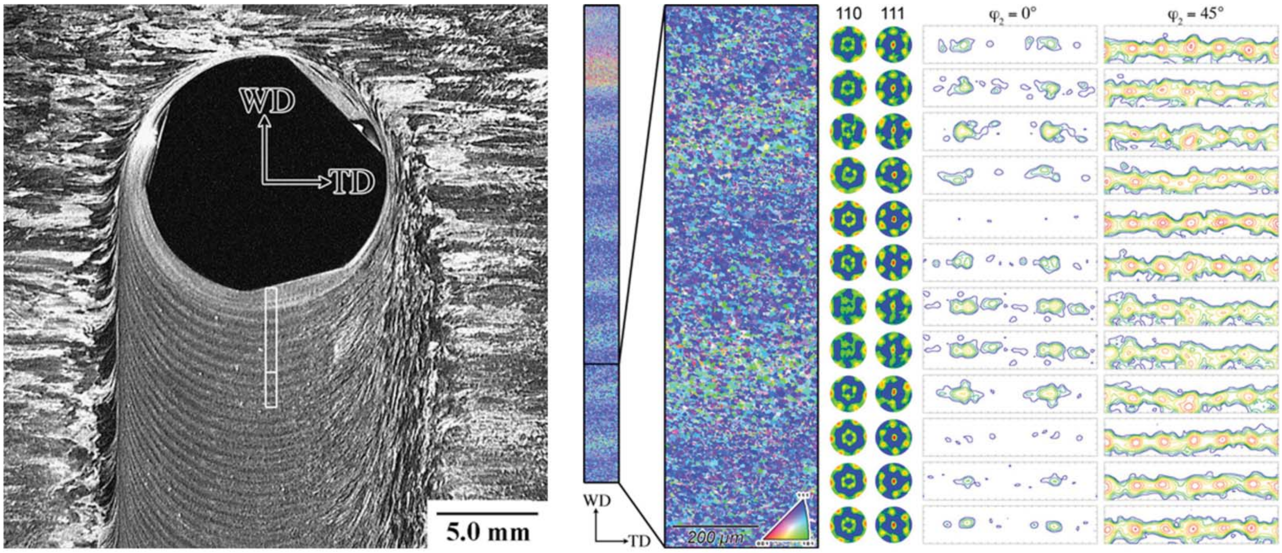

(a)

(b)

Figure 40. (a) optical macrograph of plane at 10.4 mm below top surface sectioned from FSW 2195Al alloy, (b) EBSD map of grain orientations along viewing direction from indicated regions in (a), and texture information (110 and 111 pole figures in stereographic projection and and $\varphi_2 = 0°$ and $\varphi_2 = 45°$ orientation distribution function (ODF) sections) from 100 μm regions along vertical welding direction. (© Elsevier. Reprinted with permission from Fonda & Bingert.[472] Permission to reuse must be obtained from the rightsholder.)

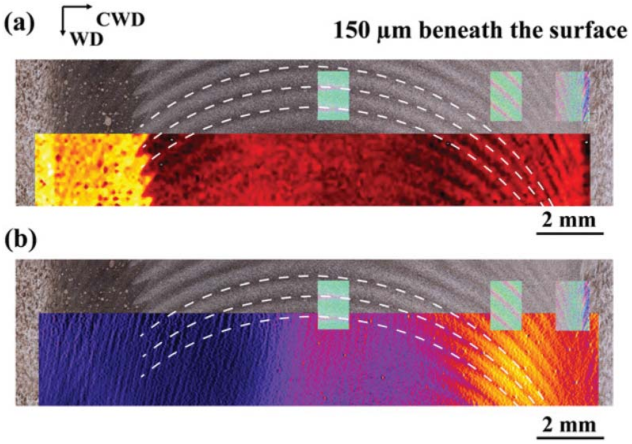

Figure 41. Correlation between banded macrostructure, local mechanical properties and crystallographic texture. The <110> fiber aligned with the material flow direction (green area on the EBSD scan) correspond to HDB and LHB. (a) Emphasis on high hardness bands (HHB)/low hardness bands (LHB) pattern. (b) Emphasis on high deformation bands (HDB)/low deformation bands (LDB) pattern. (© Elsevier. Reprinted with permission from Texier et al.[473] Permission to reuse must be obtained from the rightsholder.)

a near−<111> orientation (blue) and a near−<110> orientation (green) with a periodicity measured to be approximately 570 μm.[472]

Texier et al.[473] reported that near-surface mechanical heterogeneities were observed in a dissimilar FSW joint of 2024Al-T3 and 2198Al-T3 alloys, as shown in Figure 41. The results indicated that the shoulder-affected regions exhibited heterogeneous banded macrostructures in the top region of the joint, and these bands tended to vanish few hundreds of micrometers beneath the surface.[473]

3.4.2. Linear segregation band

In addition to the onion-ring structure, linear segregation bands consisting of second phase particles were sometimes detected in the shoulder-driven zone (SDZ) of the NZ in the FSW joints of precipitation-strengthened aluminum alloys. Such linear segregation bands exhibited different distribution characteristics from the onion-ring structure, as shown by the black lines in Figure 42a.[474] Under higher magnifications, continuous linear segregation bands were clearly visible in both optical microscopy (OM) and scanning electron microscopy (SEM) images (Figure 42 and 42c).[474] Moreover, almost all the secondary phase particles in the matrix were dissolved as shown by the SEM image (Figure 42c).[474] The magnified image of the arrow zone in Figure 42c shows that secondary phase particles segregated at the grain boundaries and the linear microstructure consisted of countless secondary phase particles at the grain boundaries (Figure 42d).[474]

It is believed that the formation of the linear segregation bands resulted from the periodic material flow, with the average band spacing on the longitudinal and horizontal cross sections equal to the tool advancement per revolution and an equation $D = \nu\cdot(2\pi/\omega)\cdot\cos\alpha$ was proposed to predict the spacing D between two adjacent lines along the y direction.[474] It was suggested that the secondary phase particles formed the phase aggregation bands at the high strain rate gradient region and were then partially broken and dis-

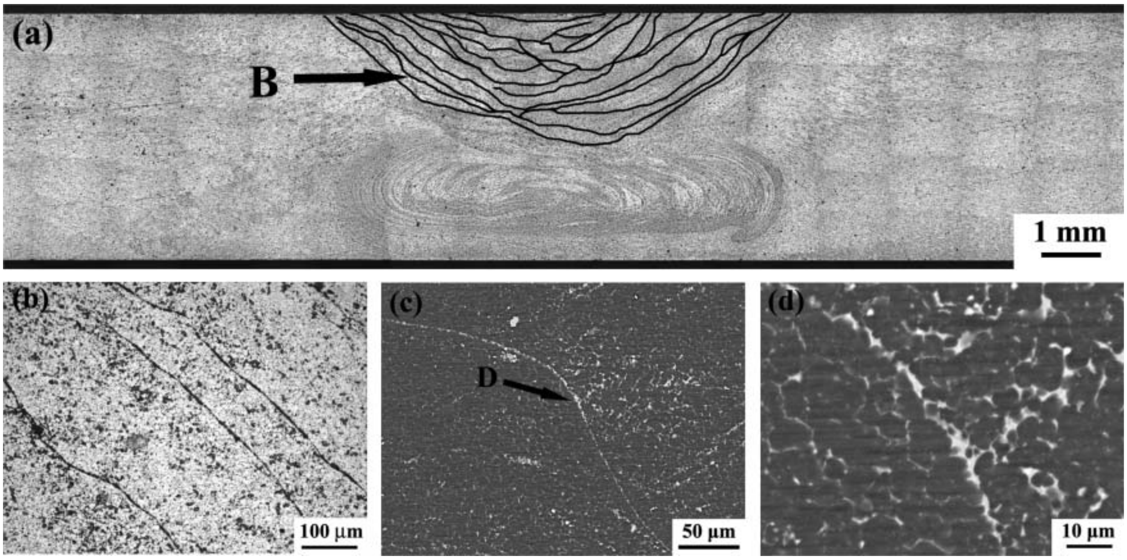

Figure 42. Segregation bands on transverse cross sections of (a) FSW 2024Al-T351 alloy joint produced at a tool rotational rate of 800 rpm and a welding speed of 200 mm/min, magnified (b) OM and (c) SEM images of position B in (a), and (d) magnified image of arrow zone in (c).[474]

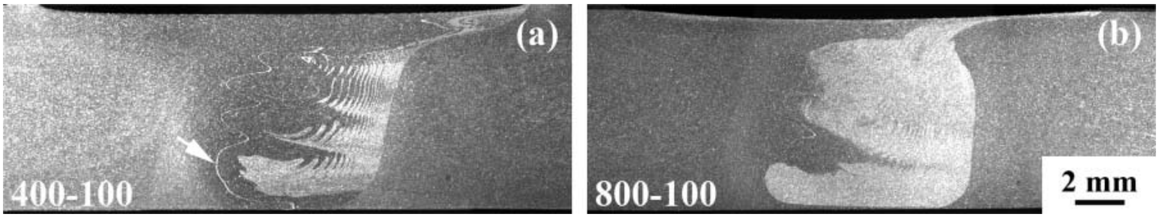

Figure 43. Cross-sectional macrographs of FSW Al-Mg-Sc alloy joints showing the zigzag line under different rotational rates at a constant welding speed of 100 min/min: (a) 400 rpm and (b) 800 rpm (AS is on the right). (© Elsevier. Reprinted with permission from Tao et al.[176] Permission to reuse must be obtained from the rightsholder.)

solved under the SPD and heat input. Meanwhile, the dissolved elements migrated to the long straight grain boundaries and re-precipitated following welding, forming the liner segregation bands.

3.4.3. Zigzag line

On the transverse section of the NZ of the FSW joints of aluminum alloys, a distorted faint line pattern, called the "zigzag line" or "lazy S", was sometimes observed.[176,475,476] The zigzag line, which runs through the whole NZ from the bottom to the top or appears only at the root of the SZ, was usually generated under lower heat-input welding condition and showed up after the weld was etched. Figure 43 shows the effect of welding heat input on the zigzag line in FSW Al-Mg-Sc alloy joints.[176] At a low heat input with a welding speed of 400 mm/min, the zigzag line was obviously visible on the transverse section of the NZ as shown by the arrow (Figure 43a), however, at a high heat input with a welding speed of 100 mm/min, the zigzag line could hardly be detected (Figure 43b).[176]

Generally, the zigzag line is believed to result from the oxide layer on the initial butt surfaces of aluminum plates.

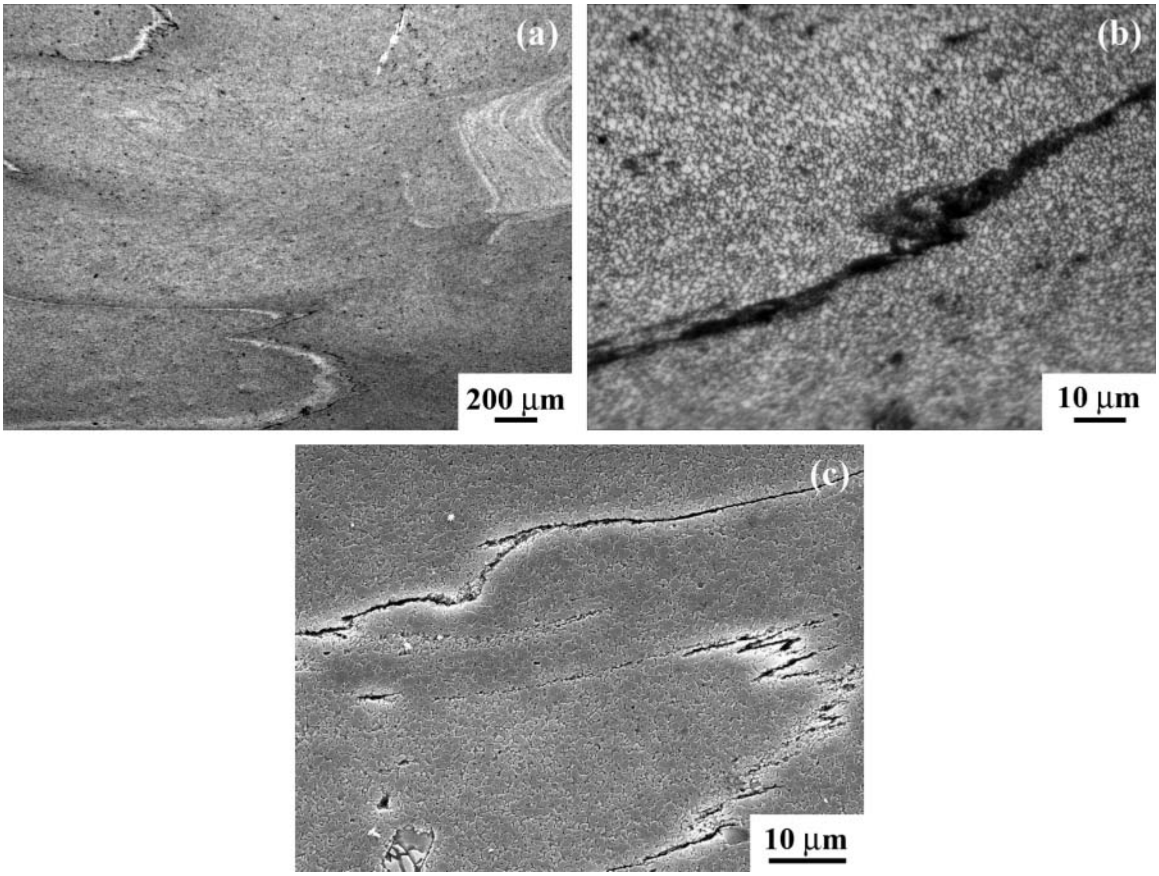

Figure 44. Microstructure of kissing bond at root tip of NZ of FSW Al-Mg-Sc alloy joint (400 rpm-400 mm/min): (a) lower and (b) higher magnification images under OM, and (c) image under SEM. (© Elsevier. Reprinted with permission from Tao et al.[176] Permission to reuse must be obtained from the rightsholder.)

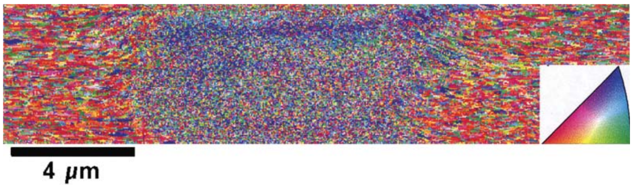

Figure 45. A representative orientation image from a complete cross section of FSW 1100Al alloy at a rotational rate of 700 rpm and a welding speed of 180 mm/min. Color key shows poles aligned with normal direction of plate.[16] (© Elsevier. Reprinted with permission from Field et al.[17] Permission to reuse must be obtained from the rightsholder.).

Sato et al.[475] observed the microstructure in the root tip of the zigzag line of FSW 5052Al alloy by focused ion beam-(FIB) assisted TEM. They suggested that the zigzag line originated from the oxide layer of the initial butt surface that was fragmented during FSW. Ren et al.[476] conducted a comparative study of FSW and FSP of 7075Al-T651, and clearly indicates that the oxide layer of the initial butt surface resulted in the occurrence of the zigzag line. Furthermore, they indicated that the zigzag line in FSW aluminum alloy butt joints could not be completely eliminated by clearing the surface oxide layer prior to welding.

3.4.4. Kissing bond

Different from the local and discontinuous oxide particle distribution along the zigzag line, the kissing bond consisting of a continuous oxide film is only observed at the root tip of the NZ,[176,477,478] as shown by Figure 44.[176] The kissing bond are prone to forming in the low heat-input conditions,[262,479] due to a lack of oxide layer disruption and insufficient material flow. Tao et al.[176] indicated that increasing the traverse speed from 100–400 mm/min gave rise to a longer kissing bond in the FSW Al-Mg-Sc alloy joints.

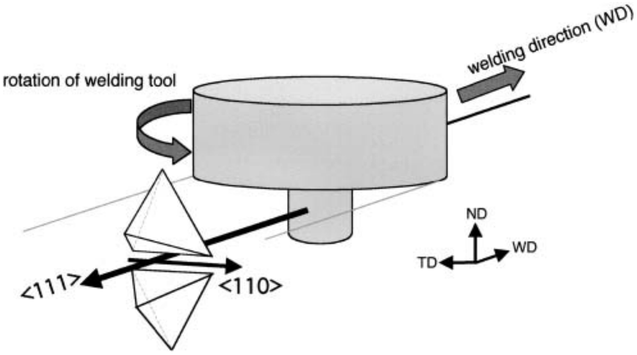
rotation of welding tool
welding direction (WD)
<111>
<110>
ND
WD
TD

Figure 46. Schematic illustration of {111} tetrahedrons formed at weld center during FSW. (© Springer. Reprinted with permission from Sato et al.[39] Permission to reuse must be obtained from the rightsholder.)

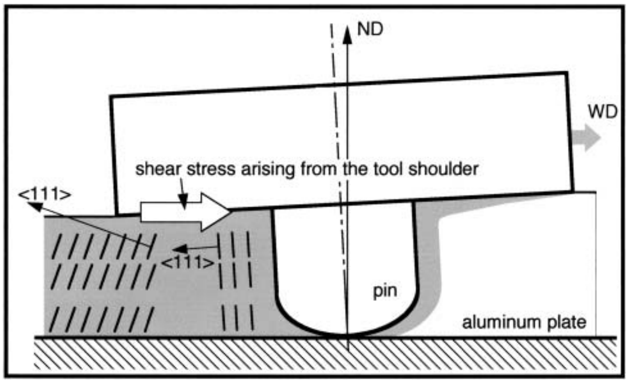
ND
WD
shear stress arising from the tool shoulder
<111>
<111>
pin
aluminum plate

Figure 47. Schematic illustration of effect of shear stress arising from tool shoulder on shear plane inclination at weld center. (© Springer. Reprinted with permission from Sato et al.[39] Permission to reuse must be obtained from the rightsholder.)

3.5. Texture

The presence of texture or preferred orientation influences a variety of properties, including strength, ductility, formability, and corrosion resistance.[4] In the past few years, extensive studies have focused on the texture analysis of the FSW/FSP aluminum alloys.[16,39,49,396,412,472,480,481] It was reported that the texture in the NZ is either weak or present

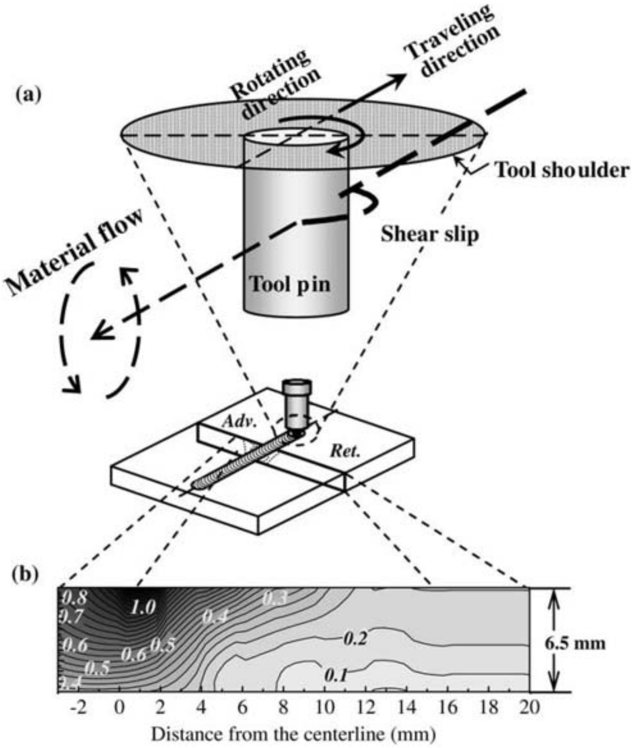
(a)
Rotating direction
Traveling direction
Tool shoulder
Shear slip
Material flow
Tool pin
Adv.
Ret.
(b)
0.8
0.7
1.0
0.3
0.4
0.6
0.6
0.5
0.2
0.5
0.4
0.1
6.5 mm
-2
0
2
4
6
8
10
12
14
16
18
20
Distance from the centerline (mm)

Figure 48. Relationship between material flow during FSP and texture variation: (a) material flow (dashed line) during FSP and (b) through-thickness contour plot of reduced intensitites of (111) along ND in Case 1 (Case 1: a regular FSP plate subjected to both SPD and frictional heating). (© Elsevier. Reprinted with permission from Woo et al.[480] Permission to reuse must be obtained from the rightsholder.)

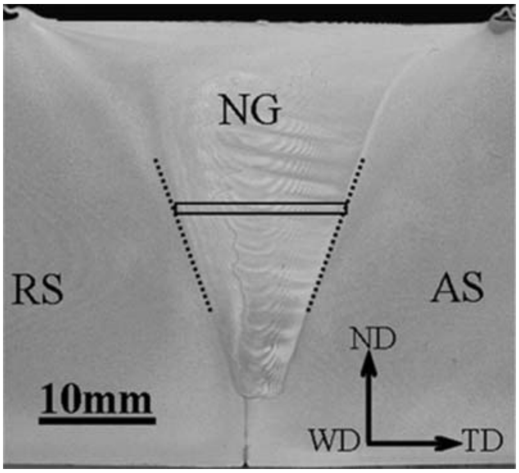

Figure 49. Optical macrograph of transverse section of FSW joint (the rectangle shows region where EBSD mapping took place. Thin dashed black lines are at ± 20° from the vertical direction. WD is out of paper). (© Elsevier. Reprinted with permission from Ahmed et al.[481] Permission to reuse must be obtained from the rightsholder.)

in a complex pattern such as the typical shear texture component induced by the rotating shear plastic flow along the pin surface.[39,73] Furthermore, strong texture gradients are not only in the transition from the BM to the NZ, but also from point to point within the NZ itself.[482] It is shown that the local textures are directly related to the welding parameters, i.e., the tool rotational rate and welding speed. The strong gradients in crystallographic texture can be observed through the NZ of the weld of 1100Al alloy (Figure 45).[16]

Sato et al.[39] noted that the Goss texture in the parent 6063Al alloy changed to a typical shear texture component with two types of orientations in the NZ. At the backside of the tool, the common {111} plane and <110> direction are roughly parallel to the pin surface and the rotating direction of the tool as schematically shown by two {111} tetrahedrons in Figure 46.[39] The forward motion of the tool shoulder produces the shear stress toward the WD (Figures 46 and 47).[39] Figure 48 shows that the shear texture is mainly caused by the severe shear deformation from the stirring action of tool during FSP.[480] Woo et al.[480] also observed that the heating alone from the tool shoulder has little effect.

The shear generated by the rotating pin is the predominant mechanism influencing the microstructure/texture, with the tool forward motion having less influence.[481] The orientation imaging microscopy (OIM) clearly shows near-vertical bands, which decrease in thickness from the center to the edge, of alternating near <110> (green) and near <111> (blue/purple) grain orientation, across the whole NZ (Figures 49 and 50).[481] The spacing between the bands is believed to be equivalent to the tool advance per revolution. Interestingly, this rotational symmetry suggests that the predominant deformation parameter should be the rotation of the pin, with the forward motion of the tool having a less significant influence on the deformation gradient experienced by the material.[481]

Xu and Deng[49] reported that the texture patterns are complex but a dominant theme is the appearance of bands. The banded pattern on the transverse cross-section is often in the form of onion rings, as described above. The spacing between the bands on the longitudinal and horizontal cross-sections equals the distance traveled by the welding

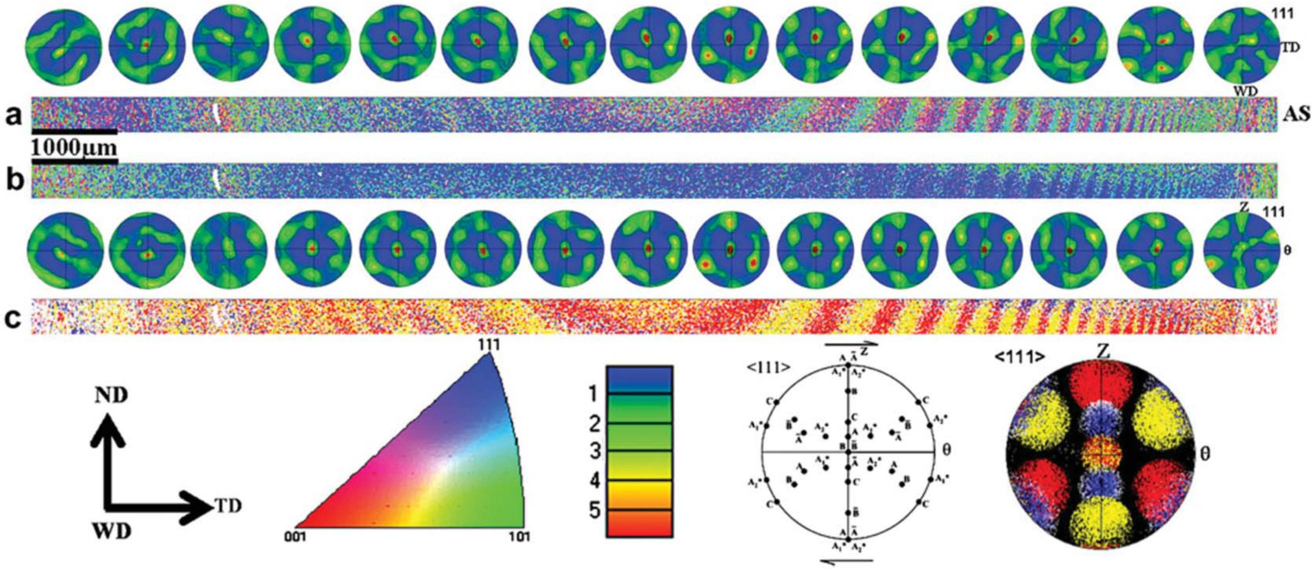

Figure 50. (a) EBSD inverse pole Figure (IPF) colouring map with respect to ND for region indicated in Figure 49, (b) IPF colouring map after rotational correction with respect to r direction, with resultant (111) pole Figures below map, (c) texture components map after rotational correction with B (red), $\overline{B}$ (yellow) and C (blue). (© Elsevier. Reprinted with permission from Ahmed et al.[481] Permission to reuse must be obtained from the rightsholder.)

tool in one revolution. The texture patterns are observed to correlate well with equivalent plastic strain contours from simulations of the corresponding FSW process.[49] The crystallographic texture that evolves during FSW contains sharp spatial gradients that undoubtedly influence the performance and structural integrity of the weld.[16] Park et al.[73,483] reported that the texture variation can strongly affect the tensile properties in a FSW AZ61 magnesium alloy.

4. Mechanical properties

FSW has many advantages over the traditional fusion welding processes, including the absence of cracking, fine microstructure, good dimensional stability, low residual distortion, and excellent mechanical properties.[4] The FSW joints are made in the solid state with a fine-grained microstructure, exhibiting superior tensile, fatigue, creep, and bend properties compared with the conventional fusion welds.[39,484–487]

4.1. Hardness

As described above, the aluminum alloys are classified into precipitation-hardened alloys and solid-solution-hardened alloys.[4] Although the precipitation-hardened aluminum alloys are readily weldable by FSW, a severely softened region in the HAZ would occur, which was basically characterized by the dissolution or coarsening of the originally existent primary strengthening precipitates during the thermal cycle.[34] Frictional heating during welding has the most significant impact on the hardness profiles in the welds of precipitation-hardened aluminum alloys, because the volume fraction, size, and distribution of the strengthening precipitates are remarkably influenced by thermal hysteresis.[39] The hardness profiles depend greatly on the precipitate distribution and only slightly on the grain size.[34,39]

Figure 51 shows typical microhardness contour maps of the FSW 7075Al-T651 alloy joints made with different FSW parameters.[51] The slight asysmmetry of the weld was noticeable between the AS and RS.[51] Two LHZs, located in the HAZs adjacent to the border between the TMAZ and HAZ, were obviously observed. The existence of LHZs was mainly attributed to the dissolution or coarsening of precipitates,[175] or related to crystallographic texture,[38,488] and grain/subgrain structure.[488] As the welding speed increased from 100 to 400 mm/min at a constant rotational rate of 800 rpm, the width of the LHZs decreased and the hardness values increased; furthermore, the location of the LHZs moved inward. As the rotational rate increased from 800 to 1200 rpm at a constant welding speed of 400 mm/min, the width and hardness values of the LHZs had almost no change, but the location of the LHZs moved outward. Similar results have also been observed in a FSW 6061Al-T651 alloy.[212]

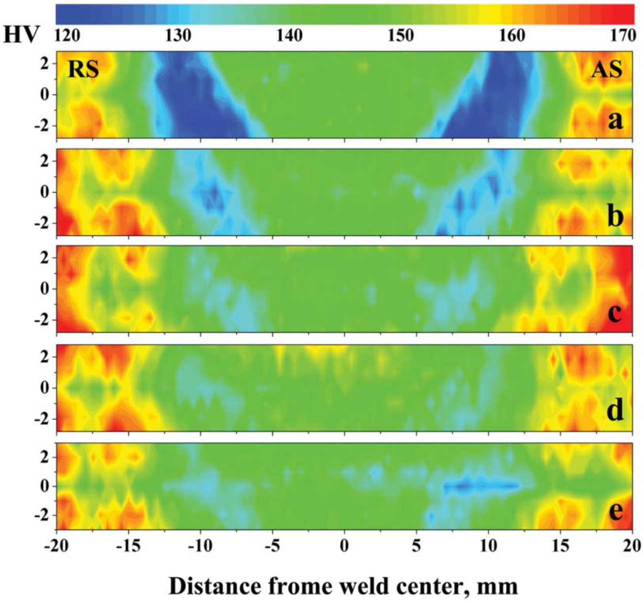

Figure 51. Microhardness contour maps for FSW 7075Al-T651 alloy joints: (a) 800 rpm and 100 mm/min, (b) 800 rpm and 200 mm/min, (c) 800 rpm and 400 mm/min, (d) 1000 rpm and 400 mm/min, (e) 1200 rpm and 400 mm/min. (© Springer. Reprinted with permission from Feng et al.[51] Permission to reuse must be obtained from the rightsholder.)

Liu and Ma proposed[175] a heat source zone (HSZ)isothermal dissolution layer (ITDL) model to explain the change of the LHZs with the welding speed and rotational rate. As shown in Figure 52,[175] a zone approximately corresponding to the NZ is regarded as the HSZ. During FSW, as the HSZ moved along the joint line, the thermal exposure exerted to peripheral material resulted in the generation of the LHZs that experienced a thermal cycle with the same peak temperature corresponding to the temperature range for the dissolution or coarsening of the strengthening precipitates. In this case, the LHZs are defined as the ITDLs. Increasing the welding speed reduced the dissolution time of the precipitates due to increased heating and cooling rates. Therefore, the width of the LHZs decreased, the hardness values increased, and the location of the LHZs moved inward. On the other hand, increasing the tool rotational rate exerts no noticeable effect on the heating and cooling rates and the dissolution time, resulting in almost unchanged width and hardness values of the LHZs, but the location of the LHZs moved outward.

For 5-mm thick FSW 2024Al-T351 alloy joints, two LHAZs were observed on both AS and RS sides, with LHZ I having a lower hardness than LHZ II (Figure 53).[56] The hardness of LHZ I increased with increasing welding speed from 100 to 400 mm/min, but was independent of the rotational rate ranging from 400–1200 rpm. The hardness of LHZ II was independent of both the welding speed and rotational rate, ALthough the location of LHZ II moved inward with increasing the welding speed (Figure 53a and 53b).[56] It is important to note that the significant recovery of hardness occurred in both the LHZs after post-welding natural aging. For LHZ I, the hardness would slightly recover during a short-term post-weld natural aging of 24–168 h and then had a stable hardness during a long-term natural aging from 168–8760 h, whereas in LHZ II, a slow recovery of hardness occurred throughout the whole aging process (Figure 53c and 53d), due to the increase in the number densities of Cu-Mg, Cu and Mg clusters, as shown in Figure 34.[56]

For the solid-solution-hardened aluminum alloys, generally FSW does not result in a softened HAZ.[4,40,412] In the absence of appreciable work hardening, the hardness (H_v) of the material is proportional to the yield stress through the expression:[489]

$$H_v \approx 3\sigma_y \tag{15}$$

Equation (15) could therefore be reformulated in terms of hardness through the following Hall-Petch type relationship:

$$H_v = H_0 + k_H d^{-1/2}, \tag{16}$$

where H_0 and k_H are constants associated with the hardness measurements.

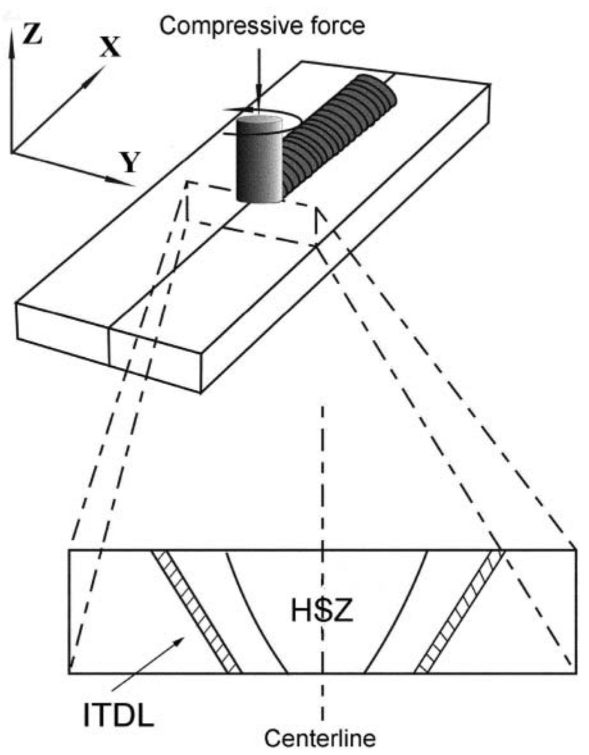

Figure 52. Schematic of HSZ-ITDL model. (© Springer. Reprinted with permission from Liu & Ma.[175] Permission to reuse must be obtained from the rightsholder.)

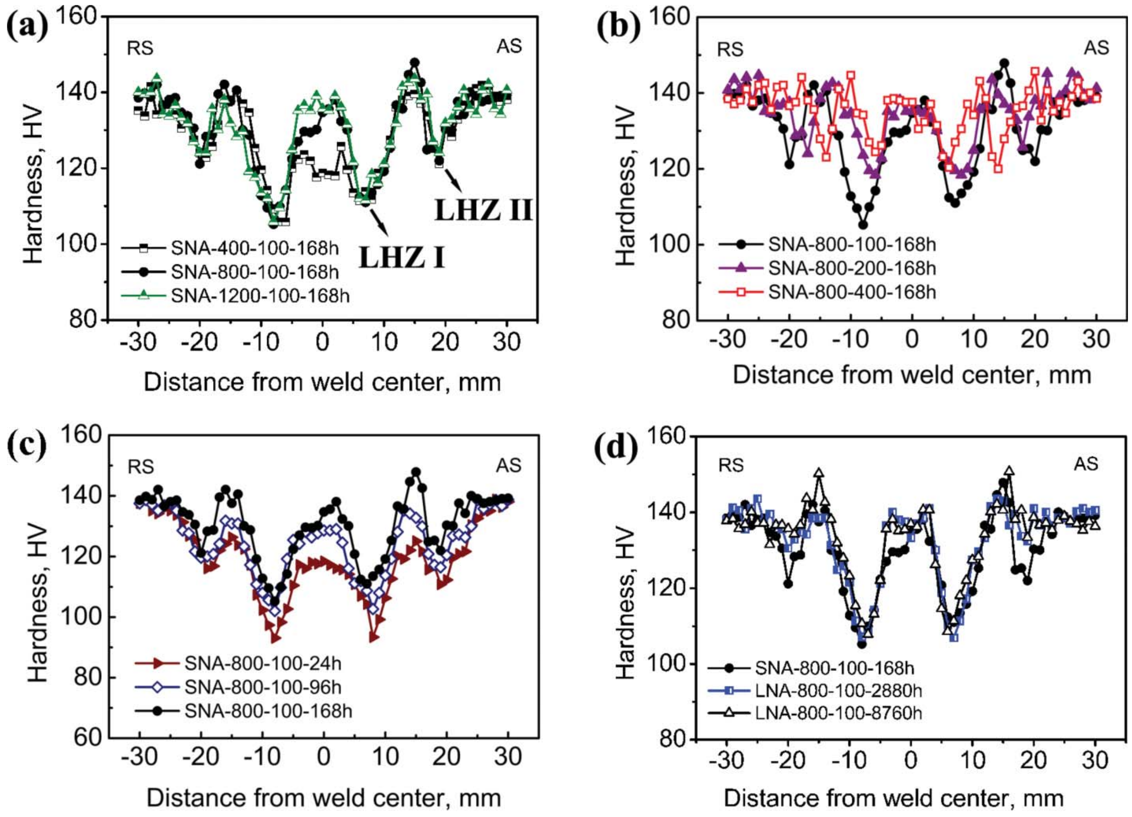

Figure 53. Hardness profiles of FSW 2024Al-T351 alloy joints showing effect of (a) rotational rate, (b) welding speed, (c) short-term natural aging time, and (d) long-term natural aging time. (© Elsevier. Reprinted with permission from Zhang et al.[56] Permission to reuse must be obtained from the rightsholder.)

Table 2. Summary of k_y and k_H in different materials ($Hv \approx 3\sigma_y$).[492–496]

Materials	Conditions	k_y, MPa $\mu m^{1/2}$	k_H, HV $\mu m^{1/2}$	Refs.
Pure Al	Annealing with grain sizes of 30–500 μm.	30	9	492 493
Pure Al	ECAP	115 (YS)	38.3	496
Al-1Mg (wt. %)	ECAP	131 (YS)	43.7	496
Al-3Mg (wt. %)	ECAP	148 (YS)	49.3	496
Al-0.12Zr (wt. %)	ECAP	112 (YS)	37.3	496
5083 (H112)	FSP	99.6 (UTS) 249.5 (YS)	36.6	494
1050	FSW		19	495

Hardness is a measure of the resistance of a material to localized plastic deformation under the application of indenting load.[490] In practice, however, care must be taken in making use of Eq. (16). Furukawa et al.[491] reported that microhardness data of an Al-5.5%Mg-2.2%Li-0.12%Zr alloy followed the above Hall-Petch type relationship with annealing at temperatures above ~400°C, but it broke down at smaller grain sizes because of variations in the volume fraction of the precipitates.

Table 2 summarizes the k_y and k_H of different aluminum alloys.[15,492–495] Besides the dislocation density in the grain interiors, other microstructural factors, such as solute elements and particle distribution, can also influence the slope of the Hall-Petch type equation in aluminum alloys.[495] Hasegawa et al.[496] reported that the magnesium addition to aluminum leads to a larger k_y because magnesium atoms suppress the dislocation movement. The hardness was observed to be essentially related to the grain size through the Hall-Petch relationship in the NZ of a FSW 1050Al alloy (Table 2).[495] A similar Hall-Petch type relationship was also reported in the NZ of a FSW AZ31B-H24 magnesium alloy.[83,497]

Sato et al.[495] reported that the slope k_H (19 HV $\mu m^{1/2}$) obtained from the NZ lies between the k_H obtained from the annealed aluminum and the k_H obtained from the UFG aluminum produced by the special intense straining processes, because the DRX during FSW left some grains with a high density of dislocations. This result suggests that the dislocation density of the NZ is higher than that of annealed materials but lower than that of UFG materials.[495] However, Sato et al.[495] reported that the relationship between hardness and grain size in the NZ of FSW 5083Al alloy was expressed by the Hall-Petch equation with a change in slope. This was attributed to the homogeneous distribution of many fine particles.[495] Sato et al.[40] concluded that the hardness profile could not be explained by the Hall-Petch relationship, but rather by Orowan hardening, namely, the hardness profile in the FSW 5083Al alloy was predominantly governed by the dispersion strengthening. The Orowan hardening is expressed by the following equation:[415]

$$\tau_y = \mu b \, / \, L, \tag{17}$$

where τ_y is the critical resolved shear stress, μ is the shear modulus, b is the Burgers vector, and L is the average distance between particles.

4.2. Tensile properties

4.2.1. Effect of welding parameters and tool geometry

It has been well documented that welding parameters and tool geometry play a significant role in the material flow pattern and temperature field distribution, thereby influencing the mechanical properties of the FSW aluminum alloy joints.[498–502] It was widely reported that the fracture of the FSW joints of the precipitation-strengthened aluminum alloys normally occurred in the HAZs, usually corresponding well to the LHZs.[50,175] Figure 54[175] shows that in all the FSW 6061Al-T651 joints prepared with varied welding

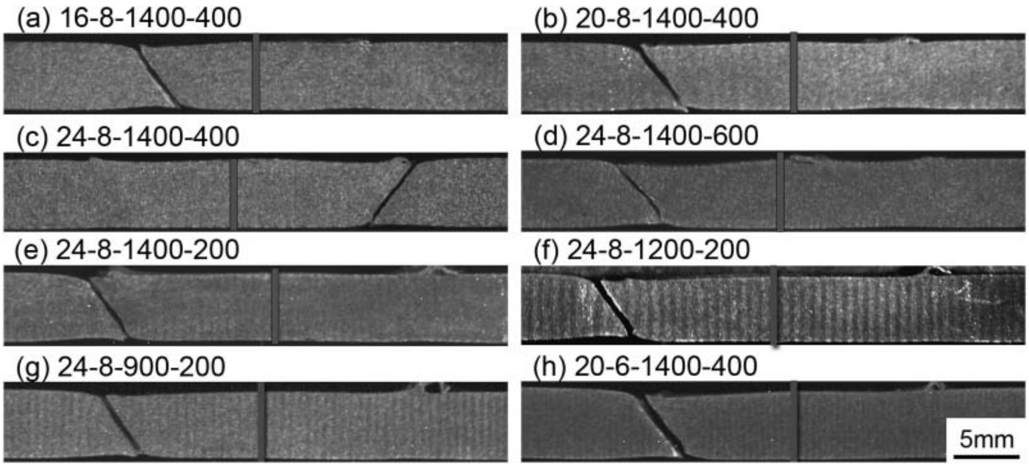

Figure 54. Failed FSW 6061Al-T651 alloy joints showing the corresponding between fracture locations and LHZs. (© Springer. Reprinted with permission from Liu & Ma.[175] Permission to reuse must be obtained from the rightsholder.)

parameters and tool dimensions, the fracture occurred exactly along the LHZs. This indicates that the properties of the FSW joints of the precipitation-strengthened aluminum alloys are mainly controlled by the strength (or hardness) of the LHZs.

Table 3 summarizes the welding parameters versus the tensile properties of FSW joints of several typical precipitation-strengthened aluminum alloys.[56,175,213] Generally, the strength of the FSW joints increased with increasing welding speed and was almost independent of the rotational rate. Furthermore, Liu and Ma[175] indicated that the tensile strength of the FSW 6061Al-T651 alloy joints exhibited no noticeable dependence on the dimension of the shoulder and pin. Such a variation tread of the joint strength with the welding parameters and tool dimension can be satisfactorily explained by the HSZ-ITSL model proposed by Liu and Ma.[175] Increasing the welding speed results in an increase in the hardness of the LHZs due to the shortened dissolution time of precipitates, thereby increasing the strength of the FSW joints of aluminum alloys. In contrast, the change in the rotational rate and tool dimension only moves the location of the LHZs, but does not change the hardness of the LHZs due to unchanged dissolution time of precipitates, therefore the joint strength does not change.

Conventional polycrystalline metals show an increase in yield strength with decreasing grain size according to the well-known Hall-Petch relationship,[490] which predicted the influence of dislocation pile-ups being held up at polycrystal grain boundaries:

$$\sigma = \sigma_0 + k_y d^{-1/2} \tag{18}$$

where σ_0 is friction stress resisting the motion of gliding dislocation, and k_y is the Hall-Petch slope, which is associated with a measure of the resistance of the grain boundary to slip transfer, and d is the average grain size.

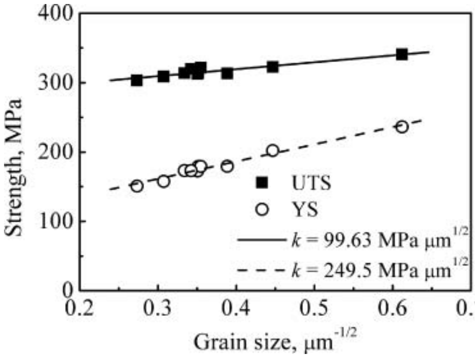

Figure 55. Variation of strength with $d^{-1/2}$ ($\mu m^{-1/2}$) in FSP 5083Al alloy. (© Elsevier. Reprinted with permission from Cui et al.[494] Permission to reuse must be obtained from the rightsholder.)

Cui et al.[494] fabricated a series of fine-grained 5083Al alloy samples with an average grain size of 2.7–13.4 μm by controlling the FSP conditions. It was found that both yield stress (YS) and ultimate tensile strength (UTS) increased with decreasing grain size, and they followed the Hall-Petch relationship well,[494] however the Hall-Petch slope was different, as shown in Figure 55.[494] Similar results have been reported in the FSW/FSP of aluminum,[503] magnesium alloys,[72,75,83,497] and pure copper.[62]

Single-pass FSP can effectively enhance the ductility and strength of the as-cast A356, as shown by Figure 56[438] however, no significant strength difference was observed among various FSP parameters (i.e., rotational rates of 600–1800 rpm and travel speeds of 150–450 mm/min).[438] With increasing the rotational rate at a fixed travel speed, the tensile properties of the FSP samples did not change much; however, after the artificial aging, the strength increased as the rotational rate increased. When increasing the travel speed at a fixed rotational rate, the tensile properties changed little, even

Table 3. Welding parameters and transverse tensile properties of FSW joints of three typical aluminum alloys.[56,175,213]

Materials	Rotational Rate (rpm)	Welding Speed (mm/min)	Strain Rate (s^{-1})	YS (MPa)	UTS (MPa)	El. (%)	Joint Efficiency (%)	Refs.
7075Al-T651	800	100	1×10^{-3}	304	453	10.5	78	213
	800	200	1×10^{-3}	328	499	12.0	86	
	800	400	1×10^{-3}	353	532	15.6	92	
	1000	400	1×10^{-3}	344	527	15.4	91	
	1200	400	1×10^{-3}	356	513	10.4	88	
6061Al-T651	1400	400	4×10^{-4}	—	231	8.1	75	175
	1400	600	4×10^{-4}	—	243	8.6	79	
	1400	200	4×10^{-4}	—	214	8.8	69	
	1200	200	4×10^{-4}	—	211	8.6	69	
	900	200	4×10^{-4}	—	214	8.4	69	
2024Al-T351	400	100	4×10^{-4}	—	412	7.4	86	56
	800	100	4×10^{-4}	—	408	7.0	85	
	1200	100	4×10^{-4}	—	416	7.8	87	
	800	200	4×10^{-4}	—	439	8.0	89	
	800	400	4×10^{-4}	—	451	14.7	94	

Table 4. Effect of cooling condition on tensile strength of FSW joints of various aluminum alloys.[14,195,507–510]

BM	Plate thickness (mm)	Rotational rate (rpm)-welding speed (mm/min)	Cooling condition	Max UTS_{FSW}, (MPa)	UTS_{FSW}/ UTS_{BM}, (%)	Refs.
7050Al-T4	5.50	800–100	AC	325	82	507
			WC	340	86	
7050Al-T7451	6.35	650–408	AC	515	98	195
			WC	535	105	
7075Al-T6	3.00	715–105	AC	356	81	508
			WC	382	87	
7075Al-T7351	9.53	—	AC	405	80	14
			WC	450	89	
2195Al-T8	6.50		AC	410	71	
			WC	415	72	
2014Al-T6	6.00	800–100	AC	366	78	509
			WC	369	79	
2219Al-T6	5.60	800–100	AC	320	72	510
			WC	332	75	
		800–400	AC	341	77	
			WC	352	80	
		800–800	AC	349	79	
			WC	352	80	

*Air cooling: AC, Water cooling: WC

after the artificial aging.[438] The two-pass FSP A356 sample exhibited better tensile properties than the single-pass sample. A further increase in the number of FSP passes only resulted in a slight improvement in the tensile properties of the FSP samples.[438] After post-FSP aging, the tensile strength of the FSP A356 samples increased significantly due to the precipitation of dissolved Mg atoms (Figure 56).[438]

4.2.2. Effect of water cooling

It is well known that welding heat input affects the microstructural evolution in various zones and thereby influences the mechanical properties of the FSW joints of aluminum alloys.[504–506] In addition to controlling the FSW parameters, active cooling is used during FSW to reduce the welding heat input to inhibit the softening of various zones, in particular the HAZs. The effect of water cooling on tensile strength of FSW joints of several precipitation-hardened aluminum alloys are summarized in Table 4.[14,195,507–510] It is noted that water cooling exhibited distinctly different effects on the tensile strength of FSW joints for different aluminum alloys. For 7075Al and 7050Al alloys, water cooling largely improved the tensile strength of the FSW joints,[14,195,507,508] whereas for 2195Al, 2014Al, and 2219Al alloys, water cooling marginally enhanced the tensile strength of the FSW joints.[14,509,510]

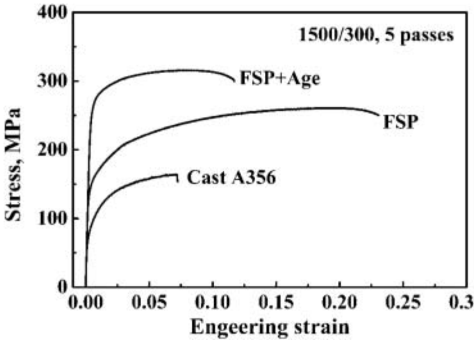

Figure 56. Typical tensile curves of five-pass FSP A356 sample at a rotational rate of 1500 rpm and a travel speed of 300 mm/min. (© Springer. Reprinted with permission from Cui et al.[438] Permission to reuse must be obtained from the rightsholder.)

Nelson et al.[14] suggested that the effect of water cooling on the mechanical properties of the FSW joints of aluminum alloys was associated with the quench sensitivity of aluminum alloys. As shown in Figure 57,[14] quench sensitive aluminum alloys (such as 7075Al alloy) exhibit an abrupt changes in the tensile strength with the quench rate, while the tensile strength of less quench sensitive aluminum alloys (such as 2195Al and 2014Al alloys) vary only slightly. The variation of tensile strength for submerged FSW joints of 7075Al, 2195Al, and 2014Al alloys could be reasonably explained by their quench sensitivity. However, this cannot be used to account for the change in the tensile strength of FSW 7050Al alloy because 7050Al alloy is less quench sensitive. Clearly, there exist some other factors influencing the role of water cooling in the FSW process.

Zhang et al.[509] suggested that the effect of water cooling on the tensile strength of the FSW joints of aluminum alloys was associated with the position of the LHZs relative to the shoulder. Under the water cooling condition, the heat input of the zone far from the welding tool was significantly reduced by the water, while for the zone close to the welding tool, the heat input was less inhibited by the water. Water cooling move the position of LHZs from A_1 to A_2 for FSW joints of 7050Al and 7075Al alloy

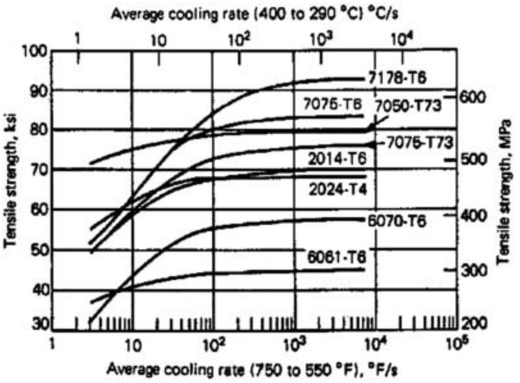

Figure 57. Variation of tensile strength of aluminum alloys with average cooling rate during quenching.[14]

and from B_1 to B_2 for FSW joints of 2195Al, 2014Al, and 2219Al alloys (Figure 58).[509] During this process, the LHZs of the water cooling FSW joints experienced a short time of direct heating by the welding tool from A'_2 to A''_2, resulting in that water cooling would shortened the duration above the phase-transition temperatures considerably for FSW joints of 7050Al and 7075Al alloys. In contrast, the LHZs of the water cooling FSW joints experienced a long time of direct heating by the shoulder from B'_2 to B''_2; in this case, the duration above the phase-transition temperatures was less affected by the water for FSW joints of 2195Al, 2014Al, and 2219Al alloys. Thus, water cooling considerably improved the tensile strength of the FSW joints of 7075Al and 7050Al alloys,[14,195,507,508] but marginally (<3%) increased the tensile strength of the FSW joints of 2195Al, 2014Al, and 2219Al alloys.[14,509,510]

4.2.3. *Effect of characteristic microstructures*

The effect of the zigzag line and kissing bond on the tensile properties of the as-welded joints remained controversial as a result of different states of break-up of the oxide arrays.[262,511–513] Peel et al.[262] found that FSW 5083Al joints welded at a higher welding speed of 200 mm/min failed along the zigzag line and the UTS (186 MPa) was significantly lower than that (304 MPa) welded at a lower traverse speed of 100 mm/min which failed around 10 mm from the zigzag line. Chen et al.[511] reported that during FSW of a 5456Al alloy, the presence of kissing bond resulted in a reduction of tensile strength of joints and the zigzag line was the important cause for the dramatic decrease of ductility. However, Liu et al.[512] pointed out that the tensile properties of as-welded joints of 2219Al-O alloy were barely affected by the zigzag line because the broken oxide particles were distributed in a dispersed and discontinuous way along the grain boundaries. Chen et al.[514] found that the initial surface oxide had a profound influence on the tensile properties of FSW 2219Al alloys. The tensile strength of FSW 2219Al joints with the initial oxide remnant inside the SZ, only reached about 60% of a sound FSW joint.[514]

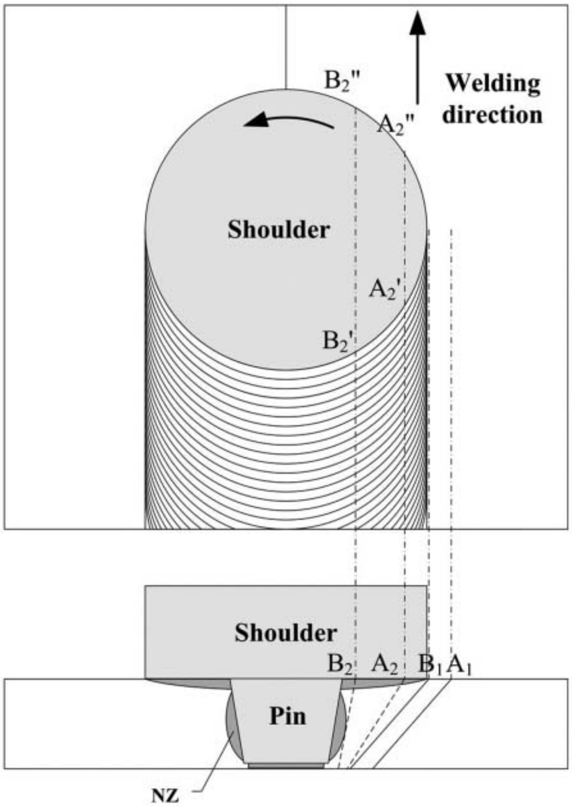

Figure 58. Schematic positions of LHZs relative to welding tool for FSW joints of different aluminum alloys. (© Elsevier. Reprinted with permission from Zhang et al.[509] Permission to reuse must be obtained from the rightsholder.)

By comparing the tensile properties of FSW Al-Mg-Sc alloy joints failed at the zigzag line or kissing bond and at the NZ/TMAZ boundary, Tao et al.[176] revealed that neither the zigzag line nor kissing bond exerted a significant influence on the UTS. Besides, they also pointed out that whether the zigzag line had an effect on the fracture behavior of FSW joints depended on two prerequisites. One was a continuous zigzag line with very low extent of disruption. The other was a roughly homogeneous hardness profile, i.e., no obvious LHZ was observed. Only if both conditions are satisfied the fracture at the zigzag line may occur during tension.

However, the zigzag line was found to be deleterious to the tensile properties of post-weld heat-treated joints.[476,512] Ren et al.[476] reported that the zigzag line did not show up in the FSW 7075Al-T651 alloy joints. However, after post-weld T6-treatment, the zigzag line appeared and the joints failed along the zigzag line during tension, which resulted in the reduced tensile strength and significantly deteriorated ductility. Liu et al.[512] found out that tensile properties of the FSW

2219Al-O alloy joints after post-weld heat-treatment were seriously deteriorated by the zigzag line, which was attributed to the generation of micro-cracks along the zigzag line during the post-weld heat treatment.

Sutton et al.[242] reported that the secondary phase particles were broken up and redistributed along the onion ring bands in a FSW 2024Al-T351 alloy joint and the FSW joint tended to fracture along the regions with a high density of secondary phase particles during mixed-mode I/II monotonic fracture experiments. Moreover, Zhang et al.[171] revealed that the segregation bands in FSW 2024Al-T351 alloy joints, consisting of second phase particles, resulted in an unusual tensile fracture behavior along the segregation bands at higher welding speeds of 200 and 400 mm/min at a constant tool rotational rate of 800 rpm.

4.3. *Superplasticity*

Superplasticity refers to the ability of metallic alloys to exhibit a high uniform elongation prior to failure[515] There are two major microstructure requirements for achieving superplastic deformation.[516] First, a fine equiaxed grain size, typically less than 15 μm, is required.[41] Second, the thermal stability of the fine-grained microstructure should be another consideration.[517] Once AGG occurred, it will result in the disappearance of superplasticity.[398]

Various fabrication/processing techniques, such as SPD techniques, powder metallurgy,[518] multi-step thermomechanical processing,[519,520] etc., have been used to produce fine-grained aluminum alloys. As described above, FSP developed on the basis of the principles of FSW, provides a very simple and effective approach for obtaining fine-grained structure.[41,521] Typically, FSP can reduce the grain size to micrometer or even submicrometer/nanometer level with a HAGB volume fraction as high as 85–97%,[522], thereby obtaining materials exhibiting superplasticity characteristics. Previous studies confirmed that superplasticity could be achieved in various FSP aluminum alloys, such as 1xxx-series aluminum alloys,[523] 2xxx-series aluminum alloys,[43,524,525] 4xxx-series aluminum alloys,[526] 5xxx-series aluminum alloys,[527,528],6xxx-series aluminum alloys,[529] and 7xxx-series aluminum alloys,[2,28,41,208,399,530] and Al-Mg-Zr alloys.[517,531]

4.3.1. *High-strain-rate superplasticity*

Conventional superplasticity is typically achieved at slow strain rates (10^{-4}–10^{-3} s^{-1}) and higher homologous temperatures (0.8 T_m).[46] High-strain-rate superplasticity (HSRS) refers to the superplasticity achieved at an optimum strain rate of $\geq 1 \times 10^{-2}$ s^{-1}. Superplasticity is often characterized using a generalized constitutive equation:

$$\dot{\varepsilon} = A\frac{DGb}{kT}\left(\frac{b}{d}\right)^{p}\left(\frac{\sigma}{G}\right)^{n}, \tag{19}$$

where $\dot{\varepsilon}$ is the strain rate, A is a dimensionless constant with a value of 25–50, D is an appropriate diffusivity (lattice or grain boundary), G is the shear modulus, b is the Burger's vector, k is the Boltzmann constant, T is the absolute temperature, p is the grain size exponent, d is the grain size, σ is the applied stress, and n is the stress exponent.

According to the prediction by Eq. (19), the optimum strain rate increased with decreasing grain size. Based on the fine grain size of 0.6–10 μm produced in aluminum alloys via FSP, it is expected that the FSP fine-grained aluminum alloys would exhibit a high strain rate superplastic behavior with the decrease in the grain size. Table 5 summarizes the superplastic data of a number of FSP aluminum alloys at high strain rates.[41,43,46,516,532–534] It is indicated that an elongation of as high as 2150% was achieved at 450°C and a high strain rate of 1×10^{-1} s^{-1} in a micro-grained Al-Mg-Sc alloy produced by FSP (Figure 59).[534] Furthermore, an exceptional high elongation of 3250%, which is the largest superplasticity even reported in the 7075Al alloy, was obtained at 535°C and 1×10^{-2} s^{-1} in a FSP 7075Al alloy with a grain size of 6.2 μm.[532]

It is important to point out that the optimum strain rate for obtaining the largest elongation in the 7xxx aluminum alloy prepared by FSP is more than one order of magnitude higher than that by thermo-mechanical processing (the previous best result on a 7xxx-series aluminum alloy).[535] This clearly illustrates the effectiveness of FSP for processing fine-grained materials that are amenable to HSRS. Excellent HSRS of FSP fine-grained aluminum alloys is attributed to uniform and equiaxed grains and high fraction of HAGBs (Figure 27[43] and Figure 28[398]), which is generally considered to be beneficial to the occurrence of GBS that is the primary superplastic deformation mechanism in the fine-grained alloys.

4.3.2. *Low-temperature superplasticity*

Ideal low-temperature superplasticity (LTSP) should be obtained at temperatures of below 0.5 T_m.[46,536] For alu-

Table 5. Summary of high strain rate superplasticity in FSP aluminum alloys.[41,43,46,516,532–534]

Alloy	Grain size (μm)	Temperature (°C)	Strain rate (s^{-1})	Elongation (%)	Refs.
7075	3.8	480	1×10^{-2}	1250	41
7075	6.2	535	1×10^{-2}	3250	532
2024	3.9	430	1×10^{-2}	525	43
Al-4Mg-1Zr	1.5	525	1×10^{-1}	1280	516
Al-4Mg-1Zr	0.7	375	3×10^{-1}	1410	533
Al-Zn-Mg-Sc	0.7	310	3×10^{-2}	1800	46
Al-Mg-Sc	2.6	450	1×10^{-1}	2150	534

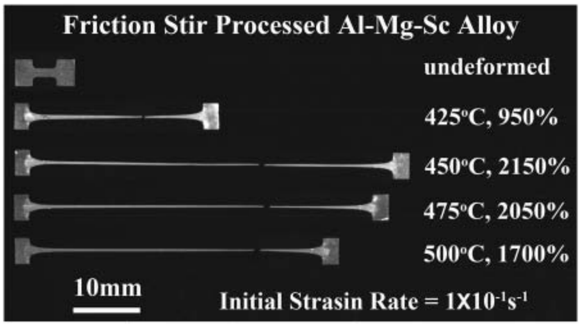
Friction Stir Processed Al-Mg-Sc Alloy
undeformed
425°C, 950%
450°C, 2150%
475°C, 2050%
500°C, 1700%
10mm
Initial Strasin Rate = 1X10^{-1}s^{-1}

Figure 59. Tensile samples of FSP Al-Mg-Sc alloy pulled to failure at a strain rate of 1×10^{-1} s^{-1} at different temperatures. (© Elsevier. Reprinted with permission from Liu & Ma.[534] Permission to reuse must be obtained from the rightsholder.)

minum alloys, the corresponding temperature for ideal LTSP is about ~190°C or lower. According to Eq. (19), the optimum superplastic temperature would decrease with decreasing grain size. Therefore, considerable efforts have been devoted to achieve LTSP by refining the grain size to the submicrometer in the past decade.[537,538] Unfortunately, it was proven by many investigators that it is difficult to achieve superplasticity at this temperature range even for UFG aluminum alloys.[537–540] The lowest temperature for superplasticity of UFG aluminum alloys prepared by various SPD techniques is reported to be 200°C.[537–540] Therefore, the superplasticity achieved at temperatures ≤ 350°C is usually considered as LTSP for aluminum alloys.[537,538]

It is well documented that by controlling FSP heat input and cooling condition, the fully recrystallized UFG with a uniform and equiaxed grain size distribution and a high fraction of HAGBs could be generated in aluminum alloys.[46,209,398,536,541] It is expected that excellent LTSP can be achieved in these FSP UFG aluminum alloys. Table 6 summarizes the LTSP of various FSP aluminum alloys. It was indicated that excellent LTSP was obtained in FSP UFG Al-Zn-Mg-Sc,[46] Al-Mg-Zr,[209] Al-Mg-Sc alloy,[398,541] and 7075Al alloy[536] samples. Especially, superplasticity was achieved in FSP UFG Al-Mg-Zr and Al-Mg-Sc alloys at a temperature as low as 175°C (0.48 T_m).[209,541] This is the first report about the superplasticity of aluminum alloys at temperatures lower than 200°C.

Table 6. Summary of low temperature superplasticity in FSP aluminum alloys at temperatures ≤ 300°C.[46,209,536,541]

Alloy	Grain size (μm)	Temperature (°C)	Strain rate (s^{-1})	Elongation (%)	Refs.
Al-Zn-Mg-Sc	0.7	220	1×10^{-3}	510	46
		250	3×10^{-3}	465	
		290	3×10^{-2}	940	
Al-4Mg-1Zr	0.7	175	1×10^{-4}	240	209
		200	1×10^{-4}	470	
		250	3×10^{-3}	740	
		300	3×10^{-2}	1160	
Al-Mg-Sc	0.6	175	1×10^{-4}	210	541
		200	3×10^{-4}	265	
		250	3×10^{-3}	530	
		300	1×10^{-2}	560	
7075	0.8	200	1×10^{-5}	350	536
		250	3×10^{-4}	400	
		300	1×10^{-3}	530	

Good superplasticity of FSP UFG aluminum alloys at temperatures as low as 175°C is ascribed to the uniform and equiaxed UFG microstructure with a high fraction of HAGBs created by FSP.[46,209,398,536] Liu and Ma[541] examined the contribution of GBS to strain in LTSP of UFG aluminum alloys by using a nano-indenter. It was revealed that the contribution of GBS to strain exceeded 50% even at 175°C, indicating that GBS is still a predominant superplastic deformation mechanism even at 0.48 T_m.[541] This provides direct evidence for the superplastic deformation mechanisms of ultrafine-grained aluminum alloys at low temperatures, which have been the subject of debate in the past two decades.[537,539,540]

4.3.3. Enhanced uperplasticity

The constitutive relationship for superplasticity in fine-grained aluminum alloys could be expressed as:[542]

$$\dot{\varepsilon} = 40\frac{D_0 E b}{kT}\exp\left(-\frac{84000}{RT}\right)\left(\frac{b}{d}\right)^2\left(\frac{\sigma-\sigma_0}{E}\right)^2, \qquad (20)$$

where D_0 is the pre-exponential constant for diffusivity, E is Young's modulus, R is the gas constant, and σ_0 is the threshold stress. The dimensionless constant of 40 is consistent with that in Eq. (19) with a value of 2550.

When analyzing the superplastic data of the FSP 7075Al alloy, Ma et al.[41] for the first time reported enhanced deformation kinetics in the FSP aluminum alloy compared with the prediction by Eq. (20). In Figure 60, the superplastic data of the FSP Al-4Mg-1Zr and 7075Al alloys are plotted as $(\dot{\varepsilon}kTd^2\ /\ D_g Eb^3)$ vs. $(\sigma\text{-}\sigma_o)/E$.[41] It was indicated that the superplastic deformation behavior of both FSP Al-4Mg-1Zr and 7075Al alloy can be described by a united constitutive equation:[517]

$$\dot{\varepsilon} = 700\frac{D_0 E b}{kT}\exp\left(-\frac{84000}{RT}\right)\left(\frac{b}{d}\right)^2\left(\frac{\sigma-\sigma_0}{E}\right)^2 \qquad (21)$$

It is proposed that the dimensionless constant in Eq. (19) is a function of the fraction of HAGBs and increases as the fraction of HAGBs increases.[517] Equation (21) implies that enhanced kinetics may be a common feature for FSP aluminum alloys.[517] GBS, grain rotation, and grain boundary migration are the main

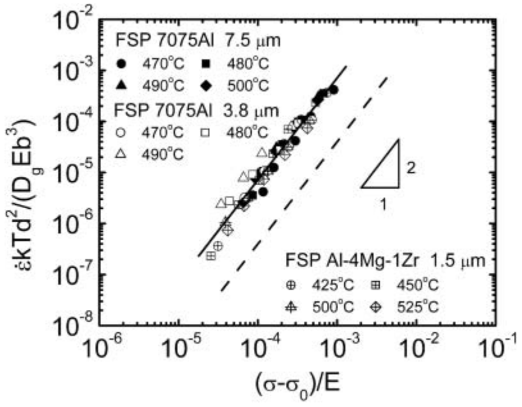

Figure 60. Variation of $(\dot{\varepsilon}kTd^2\ /\ (D_geb^3))$ with normalized effective stress, $(\sigma\text{-}\sigma_0)/E$, for Al-4Mg-1Zr and 7075Al alloys (Dashed line represents Eq. (20). (© Taylor & Francis. Reprinted with permission from Ma et al.[517] Permission to reuse must be obtained from the rightsholder.)

processes associated with the activity of grain boundaries during superplasticity.[543]

4.4. Fatigue behavior

While a lot of tensile property data on the FSW/FSP aluminum alloys are available in the open literature, the establishment of fatigue property database especially the strain-controlled fatigue life is needed since such data are required in industry to estimate the life of structural components and to guarantee the structural integrity, reliability, and longevity of the FSW/FSP aluminum alloy joints. For the FSW/FSP materials, fatigue strength/life or S-N curves,[90,437,544–553] and fatigue crack propagation behavior[36,203,206,211,437,554–558] have been well documented especially in the earlier articles.[4–7,559]

In the present review article, strain-controlled fatigue life or low/high cycle fatigue (LCF/HCF) behavior of FSW aluminum alloys in relation to the LHZs is summarized. While only limited studies on the LCF of FSW aluminum alloys have been reported,[51,150,212,560–564] the strain-controlled fatigue life data are indeed required by automobile manufacturers to estimate the lifetime of components in design.

It was reported that the tensile fracture path of the welds corresponded to the LHZs.[50,175] Although several studies have offered important insights in this regard, it is still unclear how the LHZs and the relevant FSW parameters affect LCF properties. Two LHZs appeared in the HAZs adjacent to the border between the TMAZ and HAZ, with the width decreasing with increasing welding speed (Figure 51).[51] Cyclic hardening of the FSW joints was appreciably stronger than that of the BM, and it also exhibited a two-stage character where cyclic hardening of the FSW 6061Al-T651 alloy at higher strain amplitudes was initially stronger followed by an almost linear increase of cyclic stress amplitudes on the semi-log scale (Figure 61).[212] Fatigue life, cyclic yield strength, cyclic strain hardening exponent, and cyclic strength coefficient all increased with increasing welding speed, but nearly independent of the rotational rate.[212] The total strain amplitude could be expressed as elastic strain amplitude ($</\Delta\varepsilon_e/2$) and plastic strain amplitude ($\Delta\varepsilon_p/2$), i.e.,

$$\left(\frac{\Delta\varepsilon_t}{2}\right)=\left(\frac{\Delta\varepsilon_e}{2}\right)+\left(\frac{\Delta\varepsilon_p}{2}\right) \tag{22}$$

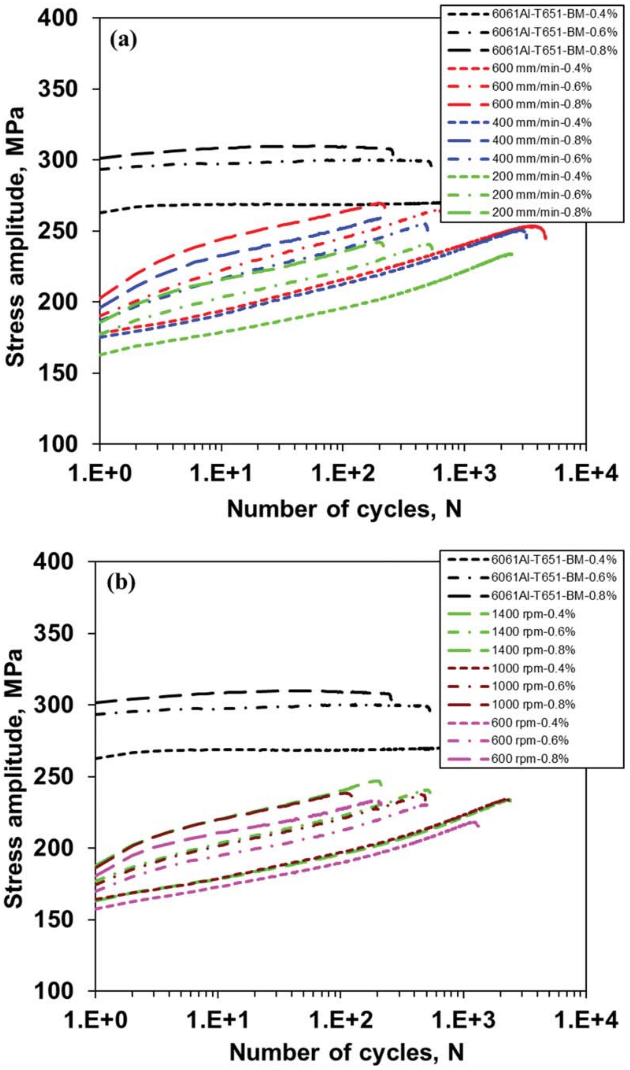

Figure 61. Stress amplitude *vs* number of cycles at different total strain amplitudes for 6061Al-T651 alloy: (a) different welding speeds at a rotational rate of 1400 rpm, (b) different rotational rate at a welding speed of 200 mm/min. (© Springer. Reprinted with permission from Feng et al.[212] Permission to reuse must be obtained from the rightsholder.)

The first part could further be expressed in terms of Basquin equation:

$$\frac{\Delta\varepsilon_e}{2} = \frac{\sigma'_f(2N_f)^b}{E} \tag{23}$$

and the second term of Eq. (22) could be replaced by the Coffin-Manson relation,

$$\frac{\Delta\varepsilon_p}{2} = \varepsilon'_f(2N_f)^c; \tag{24}$$

then,

$$\frac{\Delta\varepsilon_t}{2} = \frac{\sigma'_f(2N_f)^b}{E} + \varepsilon'_f(2N_f)^c \tag{25}$$

where N_f is the fatigue life or the number of cycles to failure, σ'_f is the fatigue strength coefficient, ε'_f is the fatigue ductility coefficient, and c is the fatigue ductility exponent.

Fatigue deformation was observed to follow the Coffin-Manson and Basquin's equations well.[51,212] Akin to the cyclic yield strength, cyclic strain hardening exponent and cyclic strength coefficient, the fatigue strength coefficient of the FSW joints also increased with increasing welding speed. The absolute value of fatigue strength exponent of the FSW joints also slightly increased, while the fatigue ductility coefficient and fatigue ductility exponent (absolute value) decreased as the welding speed increased from 200 to 600 mm/min. No strong effect of the rotational rate on the fatigue parameters could be seen. Based on the Smith, Watson, and Topper (SWT) equation:[565]

$$\sigma_{\max}\varepsilon_a = \frac{(\sigma'_f)^2}{E}(2N_f)^{2b} + \sigma'_f\varepsilon'_f(2N_f)^{b+c}, \tag{26}$$

where $\sigma_{\max}$ is the maximum stress at the saturation or mid-life and ε_a is the strain amplitude ($\Delta\varepsilon/2$). Both the experimental data in the form of $\sigma_{\max}\varepsilon_a$ and Eq. (25) are plotted in Figure 62.[212] It is seen that the obtained fatigue life followed the SWT equation well.

Figure 63 showed the failed LCF specimens.[212] The majority of FSW joints failed along the LHZs and exhibited a shear fracture mode. The shear fracture path was oriented at an angle of about 45–60° to the tensile axis. Fatigue crack initiation was observed to occur at the specimen surface or near-surface welding defect in the FSW joints and crack propagation was characterized by the characteristic fatigue striations together with some secondary cracks, as shown in Figure 64.[212]

Recently, Wang et al.[566] reported the HCF and crack growth behavior of the FSW joint of UFG 2024Al alloy. It was indicated that NaCl solution significantly reduced the fatigue strength of the joints, and the fatigue crack propagation rates in the NZ and HAZ were slower than that in the BM in the whole fatigue life.[566] Yan et al.[275] reported that the dissimilar FSW joints of Al-Mg-Si/Al-Zn-Mg alloys owned better fatigue properties, such as the fatigue lives and S-N curves, when the Al-Zn-Mg alloy was placed on the AS, because crack closure effect was easier to happen.

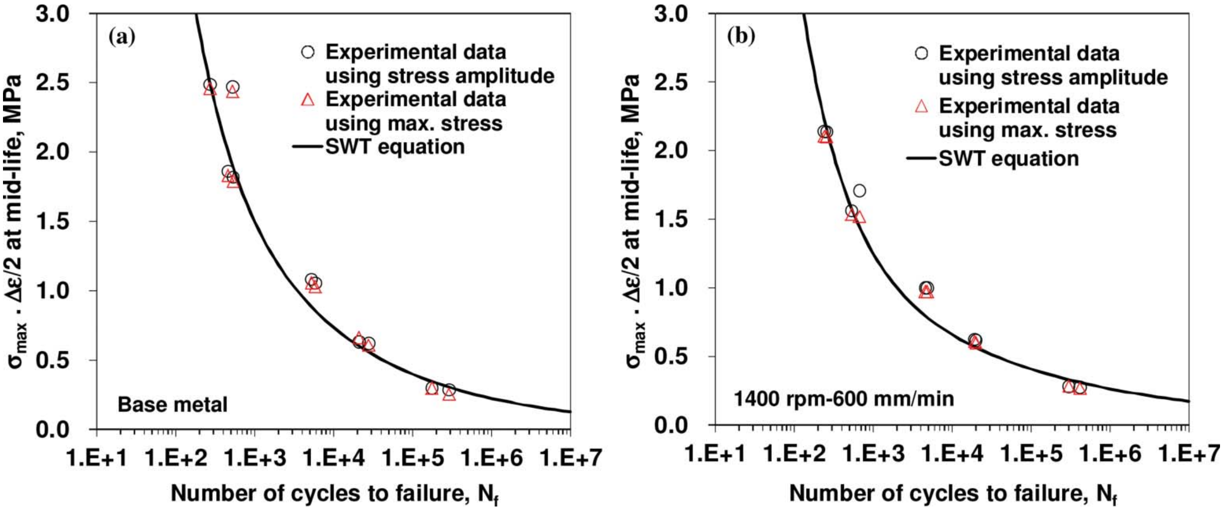

Figure 62. Product of maximum stress with strain amplitude as a function of number of cycles to failure for (a) BM and (b) FSW joint (1400 rpm and 600 mm/min). (© Springer. Reprinted with permission from Feng et al.[212] Permission to reuse must be obtained from the rightsholder.)

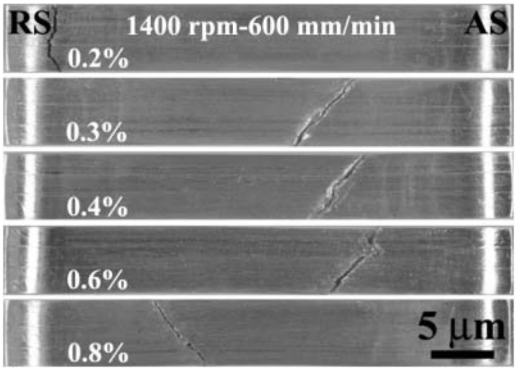

Figure 63. Typical optical micrographs showing failure locations of FSW 6061Al-T651 alloy joint fatigued at varying total strain amplitudes (1400 rpm and 600 mm/min). (© Springer. Reprinted with permission from Feng et al.[212] Permission to reuse must be obtained from the rightsholder.)

5. Outlooks

FSW is finding greater use in automobile, railway and aerospace applications through advances in equipment intelligence, material development evaluations, structural design and testing programmes, tooling and process innovations.[4,567] FSW of aluminum alloys has emerged as one of the top enabling technologies, allowing the fabrication of very large single piece components.[568] To date, even though the FSW technique was initially developed for aluminum alloys,[9] it has been developed to a stage where it is applied in production toward the high melting materials, such as steel,[569] titanium,[119] and titanium-based alloys,[570], as well as MMCs.[152]

Recently, application of FSW of thick aluminum alloy plates has gradually increased.[58] FSW of thick aluminum

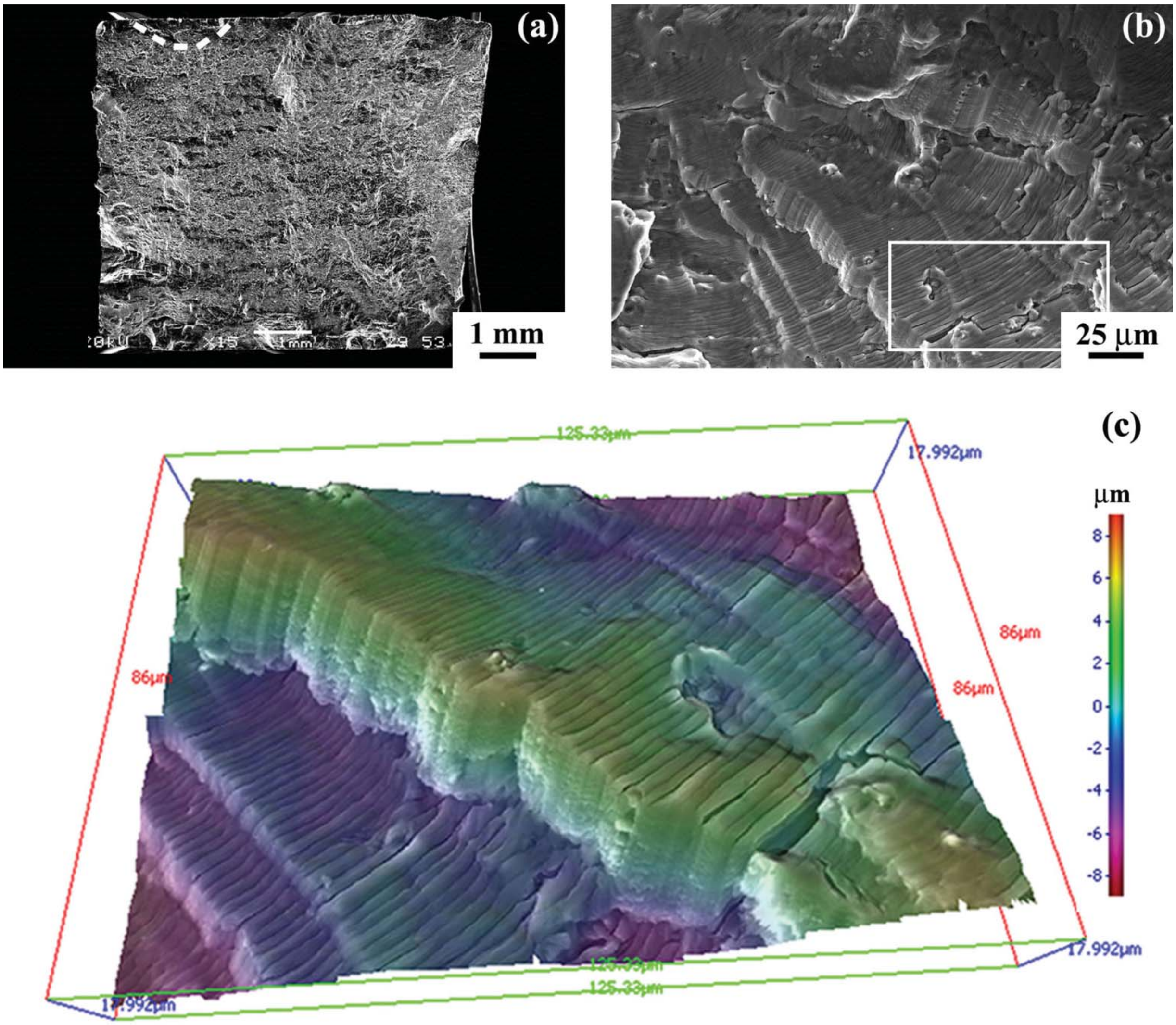

Figure 64. Typical SEM micrographs of FSW 6061Al-T651 alloy joint fatigued at a total strain amplitude of 0.6% (1400 rpm and 600 mm/min): (a) overall view of fracture surface, (b) a magnified view near the initiation site, (c) a 3D image of rectangular dashed line box in (b). (© Springer. Reprinted with permission from Feng et al.[212] Permission to reuse must be obtained from the rightsholder.)

alloy plates is more challenging than FSW of thin ones, such as 2xxx-series,[571–574] 5xxx-series,[58] 6xxx-series,[575,576] and 7xxx-series aluminum alloys.[58,575,577–579]

Some modified FSW techniques may be a potential solution, such as back heating assisted welding,[580] underwater joining technology,[505,581] stationary shoulder,[582] reverse dual-rotation FSW (RDR-FSW),[583] laser-assisted FSW/FSP,[288,584] and ultrasonic-assisted FSW/FSP.[585–587]

FSW offers additional avenues to unitization of structural components.[163] Joining of tailored welded blanks with FSW is very attractive for future aircraft applications.[588] Lap and butt joining of thin-sheet materials provides an alternative to conventional joining/fastening. Taavitsainen et al.[589] reported that the production by FSW of free-shape hollow box profile in 5754Al alloys for automotive application. In automotive industry, the innovation is based on a new clamping system enabling the use of a conventional tool architecture.[589] While it is easy to join flat plate with FSW, it is challenging to extend its applications to include tubes, in particular small diameter tubes, and other complex geometries.[590]

Recently, robotic FSW systems have been utilized in various industrial applicaions.[591] Qin et al.[592] reported a method of real-time motion control for robotic FSW. The efficiency of robotic FSW could be further improved using robust control strategies.[592] Mendes et al.[593] presented the concept and design of a novel FSW robotic platform for welding polymeric materials.

Furthermore, friction stir additive manufacturing (FSAM) based on FSW principle was currently used to build successfully a multilayered stack of an Al-based component.[594] FSAM has a huge potential to fabricate lightweight materials with high structural performances.[594]

There are some limitations in this article. Some important key issues remain to be addressed, such as the corrosion resistance of FSW joint. Therefore, to advance FSW from the research stage into industry application, corrosion resistance evaluations is one of the most importance consideration in the future.[305,310,557,595–598]

6. Conclusions

This article briefly summarized the latest advances and rapidly growing knowledge involving the FSW/FSP of aluminum alloys, with particular emphasis on the processing-microstructure-mechanical property relationships.

FSW/FSP can be regarded as a type of high-temperature SPD, involving transients and steep gradients in strain, strain rate, and temperature. The material flow during FSW is quite complex depending on the tool geometry, process parameters, and material to be welded. Recent experimental and computational works have provided significant insight about the understanding of the progress on the relationship among the strain, strain rate, temperature and their distribution during FSW/FSP. In FSW/FSP of aluminum alloys, depending on the materials, tool design, and operating conditions, the maximum values of equivalent strains were estimated to range from 6–133, the strain rate was determined to be 1.0–20 s^{-1}, and the maximum temperature could approach ~0.8 T_m, or even 0.95 T_m.

During FSW/FSP, a variety of microstructural changes including recrystallization, grain growth, phase transformation have been identified in various zones. Full recrystallization occurred in the NZ of the FSW/FSP aluminum alloys, resulting in the refinement of grain sizes down to micrometer or even nanometer and a high fraction of HAGBs (85–97%), which is much higher than that obtained in conventional thermomechanically processed aluminum alloys. Various recrystallization mechanisms, including CDRX, DDRX, GDRX, TDRX, and PSN have been recognized as possible operative mechanisms in FSW/FSP aluminum alloys dependent on the compositions and microstructures of the aluminum alloys and applied processing conditions.

The precipitation sequence in the FSW/FSP aluminum alloys remained the same as the BMs; however, complex phase transformation occurred in various zones. For the precipitation-hardened aluminum alloys, the primary strengthening precipitates originally existing in the BMs were either dissolved or coarsened, leading to the formation of two LHZs positioned in the HAZs (close to the border of HAZ/TMAZ). Under various FSW parameters, the LHZs experienced approximately the same peak temperature with varied durations that were mainly governed by the welding speed.

It is difficult to experimentally measure the temperature distribution and history during FSW, in particular in the NZ. An equivalent friction coefficient based heat generation model was proposed for FSW thermal modeling and simulation. The equivalent friction coefficient depended on temperature and was determined via an inverse solution framework. This model could predict the temperature histories accurately in various welding conditions. The temperature distribution contributes to further understanding the hardness distribution and mechanical properties of the FSW joints.

Characteristic microstructures, including the onion-ring structure, segregation band, zigzag line, and kissing bond, were formed in the NZ of FSW/FSP aluminum alloys, due to the unique and complex deformation mode. The formation of the onion-ring structure and segregation band was attributed to the periodical material flow, and could be described by the mathematics equations, with the ring/band spacing equal to the tool advancement per revolution. The zigzag line and kissing bond were indentified to result from the oxide layer on the initial butt surfaces of aluminum plates by FIB-assisted TEM examinations and the comparative study of FSW and FSP. Generally, high FSW heat-input contributes to reduce the formation of zigzag line and kissing bond.

The texture in the NZ was either weak or present in a complex pattern such as the typical shear texture component induced by the rotating shear plastic flow along the pin surface. The local textures were diretly related to the welding parameters, i.e., the rotational rate and welding speed.

For the precipitation-hardened aluminum alloys, the mechanical properties and the fracture behavior of FSW joints were directly governed by the hardness value and the position of the LHZs. Generally, the strength of the FSW joints increased with increasing welding speed and was almost independent of the rotational rate and the tool dimension, which can be well explained by the heat source zone–isothermal dissolution layer (HSZ-ITDL) model. Water cooling could largely improve the tensile strength of the FSW joints of 7075Al and 7050Al alloys, but marginally enhanced the joint strength of 2195Al, 2014Al, and 2219Al alloys, which was mainly attributed to the difference in the quench sensitivity of aluminum alloys and the position of the LHZs relative to the shoulder.

Generally, the characteristic microstructures—the onion-ring structure, segregation band, zigzag line, and kissing bond—negatively affected the mechanical properties and the fracture behavior of the FSW joints. However, when the broken oxide particles in the zigzag line were distributed in a dispersed and discontinuous form, the zigzag line did not influence the mechanical properties and the fracture behavior of the as-FSW joints because the fracture occurred in the LHZs.

Excellent HSRS and LTSP were observed in the FSP fine-grained aluminum alloys, which was attributed to uniform and equiaxed grains and high fraction of HAGBs. Especially, superplasticity was achieved for the first time in UFG aluminum alloys at a temperature as low as 175°C (0.48 T_m), and GBS was identified to be still a predominant superplastic deformation mechanism even at 0.48 T_m. The enhanced kinetics was reported for the first time in the FSP fine-grained aluminum alloys and attributed to the existence of predominant HAGBs.

Investigations on strain-controlled fatigue behavior indicated that cyclic hardening of the FSW joints of aluminum alloys was appreciably stronger than that of the BM. Fatigue life, cyclic yield strength, cyclic strain hardening exponent, and cyclic strength coefficient of FSW aluminum alloys all increased with increasing the welding speed, but were nearly independent of the rotational rate.

While the extensive studies over the past 20 years have been conducted toward the understanding of FSW/FSP of aluminum alloys, especially the relationships between microstructures and mechanical properties, the optimization of the process via a better tool design and proper selection of welding parameters as well as the development of appropriate specifications in standardizing the FSW/FSP processes and the relevant quality assurance inspections including design codes and joint classifications are still needed.

Funding

The authors would like to thank the support of the National Natural Science Foundation of China (Grant Nos. 51331008 and 51305304), and Natural Sciences and Engineering Research Council of Canada (NSERC), Premier's Research Excellence Award (PREA), NSERC-DAS award, Canada Foundation for Innovation (CFI), and Ryerson Research Chair (RRC) program.

References

1. W. M. Thomas, E. D. Nicholas, J. C. Needham, M. G. Murch, P. Templesmith, and C. J. Dawes, G.B. Patent Application No.9125978.8 (December 1992).
2. R. S. Mishra, M. W. Mahoney, S. X. McFadden, N. A. Mara, and A. K. Mukherjee, High strain rate superplasticity in a friction stir processed 7075 Al alloy, *Scripta Mater.* **42**, 163–168 (2000).
3. A. H. Feng and Z. Y. Ma, Enhanced mechanical properties of Mg-Al-Zn cast alloy via friction stir processing, *Scripta Mater.* **56**, 397–400 (2007).
4. R. S. Mishra and Z. Y. Ma, Friction stir welding and processing, *Mater. Sci. Eng. R* **50**, 1–78 (2005).
5. R. Nandan, T. DebRoy, and Bhadeshia, Recent advances in friction-stir welding - Process, weldment structure and properties, *Prog. Mater. Sci.* **53**, 980–1023 (2008).
6. Z. Y. Ma, Friction stir processing technology: A review, *Metall. Mater. Trans. A* **39A**, 642–658 (2008).
7. P. L. Threadgill, A. J. Leonard, H. R. Shercliff, and P. J. Withers, Friction stir welding of aluminum alloys, *Int. Mater. Rev.* **54**, 49–93 (2009).
8. Y. X. Gan, D. Solomon, and M. Reinbolt, Friction stir processing of particle reinforced composite materials, *Materials* **3**, 329–350 (2010).
9. G. Cam, Friction stir welded structural materials: Beyond Al-alloys, *Int. Mater. Rev.* **56**, 1–48 (2011).
10. A. Simar, Y. Bréchet, B. D. Meester, A. Denquin, C. Gallais, and T. Pardoen, Integrated modeling of friction stir welding of 6xxx series Al alloys: Process, microstructure and properties, *Prog. Mater. Sci.* **57**, 95–183 (2012).
11. X. C. He, F. S. Gu, and A. Ball, A review of numerical analysis of friction stir welding, *Prog. Mater. Sci.* **65**, 1–66 (2014).
12. K. P. Mehta and V. J. Badheka, A review on dissimilar friction stir welding of copper to aluminum: Process,

properties, and variants, *Mater. Manuf. Process.* **31**, 233–254 (2016).

13. T. R. McNelley, S. Swaminathan, and J. Q. Su, Recrystallization mechanisms during friction stir welding/processing of aluminum alloys, *Scripta Mater.* **58**, 349–354 (2008).
14. T. W. Nelson, R. J. Steel, and W. J. Arbegast, In situ thermal studies and post-weld mechanical properties of friction stir welds in age hardenable aluminium alloys, *Sci. Technol. Weld. Join.* **8**, 283–288 (2003).
15. Y. S. Sato, M. Urata, and H. Kokawa, Parameters controlling microstructure and hardness during friction-stir welding of precipitation-hardenable aluminum alloy 6063, *Metall. Mater. Trans. A* **33A**, 625–635 (2002).
16. D. P. Field, T. W. Nelson, Y. Hovanski, and K. V. Jata, Heterogeneity of crystallographic texture in friction stir welds of aluminum, *Metall. Mater. Trans. A* **32A**, 2869–2877 (2001).
17. R. S. Mishra, Preface to the viewpoint set on friction stir processing, *Scripta Mater.* **58**, 325–326 (2008).
18. K. J. Colligan and R. S. Mishra, A conceptual model for the process variables related to heat generation in friction stir welding of aluminum, *Scripta Mater.* **58**, 327–331 (2008).
19. H. B. Schmidt and J. H. Hattel, Thermal modelling of friction stir welding, *Scripta Mater.* **58**, 332–337 (2008).
20. A. P. Reynolds, Flow visualization and simulation in FSW, *Scripta Mater.* **58**, 338–342 (2008).
21. W. J. Arbegast, A flow-partitioned deformation zone model for defect formation during friction stir welding, *Scripta Mater.* **58**, 372–376 (2008).
22. R. W. Fonda, K. E. Knipling, and J. F. Bingert, Microstructural evolution ahead of the tool in aluminum friction stir welds, *Scripta Mater.* **58**, 343–348 (2008).
23. K. Masaki, Y. S. Sato, M. Maeda, and H. Kokawa, Experimental simulation of recrystallized microstructure in friction stir welded Al alloy using a plane-strain compression test, *Scripta Mater.* **58**, 355–360 (2008).
24. Z. Y. Ma, A. L. Pilchak, M. C. Juhas, and J. C. Williams, Microstructural refinement and property enhancement of cast light alloys via friction stir processing, *Scripta Mater.* **58**, 361–366 (2008).
25. I. Charit and R. S. Mishra, Abnormal grain growth in friction stir processed alloys, *Scripta Mater.* **58**, 367–371 (2008).
26. M. J. Starink, A. Deschamps, and S. C. Wang, The strength of friction stir welded and friction stir processed aluminium alloys, *Scripta Mater.* **58**, 377–382 (2008).
27. C. S. Paglia and R. G. Buchheit, A look in the corrosion of aluminum alloy friction stir welds, *Scripta Mater.* **58**, 383–387 (2008).
28. I. Charit, R. S. Mishra, and M. W. Mahoney, Multi-sheet structures in 7475 aluminum by friction stir welding in concert with post-weld superplastic forming, *Scripta Mater.* **47**, 631–636 (2002).
29. D. G. Sanders, M. Ramulu, E. J. K. McCook, P. D. Edwards, A. P. Reynolds, and T. Trapp, Characterization of superplastically formed friction stir weld in titanium 6Al-4V: Preliminary results, *J. Mater. Eng. Perform.* **17**, 187–192 (2008).
30. D. G. Sanders, M. Ramulu, P. D. Edwards, and A. Cantrell, *J. Mater. Eng. Perform.* **19**, 503–509 (2010).
31. C. G. Rhodes, M. W. Mahoney, W. H. Bingel, R. A. Spurling, and C. C. Bampton, Effects on the surface texture, superplastic forming, and fatigue performance of titanium 6Al-4V friction stir welds, *Scripta Mater.* **36**, 69–75 (1997).
32. M. W. Mahoney, C. G. Rhodes, J. G. Flintoff, R. A. Spurling, and W. H. Bingel, Properties of friction-stir-welded 7075 T651 aluminum, *Metall. Mater. Trans. A* **29A**, 1955–1964 (1998).
33. L. E. Murr, G. Liu, and J. C. McClure, A TEM study of precipitation and related microstructures in friction-stir-welded 6061 aluminium, *J. Mater. Sci.* **33**, 1243–1251 (1998).
34. Y. S. Sato, H. Kokawa, M. Enomoto, and S. Jogan, Microstructural evolution of 6063 aluminum during friction-stir welding, *Metall. Mater. Trans. A* **30A**, 2429–2437 (1999).
35. K. V. Jata and S. L. Semiatin, Continuous dynamic recrystallization during friction stir welding of high strength aluminum alloys, *Scripta Mater.* **43**, 743–749 (2000).
36. K. V. Jata, K. K. Sankaran, and J. J. Ruschau, Friction-stir welding effects on microstructure and fatigue of aluminum alloy 7050-T7451, *Metall. Mater. Trans. A* **31A**, 2181–2192 (2000).
37. O. Frigaard, O. Grong, and O. T. Midling, A process model for friction stir welding of age hardening aluminum alloys, *Metall. Mater. Trans. A* **32A**, 1189–1200 (2001).
38. Y. S. Sato and H. Kokawa, Distribution of tensile property and microstructure in friction stir weld of 6063 aluminum, *Metall. Mater. Trans. A* **32A**, 3023–3031 (2001).
39. Y. S. Sato, H. Kokawa, K. Ikeda, M. Enomoto, S. Jogan, and T. Hashimoto, Microtexture in the friction-stir weld of an aluminum alloy, *Metall. Mater. Trans. A* **32A**, 941–948 (2001).
40. Y. S. Sato, S. H. C. Park, and H. Kokawa, Microstructural factors governing hardness in friction-stir welds of solid-solution-hardened Al alloys, *Metall. Mater. Trans. A* **32A**, 3033–3042 (2001).
41. Z. Y. Ma, R. S. Mishra, and M. W. Mahoney, Superplastic deformation behaviour of friction stir processed 7075 Al alloy, *Acta Mater.* **50**, 4419–4430 (2002).
42. J. Q. Su, T. W. Nelson, R. Mishra, and M. Mahoney, Microstructural investigation of friction stir welded 7050-T651 aluminium, *Acta Mater.* **51**, 713–729 (2003).
43. I. Charit and R. S. Mishra, High strain rate superplasticity in a commercial 2024 Al alloy via friction stir processing, *Mater. Eng. A* **359**, 290–296 (2003).
44. K. A. A. Hassan, A. F. Norman, D. A. Price, and P. B. Prangnell, Stability of nugget zone grain structures in high strength Al-alloy friction stir welds during solution treatment, *Acta Mater.* **51**, 1923–1936 (2003).
45. M. N. James, D. J. Hughes, D. G. Hattingh, G. R. Bradley, G. Mills, and P. J. Webster, Synchrotron diffraction measurement of residual stresses in friction stir welded 5383-H321 aluminium butt joints and their modification by fatigue cycling, *Fatigue Fract. Eng. Mater. Struct.* **27**, 187–202 (2004).
46. I. Charit and R. S. Mishra, Low temperature superplasticity in a friction-stir-processed ultrafine grained Al-Zn-Mg-Sc alloy, *Acta Mater.* **53**, 4211–4223 (2005).

47. C. Z. Zhou, X. Q. Yang, and G. H. Luan, Fatigue properties of friction stir welds in Al 5083 alloy, *Scripta Mater.* **53**, 1187–1191 (2005).
48. M. Mochizuki, M. Inuzuka, H. Nishida, K. Nakata, and M. Toyoda, Fracture toughness of structural aluminium alloy thick plate joints by friction stir welding, *Sci. Technol. Weld. Join.* **11**, 366–370 (2006).
49. S. W. Xu and X. M. Deng, A study of texture patterns in friction stir welds, *Acta Mater.* **56**, 1326–1341 (2008).
50. A. H. Feng, D. L. Chen, and Z. Y. Ma, Effect of welding parameters on microstructure and tensile properties of friction stir welded 6061 Al joints, *Mater. Sci. Forum* **618–619**, 41–44 (2009).
51. A. H. Feng, D. L. Chen, and Z. Y. Ma, Microstructure and cyclic deformation behavior of a friction-stir-welded 7075 Al alloy, *Metall. Mater. Trans. A* **41A**, 957–971 (2010).
52. K. Chen, W. Gan, K. Okamoto, K. Chung, and R. H. Wagoner, The mechanism of grain coarsening in friction-stir-welded AA5083 after heat treatment, *Metall. Mater. Trans. A* **42A**, 488–507 (2011).
53. J. D. Costa, J. A. M. Ferreira, L. P. Borrego, and L. P. Abreu, Fatigue behaviour of AA6082 friction stir welds under variable loadings, *Int. J. Fatigue* **37**, 8–16 (2012).
54. P. Dong, D. Q. Sun, and H. M. Li, Natural aging behaviour of friction stir welded 6005A-T6 aluminium alloy, *Mater. Sci. Eng. A* **576**, 29–35 (2013).
55. M. B. Hariri, S. G. Shiri, Y. Yaghoubinezhad, and M. M. Rahvard, The optimum combination of tool rotation rate and traveling speed for obtaining the preferable corrosion behavior and mechanical properties of friction stir welded AA5052 aluminum alloy, *Mater. Des.* **50**, 620–634 (2013).
56. Z. Zhang, B. L. Xiao, and Z. Y. Ma, Hardness recovery mechanism in the heat-affected zone during long-term natural aging and its influence on the mechanical properties and fracture behavior of friction stir welded 2024Al–T351 joints, *Acta Mater.* **73**, 227–239 (2014).
57. Z. H. Zhang, W. Y. Z. Li, Y. X. Feng, J. L. Li, and Y. J. Chao, Global anisotropic response of friction stir welded 2024 aluminum sheets, *Acta Mater.* **92**, 117–125 (2015).
58. N. Guo, Y. L. Fu, Y. L. Wang, Q. Meng, and Y. Zhu, Microstructure and mechanical properties in friction stir welded 5A06 aluminum alloy thick plate, *Mater. Des.* **113**, 273–283 (2017).
59. E. Cerri and P. Leo, Aging of medium strength aluminum alloy friction stir welds produced by different process parameter after tensile strain hardening, *Mater. Chem. Phys.* **147**, 1123–1133 (2014).
60. H. S. Park, T. Kimura, T. Murakami, Y. Nagano, K. Nakata, and M. Ushio, Microstructures and mechanical properties of friction stir welds of 60% Cu-40% Zn copper alloy, *Mater. Sci. Eng. A* **A371**, 160–169 (2004).
61. W. B. Lee and S. B. Jung, The joint properties of copper by friction stir welding, *Mater. Lett.* **58**, 1041–1046 (2004).
62. G. M. Xie, Z. Y. Ma, and L. Geng, Development of a fine-grained microstructure and the properties of a nugget zone in friction stir welded pure copper, *Scripta Mater.* **57**, 73–76 (2007).
63. G. M. Xie, Z. Y. Ma, and L. Geng, Partial recrystallizatioin in the nugget zone of friction stir welded dual-phase Cu-Zn alloy, *Philos. Mag.* **89**, 1505–1516 (2009).
64. Y. F. Sun and H. Fujii, Investigation of the welding parameter dependent microstructure and mechanical properties of friction stir welded pure copper, *Mater. Sci. Eng. A* **527**, 6879–6886 (2010).
65. P. Xue, G. M. Xie, B. L. Xiao, Z. Y. Ma, and L. Geng, Effect of heat input conditions on microstructure and mechanical properties of friction-stir-welded pure copper, *Metall. Mater. Trans. A* **41A**, 2010–2021 (2010).
66. P. Xue, B. L. Xiao, Q. Zhang, and Z. Y. Ma, Achieving friction stir welded pure copper joints with nearly equal strength to the parent metal via additional rapid cooling, *Scripta Mater.* **64**, 1051–1054 (2011).
67. J. Teimournezhad and A. Masoumi, Experimental investigation of onion ring structure formation in friction stir butt welds of copper plates produced by non-threaded tool pin, *Sci. Technol. Weld. Join.* **15**, 166–170 (2010).
68. H. Khodaverdizadeh, A. Mahmoudi, A. Heidarzadeh, and E. Nazari, Effect of friction stir welding (FSW) parameters on strain hardening behavior of pure copper joints, *Mater. Des.* **35**, 330–334 (2012).
69. H. Pashazadeh, A. Masoumi, and J. Teimournezhad, Numerical modelling for the hardness evaluation of friction stir welded copper metals, *Mater. Des.* **49**, 913–921 (2013).
70. P. Xue, B. L. Xiao, and Z. Y. Ma, High tensile ductility via enhanced strain hardening in ultrafine-grained Cu, *Mater. Sci. Eng. A* **532**, 106–110 (2012).
71. P. Xue, B. L. Xiao, and Z. Y. Ma, Achieving large-area bulk ultrafine grained Cu via submerged multiple-pass friction stir pocessing, *J. Mater. Sci. Technol.* **29**, 1111–1115 (2013).
72. S. H. C. Park, Y. S. Sato, and H. Kokawa, Microstructural evolution and its effect on Hall-Petch relationship in friction stir welding of thixomolded Mg alloy AZ91D, *J. Mater. Sci.* **38**, 4379–4383 (2003).
73. S. H. C. Park, Y. S. Sato, and H. Kokawa, Basal plane texture and flow pattern in friction stir weld of a magnesium alloy, *Metall. Mater. Trans. A* **34A**, 987–994 (2003).
74. C. I. Chang, C. J. Lee, and J. C. Huang, Relationship between grain size and Zener-Holloman parameter during friction stir processing in AZ31 Mg alloys, *Scripta Mater.* **51**, 509–514 (2004).
75. Y. N. Wang, C. I. Chang, C. J. Lee, H. K. Lin, and J. C. Huang, Texture and weak grain size dependence in friction stir processed Mg-Al-Zn alloy, *Scripta Mater.* **55**, 637–640 (2006).
76. W. Woo, H. Choo, D. W. Brown, P. K. Liaw, and Z. Feng, Texture variation and its influence on the tensile behavior of a friction-stir processed magnesium alloy, *Scripta Mater.* **54**, 1859–1864 (2006).
77. C. J. Lee, J. C. Huang, and X. H. Du, Improvement of yield stress of friction-stirred Mg-Al-Zn alloys by subsequent compression, *Scripta Mater.* **56**, 875–878 (2007).
78. S. Mironov, Y. Motohashi, and R. Kaibyshev, Grain growth behaviors in a friction-stir welded ZK60 magnesium alloy, *Mater. Trans.* 1387–1395 (2007).
79. C. I. Chang, X. H. Du, and J. C. Huang, Achieving ultrafine grain size in Mg-Al-Zn alloy by friction stir processing, *Scripta Mater.* **57**, 209–212 (2007).
80. G. M. Xie, Z. Y. Ma, L. Geng, and R. S. Chen, Microstructural evolution and mechanical properties of friction stir

welded Mg-Zn-Y-Zr alloy, *Mater. Sci. Eng. A* **471**, 63–68 (2007).

81. N. Afrin, D. L. Chen, X. Cao, and M. Jahazi, Strain hardening behavior of a friction stir welded magnesium alloy, *Scripta Mater.* **57**, 1004–1007 (2007).
82. G. M. Xie, Z. Y. Ma, L. Geng, and R. S. Chen, Microstructural evolution and enhanced superplasticity in friction stir processed Mg-Zn-Y-Zr alloy, *J. Mater. Res.* **23**, 1207–1213 (2008).
83. N. Afrin, D. L. Chen, X. Cao, and M. Jahazi, Microstructure and tensile properties of friction stir welded AZ31B magnesium alloy, *Mater. Sci. Eng. A* **472**, 179–186 (2008).
84. G. M. Xie, Z. Y. Ma, and L. Geng, Effect of microstructural evolution on mechanical properties of friction stir welded ZK60 alloy, *Mater. Sci. Eng. A* **486**, 49–55 (2008).
85. L. Commin, M. Dumont, J. E. Masse, and L. Barrallier, Friction stir welding of AZ31 magnesium alloy rolled sheets: Influence of processing parameters, *Acta Mater.* **57**, 326–334 (2009).
86. A. H. Feng and Z. Y. Ma, Microstructural evolution of cast Mg-Al-Zn during friction stir processing and subsequent aging, *Acta Mater.* **57**, 4248–4260 (2009).
87. A. H. Feng, B. L. Xiao, Z. Y. Ma, and R. S. Chen, Effect of friction stir processing procedures on microstructure and mechanical properties of Mg-Al-Zn casting, *Metall. Mater. Trans. A* **40A**, 2447–2456 (2009).
88. U. F. H. R. Suhuddin, S. Mironov, Y. S. Sato, H. Kokawa, and C. W. Lee, Grain structure evolution during friction-stir welding of AZ31 magnesium alloy, *Acta Mater.* **57**, 5406–5418 (2009).
89. G. M. Xie, Z. Y. Ma, and L. Geng, Effect of Y addition on microstructure and mechanical properties of friction stir welded ZK60 alloy, *J. Mater. Sci. Technol.* **25**, 351–355 (2009).
90. D. R. Ni, D. Wang, A. H. Feng, G. Yao, and Z. Y. Ma, Enhancing the high-cycle fatigue strength of Mg-9Al-1Zn casting by friction stir processing, *Scripta Mater.* **61**, 568–571 (2009).
91. S. M. Chowdhury, D. L. Chen, S. D. Bhole, X. Cao, E. Powidajko, D. C. Weckman, and Y. Zhou, Tensile properties and strain-hardening behavior of double-sided arc welded and friction stir welded AZ31B magnesium alloy, *Mater. Sci. Eng. A* **527**, 2951–2961 (2010).
92. X. J. Gu, C. Li, A. H. Feng, and D. L. Chen, Application of flat-clad optical fiber bragg crating sensor in characterization of asymmetric fatigue deformation of extruded magnesium alloy, *IEEE Sens. J.* **11**, 3042–3046 (2011).
93. K. N. Solanki, J. B. Jordon, W. Whittington, H. Rao, and C. R. Hubbard, Structure–property relationships and residual stress quantification of a friction stir spot welded magnesium alloy, *Scripta Mater.* **66**, 797–800 (2012).
94. Q. Yang, B. L. Xiao, and Z. Y. Ma, Influence of process parameters on microstructure and mechanical properties of friction-stir-processed Mg-Gd-Y-Zr Casting, *Metall. Mater. Trans. A* **43A**, 2094–2109 (2012).
95. Q. Yang, A. H. Feng, B. L. Xiao, and Z. Y. Ma, Influence of texture on superplastic behavior of friction stir processed ZK60 magnesium alloy, *Mater. Sci. Eng. A* **556**, 671–677 (2012).
96. H. S. Arora, H. Singh, and B. K. Dhindaw, Wear behaviour of a Mg alloy subjected to friction stir processing, *Wear* **303**, 65–77 (2013).
97. Q. Yang, B. L. Xiao, and Z. Y. Ma, Enhanced superplasticity in friction stir processed Mg-Gd-Y-Zr alloy, *J. Alloys Cmpnd.* **551**, 61–66 (2013).
98. F. Chai, D. T. Zhang, Y. Y. Li, and W. W. Zhang, High strain rate superplasticity of a fine-grained AZ91 magnesium alloy prepared by submerged friction stir processing, *Mater. Sci. Eng. A* **568**, 40–48 (2013).
99. J. Yang, D. R. Ni, D. Wang, B. L. Xiao, and Z. Y. Ma, Friction stir welding of as-extruded Mg-Al-Zn alloy with higher Al content. Part I: Formation of banded and line structures, *Mater. Character.* **96**, 142–150 (2014).
100. J. Yang, D. R. Ni, D. Wang, B. L. Xiao, and Z. Y. Ma, Friction stir welding of as-extruded Mg-Al-Zn alloy with higher Al content. Part II: Influence of precipitates, *Mater. Character.* **96**, 135–141 (2014).
101. P. Carlone and G. S. Palazzo, Characterization of TIG and FSW weldings in cast ZE41A magnesium alloy, *J, Mater, Process, Technol* **215**, 87–94 (2015).
102. A. Tripathi, A. Tewari, N. Srinivasan, G. M. Reddy, S. M. Zhu, J. F. Nie, R. D. Doherty, and I. Samajdar, Microstructural origin of friction sir processed zone in a magnesium alloy, *Metall. Mater. Trans. A* **46A**, 3333–3336 (2015).
103. Z. Liu, R. L. Xin, D. R. Li, L. Y. Sun, and Q. Liu, Comparative study on twinning characteristics during two post-weld compression paths and their effects on joint enhancement, *Sci. Rep.* **6**, 39779 (2016).
104. A. P. Reynolds, E. Hood, and W. Tang, Texture in friction stir welds of Timetal 21S, *Scripta Mater.* **52**, 491–494 (2005).
105. A. L. Pilchak, D. M. Norfleet, M. C. Juhas, and J. C. Williams, Friction stir processing of investment-cast Ti-6Al-4V: Microstructure and properties, *Metall. Mater. Trans. A* **39A**, 1519–1524 (2008).
106. S. Mironov, Y. Zhang, Y. S. Sato, and H. Kokawa, Crystallography of transformed β microstructure in friction stir welded Ti-6Al-4V alloy, *Scripta Mater.* **59**, 511–514 (2008).
107. S. Mironov, Y. Zhang, Y. S. Sato, and H. Kokawa, Development of grain structure in β-phase field during friction stir welding of Ti-6Al-4V alloy, *Scripta Mater.* **59**, 27–30 (2008).
108. J. Romero, M. M. Attallah, M. Preuss, M. Karadge, and S. E. Bray, Effect of the forging pressure on the microstructure and residual stress development in Ti-6Al-4V linear friction welds, *Acta Mater.* **57**, 5582–5592 (2009).
109. L. Zhou, H. J. Liu, P. Liu, and Q. W. Liu, The stir zone microstructure and its formation mechanism in Ti-6Al-4V friction stir welds, *Scripta Mater.* **61**, 596–599 (2009).
110. S. Mironov, Y. S. Sato, and H. Kokawa, Development of grain structure during friction stir welding of pure titanium, *Acta Mater.* **57**, 4519–4528 (2009).
111. R. W. Fonda and K. E. Knipling, Texture development in near-α Ti friction stir welds, *Acta Mater.* **58**, 6452–6463 (2010).
112. H. J. Liu, L. Zhou, and Q. W. Liu, Microstructural characteristics and mechanical properties of friction stir welded joints of Ti-6Al-4V titanium alloy, *Mater. Des.* **31**, 1650–1655 (2010).
113. A. L. Pilchak, W. Tang, H. Sahiner, A. P. Reynolds, and J. C. Williams, Microstructure evolution during friction stir welding of mill-annealed Ti-6Al-4V, *Metall. Mater. Trans. A* **42A**, 745–762 (2011).

114. A. L. Pilchak and J. C. Williams, Microstructure and texture evolution during friction stir processing of fully lamellar Ti-6Al-4V, *Metall. Mater. Trans. A* **42A**, 773–794 (2011).
115. S. Nimer, J. Wolk, and M. Zupan, Local property characterization of friction stir welded Ti-5111: Transverse orientation measurements, *Acta Mater.* **61**, 3050–3059 (2013).
116. J. Q. Su, J. Y. Wang, R. S. Mishra, R. Xu, and J. A. Baumann, Microstructure and mechanical properties of a friction stir processed Ti-6Al-4V alloy, *Mater. Sci. Eng. A* **573**, 67–74 (2013).
117. L. H. Wu, D. Wang, B. L. Xiao, and Z. Y. Ma, Microstructural evolution of the thermomechanically affected zone in a Ti-6Al-4V friction stir welded joint, *Scripta Mater.* **78–79**, 17–20 (2014).
118. L. H. Wu, B. L. Xiao, D. R. Ni, Z. Y. Ma, X. H. Li, M. J. Fu, and Y. S. Zeng, Achieving superior superplasticity from lamellar microstructure of a nugget in a friction-stir-welded Ti-6Al-4V joint, *Scripta Mater.* **98**, 44–47 (2015).
119. L. H. Wu, P. Xue, B. L. Xiao, and Z. Y. Ma, Achieving superior low-temperature superplasticity for lamellar microstructure in nugget of a friction stir welded Ti-6Al-4V joint, *Scripta Mater.* **122**, 26–30 (2016).
120. A. P. Reynolds, W. Tang, T. G. Herold, and H. Prask, Structure, properties, and residual stress of 304L stainless steel friction stir welds, *Scripta Mater.* **48**, 1289–1294 (2003).
121. Y. S. Sato, T. W. Nelson, and C. J. Sterling, Recrystallization in type 304L stainless steel during friction stirring, *Acta Mater.* **53**, 637–645 (2005).
122. L. Cui, H. Fujii, N. Tsuji, and K. Nogi, Friction stir welding of a high carbon steel, *Scripta Mater.* **56**, 637–640 (2007).
123. Y. Hovanski, M. L. Santella, and G. J. Grant, Friction stir spot welding of hot-stamped boron steel, *Scripta Mater.* **57**, 873–876 (2007).
124. R. Nandan, G. G. Roy, T. J. Lienert, and T. Debroy, Three-dimensional heat and material flow during friction stir welding of mild steel, *Acta Mater.* **55**, 883–895 (2007).
125. S. H. C. Park, Y. S. Sato, H. Kokawa, K. Okamoto, S. Hirano, and M. Inagaki, Boride formation induced by pcBN tool wear in friction-stir-welded strainless steels, *Metall. Mater. Trans. A* **40A**, 625–636 (2009).
126. Y. D. Chung, H. Fujii, R. Ueji, and N. Tsuji, Friction stir welding of high carbon steel with excellent toughness and ductility, *Scripta Mater.* **63**, 223–226.
127. R. Ramesh, I. Dinaharan, R. Kumar, and E. T. Akinlabi, Microstructure and mechanical characterization of friction stir welded high strength low alloy steels, *Mater Sci Eng A*, **687**, 39–46 (2017).
128. A. Steuwer, S. J. Barnes, J. Altenkirch, R. Johnson, and P. J. Withers, Friction stir welding of HSL-65 steel: part 2. The influence of weld speed and tool material on the residual stress distribution and tool wear, *Metall. Mater. Trans. A* **43A**, 2356–2365 (2012).
129. V. Manvatkar, A. De, L. E. Svensson, and T. DebRoy, Cooling rates and peak temperatures during friction stir welding of a high-carbon steel, *Scripta Mater.* **94**, 36–39 (2015).
130. P. Xue, B. L. Xiao, W. G. Wang, Q. Zhang, D. Wang, Q. Z. Wang, and Z. Y. Ma, Achieving ultrafine dual-phase structure with superior mechanical property in friction stir processed plain low carbon steel, *Mater. Sci. Eng. A* **575**, 30–34 (2013).
131. S. Karami, H. Jafarian, A. R. Eivani, and S. Kheirandish, Engineering tensile properties by controlling welding parameters and microstructure in a mild steel processed by friction stir welding, *Mater. Sci. Eng. A* **670**, 68–74 (2016).
132. H. B. Cui, G. M. Xie, Z. A. Luo, J. Ma, G. D. Wang, and R. D. K. Misra, The microstructural evolution and impact toughness of nugget zone in friction stir welded X100 pipeline steel, *J. Alloys Cmpnd.* **681**, 426–433 (2016).
133. P. Xue, Z. Y. Ma, Y. Komizo, and H. Fujii, Achieving ultrafine-grained ferrite structure in friction stir processed weld metal, *Mater. Lett.* **162**, 161–164 (2016).
134. O. M. Barabash, R. I. Barabash, G. E. Ice, Z. L. Feng, and D. Gandy, X-ray microdiffraction and EBSD study of FSP induced structural/phase transitions in a Ni-based superalloy, *Mater. Sci. Eng. A* **524**, 10–19 (2009).
135. D. R. Ni, P. Xue, D. Wang, B. L. Xiao, and Z. Y. Ma, Inhomogeneous microstructure and mechanical properties of friction stir processed NiAl bronze, *Mater. Sci. Eng. A* **524**, 119–128 (2009).
136. M. H. Mathon, V. Klosek, Y. d. Carlan, and L. Forest, Study of PM2000 microstructure evolution following FSW process, *J. Nucl. Mater.* **386–388**, 475–478 (2009).
137. S. S. Waminathan, K. O. Ishi, A. P. Zhilyaev, C. B. Fuller, B. London, and M. W. Mahoney, Peak stir zone temperatures during friction stir processing, *Metall. Mater. Trans. A* **41A**, 631–640 (2010).
138. K. H. Song and K. Nakata, Effect of precipitation on post-heat-treated Inconel 625 alloy after friction stir welding, *Mater. Des.* **31**, 2942–2947 (2010).
139. S. R. Nathan, S. Malarvizhi, V. Balasubramanian, and A. G. Rao, Failure analysis of tungsten based tool materials used in friction stir welding of high strength low alloy steels, *Eng. Fail. Anal.* **66**, 88–98 (2016).
140. P. Xue, B. L. Xiao, and Z. Y. Ma, Achieving ultrafine-grained structure in a pure nickel by friction stir processing with additional cooling, *Mater. Des.* **56**, 848–851 (2014).
141. P. B. Berbon, W. H. Bingel, R. S. Mishra, C. C. Bampton, and M. W. Mahoney, Friction stir processing: A tool to homogenize nanocomposite aluminum alloys, *Scripta Mater.* **44**, 61–66 (2001).
142. R. A. Prado, L. E. Murr, D. J. Shindo, and K. F. Soto, Tool wear in the friction-stir welding of aluminum alloy 6061 +20% Al2O3: A preliminary study, *Scripta Mater.* **45**, 75–80 (2001).
143. D. Storjohann, O. M. Barabash, S. S. Babu, S. A. David, P. S. Sklad, and E. E. Bloom, Fusion and friction stir welding of aluminum-metal-matrix composites, *Metall. Mater. Trans. A* **A36**, 3237–3247 (2005).
144. R. S. Mishra, Z. Y. Ma, and I. Charit, Friction stir processing: A novel technique for fabrication of surface composite, *Mater. Sci. Eng. A* **341** 307–310 (2003).
145. R. A. Prado, L. E. Murr, K. F. Soto, and J. C. McClure, Self-optimization in tool wear for friction-stir welding of Al 6061+20% Al2O3 MMC, *Mater. Sci. Eng. A* **A349**, 156–165 (2003).
146. C. J. Hsu, C. Y. Chang, P. W. Kao, N. J. Ho, and C. P. Chang, Al-Al3Ti nanocomposites produced in situ by

friction stir processing, *Acta Mater.* **54**, 5241–5249 (2006).

147. W. B. Lee, C. Y. Lee, M. K. Kim, J. I. Yoon, Y. J. Kim, Y. M. Yoen, and S. B. Jung, Microstructures and wear property of friction stir welded AZ91 Mg/SiC particle reinforced composite, *Compos. Sci. Tech.* **66**, 1513–1520 (2006).
148. L. M. Marzoli, A. V. Strombeck, J. F. D. Santos, C. Gambaro, and L. M. Volpone, Friction stir welding of an AA6061/Al_2O_3/20p reinforced alloy, *Compos. Sci. Tech.* **66**, 363–371 (2006).
149. Y. Morisada, H. Fujii, T. Nagaoka, and M. Fukusumi, Nanocrystallized magnesium alloy - uniform dispersion of C60 molecules, *Scripta Mater.* **55**, 1067–1070 (2006).
150. L. Ceschini, I. Boromei, G. Minak, A. Morri, and F. Tarterini, Microstructure, tensile and fatigue properties of AA6061/20 vol.%Al_2O_3p friction stir welded joints, *Compos. Part A* **38**, 1200–1210 (2007).
151. A. H. Feng, Z. Y. Ma, Formation of Cu2FeAl7 phase in friction-stir-welded SiCp/Al-Cu-Mg composite, *Scripta Mater.* **57**, 1113–1 and16 (2007).
152. A. H. Feng, B. L. Xiao, and Z. Y. Ma, Effect of microstructural evolution on mechanical properties of friction stir welded AA2009/SiCp composite, *Compos. Sci. Tech.* **68**, 2141–2148 (2008).
153. A. H. Feng, B. L. Xiao, and Z. Y. Ma, Grain boundary misorientation and texture development in friction stir welded SiCp/Al-Cu-Mg composite, *Mater. Sci. Eng. A* **497**, 515–518 (2008).
154. J. M. Root, D. P. Field, and T. W. Nelson, Crystallographic texture in the friction-stir-welded metal matrix composite Al6061 with 10 vol pct Al_2O_3, *Metall. Mater. Trans. A* **40A**, 2109–2114 (2009).
155. Z. Y. Liu, B. L. Xiao, W. G. Wang, and Z. Y. Ma, Singly dispersed carbon nanotube/aluminum composites fabricated by powder metallurgy combined with friction stir processing, *Carbon* **50**, 1843–1852 (2012).
156. Q. Zhang, B. L. Xiao, W. G. Wang, and Z. Y. Ma, Reactive mechanism and mechanical properties of in situ composites fabricated from an Al-TiO2 system by friction stir processing, *Acta Mater.* **60**, 7090–7103 (2012).
157. Q. Zhang, B. L. Xiao, P. Xue, and Z. Y. Ma, Microstructural evolution and mechanical properties of ultrafine grained Al_3Ti/Al-5.5Cu composites produced via hot pressing and subsequent friction stir processing, *Mater. Chem. Phys.* **134**, 294–301 (2012).
158. D. Wang, Q. Z. Wang, B. L. Xiao, and Z. Y. Ma, Achieving friction stir welded SiCp/Al-Cu-Mg composite joint of nearly equal strength to base material at high welding speed, *Mater. Sci. Eng. A* **589**, 271–274 (2014).
159. X. X. Zhang, D. R. Ni, B. L. Xiao, H. Andrä, W. M. Gan, M. Hofmann, and Z. Y. Ma, Determination of macroscopic and microscopic residual stresses in friction stir welded metal matrix composites via neutron diffraction, *Acta Mater.* **87**, 161–173 (2015).
160. W. B. Lee, Y. M. Yeon, and S. B. Jung, The joint properties of dissimilar formed Al alloys by friction stir welding according to the fixed location of materials, *Scripta Mater.* **49**, 423–428 (2003).
161. Y. S. Sato, S. H. C. Park, M. Michiuchi, and H. Kokawa, Constitutional liquation during dissimilar friction stir welding of Al and Mg alloys, *Scripta Mater.* **50**, 1233–1236 (2004).
162. H. Uzun, C. D. Donne, A. Argagnotto, T. Ghidini, and C. Gambaro, Friction stir welding of dissimilar Al 6013-T4 To X5CrNi18-10 stainless steel, *Mater. Des.* **26**, 41–46 (2005).
163. M. B. Prime, T. G. Herold, J. A. Baumann, R. J. Lederich, D. M. Bowden, and R. J. Sebring, Residual stress measurements in a thick, dissimilar aluminum alloy friction stir weld, *Acta Mater.* **54**, 4013–4021 (2006).
164. Y. Li, E. A. Trillo, and L. E. Murr, Friction-stir welding of aluminum alloy 2024 to silver, *J. Mater. Sci. Lett.* **19**, 1047–1051 (2000).
165. J. Ouyang, E. Yarrapareddy, and R. Kovacevic, Microstructural evolution in the friction stir welded 6061 aluminum alloy (T6-temper condition) to copper, *J. Mater. Process. Technol.* **172**, 110–122 (2006).
166. C. Liu, D. L. Chen, S. Bhole, X. Cao, and M. Jahazi, Polishing-assisted galvanic corrosion in the dissimilar friction stir welded joint of AZ31 magnesium alloy to 2024 aluminum alloy, *Mater. Character.* **60**, 370–376 (2009).
167. P. Xue, D. R. Ni, D. Wang, B. L. Xiao, and Z. Y. Ma, Effect of friction stir welding parameters on the microstructure and mechanical properties of the dissimilar Al-Cu joints, *Mater. Sci. Eng. A* **528**, 4683–4689 (2011).
168. I. Galvão, J. C. Oliveira, A. Loureiro, and D. M. Rodrigues, Formation and distribution of brittle structures in friction stir welding of aluminium and copper: Influence of shoulder geometry, *Intermetallics* **22**, 122–128.
169. M. Jafarzadegan, A. H. Feng, T. Saeid, J. Shen, and H. Assadi, Microstructural characterization in dissimilar friction stir welding between 304 stainless steel and st37 steel, *Mater. Character.* **74**, 28–41 (2012).
170. M. Jafarzadegan, A. A. Zadeh, A. H. Feng, T. Saeid, J. Shen, and H. Assadi, Microstructure and mechanical properties of a dissimilar friction stir weld between austenitic stainless steel and low carbon steel, *J. Mater. Sci. Technol.* **29**, 367–372 (2013).
171. W. Han, D. S. Chen, Y. Ha, A. Kimura, H. Serizawa, H. Fujii, and Y. Morisada, Modifications of grain-boundary structure by friction stir welding in the joint of nanostructured oxide dispersion strengthened ferritic steel and reduced activation martensitic steel, *Scripta Mater.* **105**, 2–5 (2015).
172. D. Wang, B. L. Xiao, Z. Y. Ma, and H. F. Zhang, Friction stir welding of Zr55Cu30Al10Ni5 bulk metallic glass to Al-Zn-Mg-Cu alloy, *Scripta Mater.* **60**, 112–115 (2009).
173. Y. F. Sun, Y. S. Ji, H. Fujii, K. Nakata, and K. Nogi, Microstructure and mechanical properties of friction stir welded joint of $Zr_{55}Cu_{30}Al_{10}$Ni5 bulk metallic glass with pure copper, *Mater. Sci. Eng. A* **527**, 3427–3432 (2010).
174. B. Heinz and B. Skrotzki, Characterization of a friction-stir-welded aluminum alloy 6013, *Metall. Mater. Trans. A* **33B**, 489–498 (2002).
175. F. C. Liu and Z. Y. Ma, Influence of tool dimension and welding parameters on microstructure and mechanical properties of friction-stir-welded 6061-T651 aluminum alloy, *Metall. Mater. Trans. A* **39A**, 2378–2388 (2008).
176. Y. Tao, Z. Zhang, D. R. Ni, D. Wang, B. L. Xiao, and Z. Y. Ma, Influence of welding parameter on mechanical properties and fracture behavior of friction stir welded Al-Mg-Sc joints, *Mater. Sci. Eng. A* **612**, 236–245 (2014).
177. W. M. Thomas, K. I. Johnson, and C. S. Wiesner, Friction stir welding-recent developments in tool and process technologies, *Adv. Eng. Mater.* **5**, 485–490 (2003).

178. Y. H. Zhao, S. B. Lin, L. Wu, and F. X. Qu, The influence of pin geometry on bonding and mechanical properties in friction stir weld 2014 Al alloy, *Mater. Lett.* **59**, 2948–2952 (2005).
179. H. Fujii, L. Cui, M. Maeda, and K. Nogi, Effect of tool shape on mechanical properties and microstructure of friction stir welded aluminum alloys, *Mater. Sci. Eng. A* **A419**, 25–31 (2006).
180. A. Arora, A. De, and T. DebRoy, Toward optimum friction stir welding tool shoulder diameter, *Scripta Mater.* **64**, 9–12 (2011).
181. A. F. Hasan, C. J. Bennett, and P. H. Shipway, A numerical comparison of the flow behaviour in friction stir welding (FSW) using unworn and worn tool geometries, *Mater. Des.* **87**, 1037–1046 (2015).
182. N. Martinez, N. Kumar, R. S. Mishra, and K. J. Doherty, Effect of tool dimensions and parameters on the microstructure of friction stir welded aluminum 7449 alloy of various thicknesses, *Mater. Sci. Eng. A* **684**. 470–479 (2017).
183. H. N. B. Schmidt, T. L. Dickerson, and J. H. Hattel, Material flow in butt friction stir welds in AA2024-T3, *Acta Mater.* **54**, 1199–1209 (2006).
184. L. Fratini, G. Buffa, D. Palmeri, J. Hua, and R. Shivpuri, Material flow in FSW of AA7075-T6 butt joints numerical simulations and experimental verifications, *Sci. Technol. Weld. Join.* **11**, 412–421 (2006).
185. Y. H. Zhao, S. B. Lin, F. X. Qu, and L. Wu, Influence of pin geometry on material flow in friction stir welding process, *Mater. Sci. Technol.* **22**, 45–60 (2006).
186. A. Simar, T. Pardoen, and B. d. Meester, Effect of rotational material flow on temperature distribution in friction stir welds, *Sci. Technol. Weld. Join.* **12**, 324–333 (2007).
187. Z. Zhang, B. L. Xiao, D. Wang, and Z. Y. Ma, Effect of alclad Layer on material flow and defect formation in friction-stir-welded 2024 aluminum alloy, *Metall. Mater. Trans. A* **42A**, 1717–1726 (2011).
188. M. N. A. Fenoel, R. Tailiard, J. Laye, and T. Odievre, Experimental investigation of three-dimensional (3-D) material flow pattern in thick dissimilar 2050 friction-stir welds, *Metall. Mater. Trans. A* **45A**, 563–578 (2014).
189. X. C. Liu, C. S. Wu, and G. K. Padhy, Characterization of plastic deformation and material flow in ultrasonic vibration enhanced friction stir welding, *Scripta Mater.* **102**, 95–98 (2015).
190. H. Schmidt, J. Hattel, and J. Wert, An analytical model for the heat generation in friction stir welding, *Model. Simul. Mater. Sci. Eng.* **12**, 143–157 (2004).
191. A. Gerlich, G. A. Cingara, and T. H. North, Stir zone microstructure and strain rate during Al 7075-T6 friction stir spot welding, *Metall. Mater. Trans. A* **37A**, 2773–2786 (2006).
192. A. Gerlich, M. Yamamoto, and T. H. North, Strain rates and grain growth in Al 5754 and Al 6061 friction stir spot welds, *Metall. Mater. Trans. A* **38A**, 1291–1302 (2007).
193. W. Woo, Z. Feng, X. L. Wang, D. W. Brown, B. Clausen, K. An, H. Choo, C. R. Hubbard, and S. A. David, In situ neutron diffraction measurements of temperature and stresses during friction stir welding of 6061-T6 aluminium alloy, *Sci. Technol. Weld. Join.* **12**, 298–303 (2007).
194. X. K. Zhu, Y. J. Chao, Numerical simulation of transient temperature and residual stresses in friction stir welding of 304L stainless steel, J Mater Process Technol, *Wear* **146**, 263–272 (2004).
195. P. Upadhyay and A. P. Reynolds, Effects of thermal boundary conditions in friction stir welded AA7050-T7 sheets, *Mater. Sci. Eng. A* **527**, 1537–1543 (2010).
196. M. J. Jones, P. Heurtier, C. Desrayaud, F. Montheillet, D. Allehaux, and J. H. Driver, Correlation between microstructure and microhardness in a friction stir welded 2024 aluminium alloy, *Scripta Mater.* **52**, 693–697 (2005).
197. R. W. Fonda, J. F. Bingert, and K. J. Colligan, Development of grain structure during friction stir welding, *Scripta Mater.* **51**, 243–248 (2004).
198. C. Genevois, A. Deschamps, A. Denquin, and B. D. Cottignies, Quantitative investigation of precipitation and mechanical behaviour for AA2024 friction stir welds, *Acta Mater.* **53**, 2447–2458 (2005).
199. W. Woo, T. Ungar, Z. Feng, E. Kenik, and B. Clausen, X-ray and neutron diffraction measurements of dislocation density and subgrain size in a friction-stir-welded aluminum alloy, *Metall. Mater. Trans. A* **41A**, 1210–1216 (2010).
200. P. B. Prangnell and C. P. Heason, Grain structure formation during friction stir welding observed by the ‘stop action technique’, *Acta Mater.* **53**, 3179–3192 (2005).
201. H. Chen, L. Fu, and P. Liang, Microstructure, texture and mechanical properties of friction stir welded butt joints of 2A97 Al-Li alloy ultra-thin sheets, *J. Alloys Cmpnd.* **692**, 155–169 (2017).
202. C. M. Chen and R. Kovacevic, Finite element modeling of friction stir welding-thermal and thermomechanical analysis, *Int. J. Mach. Tools Manuf.* **43**, 1319–1326 (2003).
203. R. John, K. V. Jata, and K. Sadananda, Residual stress effects on near-threshold fatigue crack growth in friction stir welds in aerospace alloys, *Int. J. Fatigue* **25**, 939–948 (2003).
204. P. Staron, M. Kocak, S. Williams, and A. Wescott, Residual stress in friction stir-welded Al sheets, *Physica* **B350**, e491–e493 (2004).
205. P. Staron, M. Kocak, and S. Williams, Residual stresses in friction stir welded Al sheets, *Appl. Phys. A* **74**, S1161–S1162 (2002).
206. G. Bussu and P. E. Irving, The role of residual stress and heat affected zone properties on fatigue crack propagation in friction stir welded 2024-T351 aluminium joints, *Int. J. Fatigue* **25**, 77–88 (2003).
207. S. Lomolino, R. Tovo, and J. Santos, On the fatigue behaviour and design curves of friction stir butt-welded Al alloys, *Int. J. Fatigue* **27**, 305–316 (2005).
208. Z. Y. Ma and R. S. Mishra, Cavitation in superplastic 7075Al alloys prepared via friction stir processing, *Acta Mater.* **51**, 3551–3569 (2003).
209. Z. Y. Ma and R. S. Mishra, Development of ultrafine-grained microstructure and low temperature (0.48Tm) superplasticity in friction stir processed Al-Mg-Zr, *Scripta Mater.* **53**, 75–80 (2005).
210. S. Lim, S. Kim, C. G. Lee, and S. J. Kim, Tensile behavior of friction-stri-welded Al 6061-T651, *Metall. Mater. Trans. A* **35A**, 2829–2835 (2004).

211. S. R. Sharma and R. S. Mishra, Fatigue crack growth behavior of friction stir processed aluminum alloy, *Scripta Mater.* **59**, 395–398 (2008).
212. A. H. Feng, D. L. Chen, and Z. Y. Ma, Microstructure and low cycle fatigue of a friction stir welded 6061 aluminum alloy, *Metall. Mater. Trans. A* **41A**, 2626–2641 (2010).
213. A. H. Feng, D. L. Chen, Z. Y. Ma, W. Y. Ma, and R. J. Song, Microstructure and strain hardening of a friction stir welded high-strength Al-Zn-Mg alloy, *Acta Metall. Sin. (Engl. Lett.)* **27**, 723–729 (2014).
214. A. Simar, Y. Brechet, B. Meester, A. Denquin, and T. Pardoen, Sequential modeling of local precipitation, strength and strain hardening in friction stir welds of an aluminum alloy 6005A-T6, *Acta Mater.* **55**, 6133–6143 (2007).
215. R. Z. Valiev, R. K. Islamgaliev, and I. V. Alexandrov, Bulk nanostructured materials from severe plastic deformation, *Prog. Mater. Sci.* **45**, 103–189 (2000).
216. Q. Wei, S. Cheng, K. T. Ramesh, and E. Ma, Effect of nanocrystalline and ultrafine grain sizes on the strain rate sensitivity and activation volume: Fcc versus bcc metals, *Mater. Sci. Eng. A* **381**, 71–79 (2004).
217. A. P. Zhilyaev and T. G. Langdon, Using high-pressure torsion for metal processing: Fundamentals and applications, *Prog. Mater. Sci.* **53**, 893–979 (2008).
218. R. Z. Valiev, N. A. Krasilnikov, and N. K. Tsenev, Plastic deformation of alloys with submicron-grained structure, *Mater. Sci. Eng. A* **137**, 35–40 (1991).
219. R. Z. Valiev and T. G. Langdon, Principles of equal-channel angular pressing as a processing tool for grain refinement, *Prog. Mater. Sci.* **51**, 881–981 (2006).
220. A. P. Zhilyaev, G. V. Nurislamova, B. K. Kim, M. D. Baro, J. A. Szpunar, and T. G. Langdon, Experimental parameters influencing grain refinement and microstructural evolution during high-pressure torsion, *Acta Mater.* **51**, 753–765 (2003).
221. G. A. Salishchev, R. M. Galeyev, S. P. Malysheva, and M. M. Myshlyaev, Structure and density of submicrocrystalline titanium produced by severe plastic deformation, *NanoStructured Mater.* **11**, 407–414 (1999).
222. M. Richert, Q. Liu, and N. Hansen, Microstructural evolution over a large strain range in aluminium deformed by cyclic-extrusion-compression, *Mater. Sci. Eng. A* **260**, 275–283 (1999).
223. Y. Saito, H. Utsunomiya, N. Tsuji, and T. Sakai, Novel ultra-high straining process for bulk materials–development of the accumulative roll-bonding (ARB) process, *Acta Mater.* **47**, 579–583 (1999).
224. S. H. Lee, Y. Saito, T. Sakai, and H. Utsunomiya, Microstructures and mechanical properties of 6061 aluminum alloy processed by accumulative roll-bonding, *Mater. Sci. Eng. A* **325**, 228–235 (2002).
225. J. Q. Su, T. W. Nelson, and C. J. Sterling, Grain refinement of aluinum alloys by friction stir processing, *Philos. Mag.* **86**, 1–24 (2006).
226. E. Hoyos, D. López, and H. Alvarez, A phenomenologically based material flow model for friction stir welding, *Mater. Des.* **111**, 321–330 (2016).
227. J. Schneider, R. Beshears, and A. C. Nunes, Interfacial sticking and slipping in the friction stir welding process, *Mater. Sci. Eng. A* **435–436**, 297–304 (2006).
228. B. C. Liechty and B. W. Webb, The use of plasticine as an analog to explore material flow in friction stir welding, *J. Mater. Process. Technol.* **184**, 240–250 (2007).
229. Y. Morisada, H. Fujii, Y. Kawahito, K. Nakata, and M. Tanaka, Three-dimensional visualization of material flow during friction stir welding by two pairs of X-ray transmission systems, *Scripta Mater.* **65**, 1085–1088.
230. W. F. Xu, J. H. Liu, and D. L. Chen, *J. Alloys Cmpnd.* **509**, 8449–8454 (2011).
231. Y. Li, L. E. Murr, and J. C. McClure, Solid-state flow visualization in the friction-stir welding of 2024 Al to 6061 Al, *Scripta Mater.* **40**, 1041–1046 (1999).
232. Y. X. Huang, Y. B. Wang, L. Wan, H. S. Liu, J. J. Shen, J. F. dos Santos, L. Zhou, and J. C. Feng, Material-flow behavior during friction-stir welding of 6082-T6 aluminum alloy, *Int. J. Adv. Manuf. Technol.* **87**, 1115–1123 (2016).
233. Y. Morisada, H. Fujii, T. Nagaoka, K. Nogi, and M. Fukusumi, Fullerene/A5083 composites fabricated by material flow during friction stir processing, *Compos. Part A* **38**, 2097–2101 (2007).
234. P. Ulysse, Three-dimensional modeling of the friction stir-welding process, *Int. J. Mach. Tools Manuf.* **42**, 1549–1557 (2002).
235. G. Buffa, J. Hua, R. Shivpuri, and L. Fratini, Design of the friction stir welding tool using the continuum based FEM model, *Mater Sci Eng A* 419:381–388, (2005).
236. H. Schmidt and J. Hattel, A local model for the thermomechanical conditions in friction stir welding, *Model. Simul. Mater. Sci. Eng.* **13**, 77–93 (2005).
237. A. Arora, Z. Zhang, A. De, and T. DebRoy, Strains and strain rates during friction stir welding, *Scripta Mater.* **61**, 863–866 (2009).
238. A. Arora, R. Nandan, A. P. Reynolds, and T. DebRoy, Torque, power requirement and stir zone geometry in friction stir welding through modeling and experiments, *Scripta Mater.* **60**, 13–16 (2009).
239. K. A. A. Hassan, B. P. Wynne, and P. B. Prangnell, The simulation of nugget zone grain structures in high strength Al-alloy friction stir welds by high strain torsion testing, *Fourth Int. Symp. FSW*, TWI, Park City (2003) (CD-ROM).
240. J. Q. Su, T. W. Nelson, and C. J. Sterling, Microstructure evolution during FSW/FSP of high strength aluminum alloys, *Mater. Sci. Eng. A* **405**, 277–286 (2005).
241. T. Morishige, T. Hirata, T. Uesugi, Y. Takigawa, M. Tsujikawa, and K. Higashi, Effect of Mg content on the minimum grain size of Al-Mg alloys obtained by friction stir processing, *Scripta Mater.* **64**, 355–358 (2011).
242. M. A. Sutton, B. Yang, A. P. Reynolds, and R. Taylor, Microstructural studies of friction stir welds in 2024-T3 aluminum, *Mater. Sci. Eng. A* **323**, 160–166 (2002).
243. Y. Morisada, T. Imaizumi, and H. Fujii, Determination of strain rate in friction stir welding by three-dimensional visualization of material flow using X-ray radiography, *Scripta Mater.* **106**, 57–60 (2015).
244. D. Yi, T. Onuma, S. Mironov, Y. S. Sato, and H. Kokawa, Evaluation of heat input during friction stir welding of aluminium alloys, *Sci. Technol. Weld. Join.* **22**, 41–46 (2017).
245. D. C. Hofmann and K. S. Vecchio, Thermal history analysis of friction stir processed and submerged friction stir

processed aluminum, *Mater. Sci. Eng. A* **465**, 165–175 (2007).

246. Effect of tool pin-tip profiles on material flow and mechanical properties of friction stir welding thick AA7075-T6 alloy joints, *Int. J. Adv. Manuf. Technol.* **88**, 949–960 (2017).
247. Y. Pan and D.A Lados, Friction stir welding in wrought and cast aluminum alloys: Heat transfer modeling and thermal history analysis, *Metall. Mater. Trans. A* **48A**, 722–734 (2017).
248. W. F. Xu, J. H. Liu, G. H. Luan, and C. L. Dong, Temperature evolution, microstructure and mechanical properties of friction stir welded thick 2219-O aluminum alloy joints, *Mater. Des.* **30**, 1886–1893 (2009).
249. J. Kang, Feng G. S., Frankel I. W., Huang, Wang, and Wu, Friction stir welding of Al alloy 2219-T8: Part I-Evolution of precipitates and formation of abnormal Al2Cu agglomerates, *Metall. Mater. Trans. A* **47A**, 4553–4565 (2016).
250. X. X. Zhang, B. L. Xiao, and Z. Y. Ma, A transient thermal model for friction stir weld. Part 1: The model, *Metall. Mater. Trans. A* **42A**, 3218–3228 (2011).
251. X. X. Zhang, B. L. Xiao, and Z. Y. Ma, A transient thermal model for friction stir weld. Part 2: Effects of weld conditions, *Metall. Mater. Trans. A* **42A**, 3229–3239 (2011).
252. M. Song and R. Kovacevic, Thermal modeling of friction stir welding in a moving cordinate system and its validation, *Int. J. Mach. Tools Manuf.* **43**, 605–615 (2003).
253. J. H. Yan, M. A. Sutton, and A. P. Reynolds, Process-structure-property relationships for nugget and heat affected zone regions of AA2524-T351 friction stir welds, *Sci. Technol. Weld. Join.* **10**, 725–736 (2005).
254. W. J. Arbegast and P. J. Hartley, Friction stir weld technology development at lockheed martin michoud space system-An overview, in: *Proc. Fifth Int. Conf. Trends Weld Res.*, Pine Mountain, GA, June 1–5, pp. 541–546 (1998).
255. W. Woo, Z. Feng, X. L. Wang, and C. R. Hubbard, Neutron diffraction measurements of time-dependent residual stresses generated by severe thermomechanical deformation, *Scripta Mater.* **61**, 624–627 (2009).
256. W. Woo, H. Choo, D. W. Brown, Z. Feng, and P. K. Liaw, Angular distortion and through-thickness residual stress distribution in the friction-stir processed 6061-T6 aluminum alloy, *Mater. Sci. Eng. A* **437**, 64–69 (2006).
257. L. Fratini and B. Zuccarello, An analysis of through-thickness residual stresses in aluminium FSW butt joints, *Int. J. Mach. Tools Manuf.* **46**, 611–619 (2006).
258. W. F. Xu, J. H. Liu, and H. Q. Zhu, Analysis of residual stresses in thick aluminum friction stir welded butt joints, *Mater. Des.* **32**, 2000–2005 (2011).
259. O. Hatamleh, I. V. Rivero, and A. Maredia, Residual stresses in friction-stir-welded 2195 and 7075 aluminum alloys, *Metall. Mater. Trans. A* **39A**, 2867–2874 (2008).
260. V. M. Linton and M. I. Ripley, Influence of time on residual stresses in friction stir welds in agehardenable 7xxx aluminium alloys, *Acta Mater.* **56**, 4319–4327 (2008).
261. W. Woo, H. Choo, M. B. Prime, Z. Feng, and B. Clausen, Microstructure, texture and residual stress in a friction-stir-processed AZ31B magnesium alloy, *Acta Mater.* **56**, 1701–1711 (2008).
262. M. Peel, A. Steuwer, M. Preuss, and P. J. Withers, Microstructure, mechanical properties and residual stresses as a function of welding speed in aluminium AA5083 friction stir welds, *Acta Mater.* **51**, 4791–4801 (2003).
263. A. Steuwer, M. J. Peel, and P. J. Withers, Dissimilar friction stir welds in AA5083-AA6082: The effect of process parameters on residual stress, *Mater. Sci. Eng. A* **441**, 187–196 (2006).
264. R. Brown, W. Tang, and A. P. Reynolds, Multi-pass friction stir welding in alloy 7050-T7451: Effects on weld response variables and on weld properties, *Mater. Sci. Eng. A* **513–514**, 115–121 (2009).
265. C. D. Donne, E. Lima, J. Wegener, A. Pyzalla, and T. Buslaps Investigations on Residual Stresses in Friction Stir Welds, in: Proceedings of the Third International Symposium on Friction Stir Welding, Kobe, Japan, September 27–28 (2001).
266. Z. Y. Ma, S. R. Sharma, and R. S. Mishra, Effect of multiple-pass friction stir processing on microstructure and tensile properties of a cast aluminum-silicon alloy, *Scripta Mater.* **54**, 1623–1626 (2006).
267. S. Meenia, F. Md, S. Babu, R. J. Immanuel, S. K. Panigrahi, and G. D. Ram, Particle refinement and fine-grain formation leading to enhanced mechanical behaviour in a hypo-eutectic Al–Si alloy subjected to multi-pass friction stir processing, *Mater. Character.* **113**, 134–143 (2016).
268. V. Firouzdor and S. Kou, Al-to-Mg friction stir welding: Effect of material position, travel speed, and rotation speed, *Metall. Mater. Trans. A* **41A**, 2914–2935 (2010).
269. M. P. Miles, D. W. Melton, and T. W. Nelson, Formability of friction-stir-welded dissimilar-aluminum-alloy sheets, *Metall. Mater. Trans. A* **36A**, 3335–3342 (2005).
270. S. A. Khodir and T. Shibayanagi, Friction stir welding of dissimilar AA2024 and AA7075 aluminum alloys, *Mater. Sci. Eng. B* **148**, 82–87 (2008).
271. M. Ghosh, K. Kumar, S. V. Kailas, and A. K. Ray, Optimization of friction stir welding parameters for dissimilar aluminum alloys, *Mater. Des.* **31**, 3033–3037 (2010).
272. A. Simar, C. Jonckheere, K. Deplus, T. Pardoen, and B. D. Meester, Comparing similar and dissimilar friction stir welds of 2017-6005A aluminium alloys, *Sci. Technol. Weld. Join.* **15**, 254–259 (2010).
273. V. Saravanan, S. Rajakumar, and A. Muruganandam, Effect of friction stir welding process parameters on microstructure and mechanical properties of dissimilar AA6061-T6 and AA7075-T6 aluminum alloy joints, *Metallogr. Microstruct. Anal.* **5**, 476–485 (2016).
274. V. Saravanan, S. Rajakumar, N. Banerjee, and R. Amuthakkannan, Effect of shoulder diameter to pin diameter ratio on microstructure and mechanical properties of dissimilar friction stir welded AA2024-T6 and AA7075-T6 aluminum alloy joints, *Int. J. Adv. Manuf. Technol.* **87**, 3637–3645 (2016).
275. Yan, Liu, and Fang, Fatigue behavior of dissimilar Al-Mg-Si/Al-Zn-Mg aluminum alloys friction stir welding joints, *Acta Metallurg. Sinica–Engl. Lett.* **29**, 1161–1168 (2016).

276. P. Mastanaiah, A. Sharma, and G. M. Reddy, Dissimilar friction stir welds in AA2219-AA5083 aluminium alloys: Effect of process parameters on material inter-mixing, defect formation, and mechanical properties, *Trans. Ind. Instit. Met.* **69**, 1397–1415 (2016).
277. M. Saeidi, B. Manafi, M. K. B. Givi, and G. Faraji, Mathematical modeling and optimization of friction stir welding process parameters in AA5083 and AA7075 aluminum alloy joints, *Proc. Instit. Mech. Eng. Part B–J. Eng. Manuf.* **230**, 1284–1294 (2016).
278. A. C. Somasekharan and L. E. Murr, Microstructures in friction-stir welded dissimilar magnesium alloys and magnesium alloys to 6061-T6 aluminum alloy, *Mater. Charcter.* **52**, 49–64 (2004).
279. J. C. Yan, Z. W. Xu, Z. Y. Li, L. Li, and S. Q. Yang, Microstructure characteristics and performance of dissimilar welds between magnesium alloy and aluminum formed by friction stirring, *Scripta Mater.* **53**, 585–589 (2005).
280. A. C. Somasekharan and L. E. Murr, Characterization of complex, solid-state flow and mixing in the friction-stir welding (FSW) of aluminum alloy 6061-T6 to magnesium alloy AZ91D using color metallography, *J. Mater. Sci.* **41**, 5365–5370 (2006).
281. M. E. A. Aleagha, B. Hadi, and M. A. Shahbazi, 3-dimensional numerical analysis of friction stir welding of copper and aluminum, *J. Mech. Sci. Technol.* **30**, 3767–3776 (2016).
282. M. Kimura, H. Ishii, M. Kusaka, K. Kaizu, and A. Fuji, Joining phenomena and joint strength of friction welded joint between aluminium-magnesium alloy (AA5052) and low carbon steel, *Sci. Technol. Weld. Join.* **14**, 655–661 (2009).
283. H. A. Derazkola, H. J. Aval, and M. Elyasi, Analysis of process parameters effects on dissimilar friction stir welding of AA1100 and A441 AISI steel, Sci Technol Weld Joining **20**, 553–562 (2015).
284. W. B. Lee, M. Schmuecker, U. A. Mercardo, G. Biallas, and S. B. Jung, Interfacial reaction in steel-aluminum joints made by friction stir welding, *Scripta Mater.* **55**, 355–358 (2006).
285. T. Tanaka, T. Morishige, and T. Hirata, Comprehensive analysis of joint strength for dissimilar friction stir welds of mild steel to aluminum alloys, *Scripta Mater.* **61**, 756–759 (2009).
286. S. Kundu, D. Roy, R. Bhola, D. Bhattacharjee, B. Mishra, and S. Chatterjee, Microstructure and tensile strength of friction stir welded joints between interstitial free steel and commercially pure aluminium, *Mater. Des.* **50**, 370–375 (2013).
287. M. Ghosh, R. K. Gupta, and M. M. Husain, Friction stir welding of stainless steel to Al alloy: Effect of thermal condition on weld nugget microstructure, *Metall. Mater. Trans. A* **45A**,854–863 (2014).
288. X. J. Fei, X. Z. Jin, N. X. Peng, Y. Ye, S. G. Wu, and H. F. Dai, Effect of filling material and laser power on the formation of intermetallic compounds during laser-assisted friction stir butt welding of steel and aluminum alloys, *Appl. Phys. A.* **122**, 936 (2016).
289. H. D. Naghibi, M. Shakeri, and M. Hosseinzadeh, Neural network and genetic algorithm based modeling and optimization of tensile properties in FSW of AA 5052 to AISI 304 dissimilar joints, *Trans. Ind. Instit. Met.* **69**, 891–900 (2016).
290. K. K. Ramachandran, N. Murugan, and S. S. Kumar, Performance analysis of dissimilar friction stir welded aluminium alloy AA5052 and HSLA steel butt joints using response surface method, *Int. J. Adv. Manuf. Technol.* **86**, 2373–2392 (2016).
291. A. Yazdipour and A. Heidarzadeh, Dissimilar butt friction stir welding of Al 5083-H321 and 316L stainless steel alloys, *Int. J. Adv. Manuf. Technol.* **87**, 3105–3112 (2016).
292. A. Yazdipour and A. Heidarzadeh, Effect of friction stir welding on microstructure and mechanical properties of dissimilar Al 5083-H321 and 316L stainless steel alloy joints, *J. Alloys Cmpnd.* **680**, 595–603 (2016).
293. K. S. Bang, K. J. Lee, Han Sur Bang, and Hee Sun Bang, Interfacial microstructure and mechanical properties of dissimilar friction stir welds between 6061-T6 aluminum and Ti-6%Al-4%V alloys, *Mater. Trans.* **52**, 974–978 (2011).
294. P. Xue, X. X. Zhang, L. H. Wu, and Z. Y. Ma, Research progress on friction stir welding and processing, *Acta Metallurg. Sinica* **52**, 1222–1238 (2016).
295. G. Ipekoglu and G. Cam, Effects of initial temper condition and postweld heat treatment on the properties of dissimilar friction-stir-welded joints between AA7075 and AA6061 aluminum Alloys, *Metall. Mater. Trans. A* **45A**, 3074–3087 (2014).
296. Y. Li, L. E. Murr, and J. C. McClure, Flow visualization and residual microstructures associated with the friction-stir welding of 2024 aluminum to 6061 aluminum, *Mater. Sci. Eng. A* **A271**, 213–223 (1999).
297. P. Cavaliere, R. Nobile, F. W. Panella, and A. Squillace, Mechanical and microstructural behaviour of 2024-7075 aluminium alloy sheets joined by friction stir welding, *Int. J. Mach. Tools Manuf.* (2005).
298. J. M. Tang and Y. F. Shen, Numerical simulation and experimental investigation of friction stir lap welding between aluminum alloys AA2024 and AA7075, *J. Alloys Cmpnd.* **666**, 493–500 (2016).
299. Y. F. Sun, N. Tsuji, and H. Fujii, Microstructure and mechanical properties of dissimilar friction Stir welding between ultrafine grained 1050 and 6061-T6 aluminum alloys, *Metals* **6**, 249 (2016).
300. S. Lim, Sangshik Kim, C. G. Lee, and Sungjoon Kim, Tensile behavior of friction-stir-welded A356-T6Al 6061-T651 bi-alloy plate, *Metall. Mater. Trans. A* **35A**, 2837–2843 (2004).
301. T. Luijendijk, Welding of dissimilar aluminium alloys, *J. Mater. Process. Technol.* **103**, 29–35 (2000).
302. M. J. Peel, A. Steuwer, P. J. Withers, T. Dickerson, Q. Shi, and H. Shercliff, Dissimilar friction stir welds in AA5083-AA6082. Part I process parameter effects on thermal history and weld properties, *Metall. Mater. Trans. A* **37A**, 2183–2193 (2006).
303. M. J. Peel, A. Steuwer, and P. J. Withers, Dissimilar friction stir welds in AA5083-AA6082. Part II process parameter effects on microstructure, *Metall. Mater. Trans. A* **37A**, 2195–2206 (2006).
304. M. Ahmadnia, S. Shahraki, and M. A. Kamarposhti, Experimental studies on optimized mechanical properties while dissimilar joining AA6061 and AA5010 in a

friction stir welding process, *Int. J. Adv. Manuf. Technol.* **87**, 2337–2352 (2016).

305. I. A. Kartsonakis, D. A. Dragatogiannis, E. P. Koumoulos, A. Karantonis, and C. A. Charitidis, Corrosion behaviour of dissimilar friction stir welded aluminium alloys reinforced with nanoadditives, *Mater. Des.* **102**, 56–67 (2016).
306. R. Palanivel, R. F. Laubscher, I. Dinaharan, and N. Murugan, Tensile strength prediction of dissimilar friction stir-welded AA6351-AA5083 using artificial neural network technique, *J. Braz. Soc. Mech. Sci. Eng.* **38**, 1647–1657 (2016).
307. V. X. Tran, J. Pan, and T. Pan, Effects of processing time on strengths and failure modes of dissimilar spot friction welds between aluminum 5754-O and 7075-T6 sheets, *J. Mater. Process. Technol.* **209**, 3724–3739 (2009).
308. A. Davoodi, Z. Esfahani, and M. Sarvghad, Microstructure and corrosion characterization of the interfacial region in dissimilar friction stir welded AA5083 to AA7023, *Corros. Sci.* **107**, 133–144 (2016).
309. I. K. Rec, M. Wrobel, and M. Kopyscianski, Investigations of friction stir welds between 5083 and 7075 aluminum alloys using EBSD and X-Ray techniques, *Acta Physica Polonica A* **130**, 996–999 (2016).
310. P. B. Srinivasan, W. Dietzel, R. Zettler, J. F. D. Santos, and V. Sivan, Stress corrosion cracking susceptibility of friction stir welded AA7075-AA6056 dissimilar joint, *Mater. Sci. Eng. A* **A392**, 292–300 (2005).
311. M. R. M. Aliha, M. Shahheidari, M. Bisadi, M. Akbari, and S. Hossain, Mechanical and metallurgical properties of dissimilar AA6061-T6 and AA7277-T6 joint made by FSW technique, *Int. J. Adv. Manuf. Technol.* **86**, 2551–2565 (2016).
312. L. Giraud, H. Robe, C. Claudin, C. Desrayaud, P. Bocher, and E. Feulvarch, Investigation into the dissimilar friction stir welding of AA7020-T651 and AA6060-T6, *J. Mater. Process. Technol.* **235**, 220–230 (2016).
313. H. J. Aval, Microstructure and residual stress distributions in friction stir welding of dissimilar aluminium alloys, *Mater. Des.* **87**, 405–413 (2015).
314. Z. Zhang, Comparison of two contact models in the simulation of friction stir welding process, *J. Mater. Sci.* **43**, 5867–5877 (2008).
315. Z. Zhang, Q. Wu, M. Grujicic, and Z. Y. Wan, Monte carlo simulation of grain growth and welding zones in friction stir welding of AA6082-T6, *J. Mater. Sci.* **51**, 1882–1895.
316. Z. Zhang, J. T. Chen, Z. W. Zhang, and H. W. Zhang, Coupled thermo-mechanical model based comparison of friction stir welding processes of AA2024-T3 in different thicknesses, *J. Mater. Sci.* **46**, 5815–5821 (2011).
317. Y. B. Zhong, C. S. Wu, and G. K. Padhy, Effect of ultrasonic vibration on welding load, temperature and material flow in friction stir welding, *J. Mater. Process. Technol.* **239**, 273–283 (2017).
318. A. A. McLean, G. L. F. Powell, I. H. Brown, and V. M. Linton, Friction stir welding of magnesium alloy AZ31B to aluminium alloy 5083, *Sci. Technol. Weld. Join.* **8**, 462–464 (2003).
319. R. Zettler, Dissimilar Al to Mg alloy friction stir welds, *Adv. Eng. Mater.* **8**, 415–421 (2006).
320. V. Firouzdor and S. Kou, Formation of liquid and intermetallics in Al-to-Mg friction stir welding, *Metall. Mater. Trans. A* **41A**, 3238–3251 (2010).
321. S. A. Khodir, M. M. Z. Ahmed, E. Ahmed, S. M. R. Mohamed, and H. Aleem, Effect of intermetallic compound phases on the mechanical properties of the dissimilar Al/Cu friction stir welded joints, *J. Mater. Eng. Perform.* **25**, 4637–4648 (2016).
322. P. K. Sahu, S. Pal, S. K. Pal, and R. Jain, Influence of plate position, tool offset and tool rotational speed on mechanical properties and microstructures of dissimilar Al/Cu friction stir welding joints, *J. Mater. Process. Technol.* **235**, 55–67 (2016).
323. P. Xue, B. L. Xiao, D. R. Ni, and Z. Y. Ma, Enhanced mechanical properties of friction stir welded dissimilar Al-Cu joint by intermetallic compounds, *Mater. Sci. Eng. A* **527**, 5723–5727 (2010).
324. S. V. Safi, H. Amirabadi, M. K. B. Givi, and S. M. Safi, The effect of preheating on mechanical properties of friction stir welded dissimilar joints of pure copper and AA7075 aluminum alloy sheets, *Int. J. Adv. Manuf. Technol.* **84**, 2401–2411 (2016).
325. P. Xue, B. L. Xiao, and Z. Y. Ma, Effect of interfacial microstructure evolution on mechanical properties and fracture behavior of friction-stir-welded Al-Cu joints, *Metall. Mater. Trans. A* **46A**, 3091–3103 (2015).
326. J. Q. Zhang, Y. F. Shen, X. Yao, H. S. Xu, and B. Li, Investigation on dissimilar underwater friction stir lap welding of 6061-T6 aluminum alloy to pure copper, *Mater. Des.* **64**, 74–80 (2014).
327. S. A. Hussein, A. S. M. Tahir, and A. B. Hadzley, Characteristics of aluminum-to-steel joint made by friction stir welding: A review, *Mater. Today Commun.* **5**, 32–49 (2015).
328. Q. X. Zheng, X. M. Feng, Y. F. Shen, G. Q. Huang, and P. C. Zhao, Dissimilar friction stir welding of 6061 Al to 316 stainless steel using Zn as a filler metal, *J. Alloys Cmpnd.* **686**, 693–701 (2016).
329. P. Kannan, K. Balamurugan, and K. Thirunavukkarasu, Influence of silver interlayer in dissimilar 6061-T6 aluminum MMC and AISI 304 stainless steel friction welds, *Int. J. Adv. Manuf. Technol.* **81**, 1743–1756 (2015).
330. M. Yılmaz, M. Çöl, and M. Acet, Interface properties of aluminum/steel friction-welded components, *Mater. Character.* **49**, 421–429 (2002).
331. T.-J. Yoon, B.-H. Jung, and C.-Y. Kang, The quantitative investigation of mechanical properties and characterization of fractured position for friction stir lap welded A6111/A5023, *Mater. Des.* **83**, 377–386 (2015).
332. M. R. Pishevar, H. Omidvar, J. A. Mohandesi, and M. A. Safarkhanian, Effect of applying second-pass welding and welding parameters on the defects and mechanical properties in friction-stir lap-welded AA5456 sheets, *Weld. World* **60**, 497–506 (2016).
333. Y. M. Yue, Z. W. Li, S. D. Ji, Y. X. Huang, and Z. L. Zhou, Effect of reverse-threaded pin on mechanical properties of friction stir lap welded alclad 2024 aluminum alloy, *J. Mater. Sci. Technol.* **32**, 671–675 (2016).
334. Y. C. Chen and K. Nakata, Friction stir lap joining aluminum and magnesium alloys, *Scripta Mater.* **58**, 433–436 (2008).

335. Y. X. Huang, J. C. Wang, L. Wan, X. C. Meng, H. B. Liu, and H. Li, Self-riveting friction stir lap welding of aluminum alloy to steel, *Mater. Lett.* **185**, 181–184 (2016).
336. J. Jeon, S. Mironov, Y. S. Sato, H. Kokawa, S. H. C. Park, and S. Hirano, Friction stir spot welding of single-crystal austenitic stainless steel, Acta Mater, **59**, 7439–7449 (2011).
337. G. D'Urso and C. Giardini, Thermo-mechanical characterization of friction stir spot welded AA7050 sheets by means of experimental and FEM analyses, *Materials* **9**, 689 (2016).
338. Y. Tozaki, Y. Uematsu, and K. Tokaji, A newly developed tool without probe for friction stir spot welding and its performance, *J. Mater. Process Technol.* **210**, 844–851 (2010).
339. P. Jedrasiak, H. R. Shercliff, A. Reilly, G. J. McShane, Y. C. Chen, L. Wang, J. Robson, and P. Prangnell, Thermal modeling of Al-Al and Al-Steel friction stir spot welding, *J. Mater. Eng. Perform.* **25**, 4089–4098 (2016).
340. H. S. Shin and Y. C. Jung, Characteristics of friction stir spot welding of Zr-based bulk metallic glass sheets, *J. Alloys Cmpnd.* **504**, S279–S282 (2010).
341. H. S. Shin, Tool geometry effect on the characteristics of dissimilar friction stir spot welded bulk metallic glass to lightweight alloys, *J. Alloys Cmpnd.* **586**(Supplement 1), S50–S55 (2014).
342. F. Lambiase, A. Paoletti, and A. Ilio, Effect of tool geometry on loads developing in friction stir spot welds of polycarbonate sheets, *Int. J. Adv. Manuf. Technol.* **87**, 2293–2303 (2016).
343. L. E. Murr, E. A. Trillo, S. Pappu, and C. Kennedy, Adiabatic shear bands and examples of their role in severe plastic deformation, *J. Mater. Sci.* **37**, 3337–3360 (2002).
344. C. Gallais, A. Simar, D. Fabregue, A. Denquin, G. Lapasset, B. D. Meester, Y. Brechet, and T. Pardoen, Multiscale analysis of the strength and ductility of AA 6056 aluminum friction stir welds, *Metall. Mater. Trans. A* **38A**, 964–981 (2007).
345. P. Heurtier, C. Desrayaud, and F. Montheillet, A thermomechanical analysis of the friction stir welding process, *Mater. Sci. Forum* **396–402**, 1537–1542 (2002).
346. K. O. Ishi and T. R. Mcnelley, Microstructural modification of as-cast NiAl bronze by friction stir processing, *Metall. Mater. Trans. A* **35A**, 2951–2961 (2004).
347. J. Q. Su, T. W. Nelson, and C. J. Sterling, A new route to bulk nanocrystalline materials, *J. Mater. Res.* **18**, 1757–1760 (2003).
348. C. G. Rhodes, M. W. Mahoney, W. H. Bingel, and M. Calabrese, Fine-grain evolution in friction-stir processed 7050 aluminum, *Scripta Mater.* **48**, 1451–1455 (2003).
349. S. M. Chowdhury, D. L. Chen, S. D. Bhole, and X. Cao, Tensile properties of a friction stir welded magnesium alloy: Effect of pin tool thread orientation and weld pitch, *Mater. Sci. Eng.* **527**, 6064–6075 (2010).
350. K. O. Ishi, A. P. Zhilyaev, and T. R. Mcnelley, A microtexture investigation of recrystallization during friction stir processing of as-cast NiAl bronze, *Metall. Mater. Trans. A* **37A**, 2239–2251 (2006).
351. W. B. Lee, C. Y. Lee, W. S. Chang, Y. M. Yeon, and S. B. Jung, Microstructural investigation of friction stir welded pure titanium, *Mater. Lett.* **59**, 3315–3318 (2005).
352. A. L. Pilchak, M. C. Juhas, and J. C. Williams, Microstructural changes due to friction stir processing of investment-cast Ti-6Al-4V, *Metall. Mater. Trans. A* **38A**, 401–408 (2007).
353. A. L. Etter, T. Baudin, N. Fredj, and R. Penelle, Recrystallization mechanisms in 5251 H14 and 5251 O aluminum friction stir welds, *Mater. Sci. Eng. A* **445–446**, 94–99 (2007).
354. O. Sitdikov and R. Kaibyshev, Dynamic recrystallization in pure magnesium, *Mater. Trans.* **42**, 1928–1937 (2001).
355. F. J. Humphreys and M. Hatherly, *Recrystallization and Related Annealing Phenomena*, 2nd ed., Elsevier Ltd., Oxford, UK (2004).
356. B. Radhakrishnan and G. Sarma, The effect of coarse non-deformable particles on the deformation and static recrystallization of aluminium alloys, *Philos. Mag.* **84**, 2341–2366 (2004).
357. A. M. Russell and K. L. Lee, *Structure–property Relations in Nonferrous Metals*, Wiley Interscience, John Wiley & Sons, Inc., Publication, Hoboken, New Jersey, (2005).
358. B. C. Ko and Y. C. Yoo, Prediction of dynamic recrystallization condition by deformation efficiency for Al 2024 composite reinforced with SiC particle, *J. Mater. Sci.* **35**, 4073–4077 (2000).
359. D. H. Sastry, Prasad, and K. I. Vasu, On the stacking fault energies of some close-packed hexagonal metals, *Scripta Metall.* **3**, 927–929 (1969).
360. G. Lutjering and J. C. Williams, *Titanium*, 2nd ed., Springer, Berlin (2007).
361. Z. Guo, A. P. Miodownik, N. Saunders, and J. P. Schillé, Influence of stacking-fault energy on high temperature creep of alpha titanium alloys, *Scripta Mater.* **54**, 2175–2178 (2006).
362. J. W.D. Callister and D. G. Rethwisch, *Materials Science and Engineering*, 9th ed., John Wiley & Sons, Hoboken, NJ (2014).
363. K. Colligan, Material flow behavior during friction welding of aluminum, *Weld. J.* **78**, 229–237 (1999).
364. Suhuddin, S. Mironov, Y. S. Sato, and H. Kokawa, Grain structure and texture evolution during friction stir welding of thin 6016 aluminum alloy sheets, *Mater. Sci. Eng. A* **527**, 1962–1969 (2010).
365. F. Montheillet, J. Lepinoux, D. Weygand, and E. Rauch, Dynamic and static recrystallization, *Adv. Eng. Mater.* **3**, 587–589 (2001).
366. R. D. Doherty, D. A. Hughes, F. J. Humphreys, J. J. Jonas, D. J. Jensen, M. E. Kassner, W. E. King, T. R. McNelley, H. J. McQueen, and A. D. Rollett, Current issues in recrystallization: a review, *Mater. Sci. Eng. A* **238**, 219–274 (1997).
367. W. Pantleon, On the statistical origin of disorientations in dislocation structures, *Acta Mater.* **46**, 451–456 (1998).
368. G. Liu, L. E. Murr, C. S. Niou, J. C. McClure, and F. R. Vega, Microstructural aspects of the friction-stir welding of 6061-T6 aluminum, *Scripta Mater.* **37**, 355–361 (1997).
369. L. Fratini and G. Buffa, Continuous dynamic recrystallization phenomena modelling in friction stir welding of aluminium alloys: A neural-network-based approach, *Proc. IMechE Part B: J. Eng. Manuf.* **221**, 857–864 (2007).
370. G. Buffa, L. Fratini, and R. Shivpuri, CDRX modelling in friction stir welding of AA7075-T6 aluminum alloy: Analytical approaches, *J. Mater. Process. Technol.* **191**, 356–359 (2007).

371. H. J. McQueen, O. Knustad, N. Ryum, and J. K. Solberg, Microstructural evolution in Al deformed to strains of 60 at 400°C, *Scripta Metall.* **19**, 73–78 (1985).
372. T. L. Giles, K. O. Ishi, A. P. Zhilyaev, S. Swaminathan, M. W. Mahoney, and T. R. McNelley, The effect of friction stir processing on the microstructure and mechanical properties of an aluminum lithium alloy, *Metall. Mater. Trans. A* **40A**, 104–115 (2009).
373. J. D. Robson and L. Campbell, Model for grain evolution during friction stir welding of aluminium alloys, *Sci. Technol. Weld. Join.* **15**, 171–176 (2010).
374. A. Gholinia, F. J. Humphreys, and P. B. Prangnell, Production of ultra-fine grain microstructures in Al-Mg alloys by coventional rolling, *Acta Mater.* **50**, 4461–4476 (2002).
375. F. J. Humphreys, P. B. Prangnell, J. R. Bowen, A. Gholinia, and C. Harris, Developing stable fine-grain microstructures by large strain deformation, *Phil. Trans. R. Soc. Lond. A* **357**, 1663–1681 (1999).
376. L. E. Murr, Twin boundary energetics in pure aluminium, *Acta Metall.* **21**, 791–797 (1973).
377. F. J. Humphreys and M. Ferry, On the role of twinning in the recrystallization of aluminium, *Scripta Mater.* **35**, 99–105 (1996).
378. R. W. K. Honeycombe, *The Plastic deformation of Metals*, Edward Arnold, London (1971).
379. O. Sitdikov, R. Kaibyshev, and T. Sakai, Dynamic recrystallization based on twinning in coarse-grained Mg, *Mater. Sci. Forum* **419–422**, 521–526 (2003).
380. R. O. Kaibyshev and O. S. Sitdikov, On the role of twinning in dynamic recrystallization, *Phys. Met. Metallogr.* **89**, 384–390 (2000).
381. S. E. Ion, F. J. Homphreys, and S. H. Wmoe, Dynamic recrystallisation and the development of microstructure during the high temperature deformation of magnesium, *Acta Metall.* **30**, 1909–1919 (1982).
382. A. Galiyev, R. Kaibyshev, and G. Gottstein, Correlation of plastic deformation and dynamic recrystallization in magnesium alloy ZK60, *Acta Mater.* **49**, 1199–1207 (2001).
383. R. O. Kaibyshev and O. S. Sitdikov, Structural changes during plastic deformation of pure magnesium, *Phys. Met. Metallogr.* **73**, 635 (1992).
384. Y. N. Wang and J. C. Huang, The role of twinning and untwinning in yielding behavior in hot-extruded Mg-Al-Zn alloy, *Acta Mater.* **55**, 897–905 (2007).
385. X. X. Xia and H. J. Mcqueen, Deformation behavior and microstructure of a 20% Al_2O_3 reinforced 6061 Al composite, *Appl. Compos. Mater.* **4**, 333–347 (1997).
386. B. Inem, Dynamic recrystallization in a thermomechanically processed metal matrix composite, *Mater. Sci. Eng. A* **197**, 91–95 (1995).
387. C. Barry Carter, M. Grant Norton, Ceramic Materials Sciences and Engineering, Springer Science + Business Media, LLC, 233 Spring Street, New York, NY 10013, USA, (2007).
388. R. E. R. Hill and R. Abbaschian, in, 3rd ed. Physical Metallurgy Principles. PWS–Kent Publishing Company, Boston (1992).
389. A. P. Gerlich and T. Shibayanagi, *Scripta Mater.* **60**, 236–239 (2009).
390. R. Kapoor, N. Kumar, R. S. Mishra, C. S. Huskamp, and K. K. Sankaran, Influence of fraction of high angle boundaries on the mechanical behavior of an ultrafine grained Al-Mg alloy, *Mater. Sci. Eng. A* **527**, 5246–5254 (2010).
391. R. S. Mishra and M. W. Mahoney, Friction stir processing: A new grain refinement technique to achieve high strain rate superplasticity in commercial alloys. In N. Chandra (Ed.) *Superplasticity in Advanced Materials, Icsam–2000* (2001) pp. 507–512.
392. A. F. Norman, I. Brough, and P. B. Prangnell, High resolution EBSD analysis of the grain structure in an AA2024 friction stir weld, *Mater. Sci. Forum* **331–337**, 1713–1718 (2000).
393. M. Eddahbi, T. R. Mcnelley, and O. A. Ruano, The evolution of grain boundary character during superplastic deformation of an Al-6 pct Cu-0.4 pct Zr alloy, *Metall. Mater. Trans. A* **32A**, 1093–1102 (2001).
394. J. Wang, Y. Iwahashi, Z. Horita, M. Furukawa, M. Nemoto, R. Z. Valiev, and T. G. Langdon, An investigation of microstructural stability in an Al-Mg alloy with submicrometer grain size, *Acta Mater.* **44**, 2973–2982 (1996).
395. R. Z. Valiev, A. V. Korznikov, and R. R. Mulyukov, Structure and properties of ultrafine-grained materials produced by severe plastic deformation, *Mater. Sci. Eng. A* **168**, 141–148 (1993).
396. S. H. Kang, W. H. Bang, J. H. Cho, H. N. Han, K. H. Oh, C. G. Lee, and S. J. Kim, Microtexture analysis of friction stir welded Al 6061-T651 plates, *Mater. Sci. Forum* **495–497**, 901–906 (2005).
397. J. K. Mackenzie, Second paper on statistics associated with the random disorientation of cubes, *Biometrika* **45**, 229–240 (1958).
398. F. C. Liu, Z. Y. Ma, and L. Q. Chen, Low-temperature superplasticity of Al-Mg-Sc alloy produced by friction stir processing, *Scripta Mater.* **60**, 968–971 (2009).
399. Y. Motohashi, T. Sakuma, A. Goloborodko, T. Ito, and G. Itoh, Grain refinement process in commercial 7075-T6 aluminum alloy under friction stir welding and superplasticity, *Mat.wiss.u. Werkstofftech.* **39**, 275–278 (2008).
400. S. Mironov, K. Masaki, Y. S. Sato, and H. Kokawa, Texture produced by abnormal grain growth in friction stir-welded aluminum alloy 1050, *Metall. Mater. Trans. A* **44A**, 1153–1157 (2013).
401. M. Cabibbo, A. Forcellese, M. Simoncini, M. Pieralisi, and D. Ciccarelli, Effect of welding motion and pre-/post-annealing of friction stir welded AA5754 joints, *Mater. Des.* **93**, 146–159 (2016).
402. F. Khodabakhshi, A. Simchi, A. H. Kokabi, A. P. Gerlich, and M. Nosko, Effects of post-annealing on the microstructure and mechanical properties of friction stir processed Al-Mg-TiO_2 nanocomposites, *Mater. Des.* **63**, 30–41 (2014).
403. X. G. Chen, M. Silva, P. Gougeon, and L. Georges, Microstructure and mechanical properties of friction stir welded AA6063-B4C metal matrix composites, *Mater. Sci. Eng. A* **518**, 174–184 (2009).
404. Y. J. Li, R. D. Fu, D. X. Du, L. J. Jing, D. L. Sang, and Y. P. Wang, Effect of post-weld heat treatment on microstructures and properties of friction stir welded joint of 32Mn-7Cr-1Mo-0.3N steel, *Sci. Technol. Weld. Join.* **20**, 229–235 (2015).

405. F. J. Humphreys, A unified theory of recovery, recrystallization and grain growth, based on the stability and growth of cellular microstructures-II.The effect of second-phase particles, *Acta Mater.* **45**, 5031–5039 (1997).
406. M. M. Attallah and H. G. Salem, Friction stir welding parameters a tool for controlling abnormal grain growth during subsequent heat treatment, *Mater. Sci. Eng.* **A391**, 51–59 (2005).
407. M. A. G. Bernal, R. S. Mishra, R. Verma, and D. H. Silva, Inhibition of abnormal grain growth during hot deformation behavior of friction stir processed 5083 Al alloys, *Mater. Sci. Eng. A* **636**, 326–330 (2015).
408. F. J. Humphreys, Stability and growth of grain and sturctures in two-phase materials, in: *Grain Growth in Polycrystalline Materials 3*, TMS, Warrendale (1998). p. 13.
409. S. Jana, R. S. Mishra, J. A. Baumann, and G. Grant, Effect of process parameters on abnormal grain growth during friction stir processing of a cast Al alloy, *Mater. Sci. Eng. A* **528**, 189–199 (2010).
410. Z. L. Hu, X. S. Wang, Q. Pang, F. Huang, X. P. Qin, and L. Hua, The effect of postprocessing on tensile property and microstructure evolution of friction stir welding aluminum alloy joint, *Mater. Character.* **99**, 180–187 (2015).
411. G. Ipekoglu, S. Erim, and G. Cam, Investigation into the influence of post-weld heat treatment on the friction stir welded AA6061 Al-alloy plates with different temper conditions, *Metall. Mater. Trans. A* **45A**, 864–877 (214).
412. H. Jin, S. Saimoto, M. Ball, and P. L. Threadgill, Characterisation of microstructure and texture in friction stir welded joints of 5754 and 5182 aluminium alloy sheets, *Mater. Sci. Technol.* **17**, 1605–1614 (2001).
413. Y. S. Sato, H. Kokawa, M. Enomoto, S. Jogan, and T. Hashimoto, Precipitation sequence in friction stir weld of 6063 aluminum during aging, *Metall. Mater. Trans. A* **30A**, 3125–3130 (1999).
414. H. Yoshida, The control of grain size particles in grain boundary for superplastic aluminum alloys, *Mater. Sci. Forum* **204–206** 657–666 (1996).
415. J. D. Verhoeven, *Fundamentals of Physical Metallurgy*, John Wiley & Sons, New York, 118–120 (1975).
416. L. F. Mondolfo, *Aluminum Alloys Structure and Properties*. England by William Clowes & Sons Limited Beccles and London (1979).
417. C. S. T. Chang and B. J. Duggan, Relationships between rolled grain shape, deformation bands, microstructures and recrystallization textures in Al-5%Mg, *Acta Mater.* **58**, 476–489 (2010).
418. L. E. Svensson, L. Karlsson, H. Larsson, B. Karlsson, and M. Fzaaini, Microstructure and mechanical properties of friciton stir welded aluminium alloys with special reference to AA5083 and AA6082, *Sci. Technol. Weld. Join.* **5**, 285–296 (2000).
419. P. Ratchev, B. Verlinden, and P. V. Houtte, Effect of preheat temperature on the orientation relationship of (Mn, Fe)Al6 precipitates in an AA 5182 Aluminium–Magnesium alloy, *Acta Metall. Mater* **43**, 621–629 (1995).
420. M. Imam, Y. F. Sun, H. Fujii, N. Ma, S. Tsutsumi, and H. Murakawa, Microstructural characteristics and mechanical properties of friction stir welded thick 5083 aluminum alloy, *Metall. Mater. Trans. A* **48**, 208–229 (2017).
421. J. Li, S. Saimoto, The role of solute segregation and precipitation at dislocations to enhance continuous recrystallization, *Mater. Sci. Eng. A* **234–236**, 1011–1014 (1997).
422. C. B. Fuller and M. W. Mahoney, The effect of friction stir processing on 5083-H321/5356 Al arc welds: Microstructural and mechanical analysis, *Metall. Mater. Trans. A* **37A**, 3605–3615 (2006).
423. F. Zhang, L. E. Levine, A. J. Allen, C. E. Campbell, A. A. Creuziger, N. Kazantseva, and J. Ilavsky, In situ structural characterization of ageing kinetics in aluminum alloy 2024 across angstrom-to-micrometer length scales, *Acta Mater.* **111**, 385–398 (2016).
424. H. B. Aaron and H. I. Aaronson, Growth of grain boundary precipitates in Al-4%Cu by interfacial diffusion, *Acta Metall.* **16**, 789–798 (1968).
425. R. N. Wilson and P. G. Partridge, The nucleation and growth of S' precipitates in an aluminium-2.5% copper-1.2% magnesium alloy, *Acta Metall.* **13**, 1321–1327 (1965).
426. L. Litynska, R. Braun, G. Staniek, C. D. Donne, and J. Dutkiewicz, TEM study of the microstructure evolution in a friction stir-welded AlCuMgAg alloy, *Mater. Chem. Phys.* **81**, 293–295 (2003).
427. F. F. Wang, W. Y. Li, J. Shen, S. Y. Hu, and J. F. Santos, *Mater. Des.* **86**, 933–940 (2015).
428. R. J. Rioja and J. Liu, The evolution of Al-Li base products for aerospace and space applications, *Metall. Mater. Trans. A* **43**, 3325–3337 (2012).
429. Y. Tao, D. R. Ni, B. L. Xiao, Z. Y. Ma, W. Wu, R. X. Zhang, and Y. S. Zeng, Origin of unusual fracture in stirred zone for friction stir welded 2198-T8 Al-Li alloy joints, *Mater. Sci. Eng. A* **693**, 1–13 (2017).
430. B. Cai, Z. Q. Zheng, D. Q. He, S. C. Li, and H. P. Li, Friction stir weld of 2060 Al-Cu-Li alloy: Microstructure and mechanical properties, *J. Alloys Cmpnd.* **649**, 19–27 (2015).
431. H. Sidhar and R. S. Mishra, Aging kinetics of friction stir welded Al-Cu-Li-Mg-Ag and Al-Cu-Li-Mg alloys, *Mater. Des.* **110**, 60–71 (2016).
432. H. J. Liu, Y. Y. Hu, C. Dou, and D. P. Sekulic, An effect of the rotation speed on microstructure and mechanical properties of the friction stir welded 2060-T8 Al-Li alloy, *Mater. Character.* **123**, 9–19 (2017).
433. I. G. Urrutia, M. A. M. Morris, and D. G. Morris, Contribution of microstructural parameters to strengthening in an ultrafine-grained Al-7% Si alloy processed by severe deformation, *Acta Mater.* **55**, 1319–1330 (2007).
434. I. A. Lopez, C. M. Zepeda, J. G. G. Reyes, A. M. Flores, J. S. Rodriguez, and L. B. Gomez, TEM microstructural characterization of melt-spun aged Al-6Si-3Cu-xMg alloys, *Mater. Character.* **58**, 509–518 (2007).
435. R. X. Li, R. D. Li, Y. H. Zhao, L. Z. He, C. X. Li, H. R. Guan, and Z. Q. Hu, Age-hardening behavior of cast Al-Si base alloy, *Mater. Lett.* **58**, 2096–2101 (2004).
436. Z. Y. Ma, S. R. Sharma, R. S. Mishra, Microstructural modification of as-cast Al-Si-Mg alloy by friction stir processing, *Metall. Mater. Trans. A* **37A** (2006) 3323–3336 (2006).
437. S. Jana, R. S. Mishra, J. B. Baumann, and G. Grant, Effect of friction stir processing on fatigue behavior of an investment cast Al-7Si-0.6 Mg alloy, *Acta Mater.* **58** (2010) 989–1003 (2010).

438. G. R. Cui, D. R. Ni, Z. Y. Ma, and S. X. Li, Effects of friction stir processing parameters and in situ passes on microstructure and tensile properties of Al-Si-Mg casting, *Metall. Mater. Trans. A* **45A**, 5318–5331 (2014).
439. C. Ravi and C. Wolverton, First-principles study of crystal structure and stability of Al-Mg-Si-(Cu) precipitates, *Acta Mater.* **52**, 4213–4227 (2004).
440. H. Tanihata, T. Sugawara, K. Matsuda, and S. Ikeno, Effect of casting and homogenizing treatment conditions on the formation of Al-Fe-Si intermetallic compounds in 6063 Al-Mg-Si alloys, *J. Mater. Sci.* **34**, 1205–1210 (1999).
441. A. L. Dons, E. K. Jensen, Y. Langsrud, E. Tromborg, and S. Brusethaug, The alstruc microstructure solidification model for industrial aluminum alloys, *Metall. Mater. Trans. A* **30A**, 2135–2146 (1999).
442. G. Sha, K. O'Reilly, B. Cantor, R. Hamerton, and J. Worth, Effect of grain refiner on intermetallic phase formation in directional solidification of 6xxx series wrought Al alloys, *Mater. Sci. Forum* **331–337**, 253–258 (2000).
443. T. S. Srivatsan, M. AlHajri, M. Petraroli, B. Hotton, and P. C. Lam, Influence of silicon carbide particulate reinforcement on quasi static and cyclic fatigue fracture behavior of 6061 aluminum alloy composites, *Mater. Sci. Eng. A* **325**, 202–214 (2002).
444. C. A. W. Olea, L. Roldo, J. F. D. Santos, and T. R. Strohaecker, A sub-structural analysis of friction stir welded joints in an AA6056 Al-alloy in T4 and T6 temper conditions, *Mater. Sci. Eng. A* **454–455**, 52–62 (2007).
445. J. E. Hatch, *Aluminum Properties and Physical Metallurgy*, ASM, Metals Park, OH (1984).
446. D. Lassance, D. Fabregue, F. Delannay, and T. Pardoen, Micromechanics of room and high temperature fracture in 6xxx Al alloys, *Prog. Mater. Sci.* **52**, 62–129 (2007).
447. K. Laue, *Extrusion: Process Machinery Tooling*, ASM International, Metals Park (Ohio) (1976).
448. E. A. Starke, Aluminium alloys of the 70's: Scientific solutions to engineering problems. An invited review, *Mater. Sci. Eng. A* **29**, 99–115 (1977).
449. D. J. Chakrabarti and D. E. Laughlin, Phase relations and precipitation in Al-Mg-Si alloys with Cu additions, *Prog. Mater. Sci.* **49**, 389–410 (2004).
450. M. A. V. Huis, J. H. Chen, M. H. F. Sluiter, and H. W. Zandbergen, Phase stability and structural features of matrix-embedded hardening precipitates in Al-Mg-Si alloys in the early stages of evolution, *Acta Mater.* **55**, 2183–2199 (2007).
451. J. H. Chen, E. Costan, M. A. V. Huis, Q. Xu, and H. W. Zandbergen, Atomic Pillar-based nanoprecipitates strengthen AlMgSi alloys, *Science* **312**, 416–419 (2006).
452. C. D. Marioara, S. J. Andersen, J. Jansen, and H. W. Zandbergen, Atomic model for GP-zones in a 6082 Al-Mg-Si system, *Acta Mater.* **49**, 321–328 (2001).
453. H. W. Zandbergen, S. J. Andersen, and J. Jansen, Structure determination of Mg_5Si_6 particles in Al by dynamic electron diffraction studies, *Science* **277**, 1221–1225 (1997).
454. C. D. Marioara, S. J. Andersen, J. Jansen, and H. W. Zandbergen, The influence of temperature and storage time at RT on nucleation of the β"phase in a 6082 Al-Mg-Si alloy, *Acta Mater.* **51**, 789–796 (2003).
455. M. H. Mulazimoglu, A. Zaluska, F. Paray, and J. E. Gruzleski, The effect of strontium on the Mg2Si precipitation process in 6201 aluminum alloy, *Metall. Mater. Trans. A* **28A**, 1289–1295 (1997).
456. M. A. V. Huis, J. H. Chen, H. W. Zandbergen, and M. H. F. Sluiter, Phase stability and structural relations of nanometer-sized, matrix-embedded precipitate phases in Al-Mg-Si alloys in the late stages of evolution, *Acta Mater.* **54**, 2945–2955 (2006).
457. G. A. Edwards, K. Stiller, G. L. Dunlop, and M. J. Couper, The precipitation sequence in Al-Mg-Si alloys, *Acta Mater.* **46**, 3893–3904 (1998).
458. C. D. Marioara, S. J. Andersen, H. W. Zandbergen, and R. Holmestad, The influence of alloy composition on precipitates of the Al-Mg-Si system, *Metall. Mater. Trans. A* **36A**, 691–702 (2005).
459. M. Murayama, K. Hono, M. Saga, and M. Kikuchi, Atom probe studies on the early stages of precipitation in Al-Mg-Si alloys, *Mater. Sci. Eng. A* **250**, 127–132 (1998).
460. N. U. Deshpande, A. M. Gokhale, D. K. Denzer, and J. Liu, Relationship between fracture toughness, fracture path, and microstructure of 7050 aluminum alloy: Part 1. Quantitative characterization, *Metall. Mater. Trans. A* **29A**, 1191–1201 (1998).
461. A. Raghavan, J. Y. Koo, J. W. Steeds, and B. K. Park, Microanalytical study of the heterogeneous phases in commercial Al-Zn-Mg-Cu alloys, *Metall Trans.* **16A**, 1925–1936 (1985).
462. C. W. Bartges, Evidence of η" or ordered zone formation in aluminum alloy 7075 from differential scanning calorimetry, *Scripta Metall Mater.* **28**, 1039–1042 (1993).
463. R. Bush, M. Kiyota, and C. Kiyota, Characterization of a friction Stir weld in aluminum alloy 7055 using microhardness, electrical conductivity, and differential scanning calorimetry (DSC), *Metall. Mater. Trans. A* **47A** (2016) 3522–3532 (2016).
464. M. Dumont, A. Steuwer, A. Deschamps, M. Peel, and P. J. Withers, Microstructure mapping in friction stir welds of 7449 aluminium alloy using SAXS, *Acta Mater.* **54**, 4793–4801 (2006).
465. K. A. A. Hassan, P. B. Prangnell, A. F. Norman, D. A. Price, and S. W. Williams, Effect of welding parameters on nugget zone microstructure and properties in high strength aluminium alloy friction stir welds, *Sci. Technol. Weld. Join.* **8**, 257–268 (2003).
466. G. R. Cui, Z. Y. Ma, and S. X. Li, Periodical plastic flow pattern in friction stir processed Al-Mg alloy, *Scripta Mater.* **58**, 1082–1085 (2008).
467. K. N. Krishnan, On the formation of onion rings in friction stir welds, *Mater Sci. Eng.* **A327**, 246–251 (2002).
468. J. A. Schneider and A. C. Nunes, Characterization of plastic flow and resulting microtextures in a friction stir weld, *Metall. Mater. Trans. A* **35B**, 777–783 (2004).
469. M. A. Sutton, B. Yang, A. P. Reynolds, and J. Yan, Banded microstructure in 2024-T351 and 2524-T351 aluminum friction stir welds Part II. Mechanical characterization, *Mater. Sci. Eng. A* **364** (2004) 66–74 (2004).
470. B. C. Yang, J. H. Yan, M. A. Sutton, and A. P. Reynolds, Banded microstructure in AA2024-T351 and AA2524-T351 aluminum friction stir welds: Part I. Metallurgical studies, *Mater. Sci. Eng. A* **364**, 55–65 (2004).

471. Y. Z. Zhou, W. Zhang, B. Q. Wang, and J. D. Guo, Ultrafine-grained microstructure in a Cu-Zn alloy produced by electropulsing treatment, *J. Mater. Res.* **18**, 1991–1997 (2003).
472. R. W. Fonda and J. F. Bingert, Texture variations in an aluminum friction stir weld, *Scripta Mater.* **57**, 1052–1055 (2007).
473. D. Texier, Y. Zedan, T. Amoros, E. Feulvarch, J. C. Stinville, and P. Bocher, Near-surface mechanical heterogeneities in a dissimilar aluminum alloys friction stir welded joint, *Mater. Des.* **108**, 217–229 (2016).
474. Z. Zhang, B. L. Xiao, and Z. Y. Ma, Effect of segregation of secondary phase particles and "S" line on tensile fracture behavior of friction stir-welded 2024Al-T351 joints, *Metall. Mater. Trans. A* **44A**, 4081–4097 (2013).
475. Y. S. Sato, F. Yamashita, Y. Sugiura, S. H. C. Park, and H. Kokawa, FIB-assisted TEM study of an oxide array in the root of a friction stir welded aluminium alloy, *Scipta Materialia* **50**, 365–369 (2004).
476. S. R. Ren, Z. Y. Ma, and L. Q. Chen, Effect of initial butt surface on tensile properties and fracture behavior of friction stir welded Al-Zn-Mg-Cu alloy, *Mater. Sci. Eng. A* **479**, 293–299 (2008).
477. Y. S. Sato, H. Takauchi, S. H. C. Park, and H. Kokawa, Characteristics of the kissing-bond in friction stir welded Al alloy 1050, *Mater. Sci. Eng. A* **405**, 333–338 (2005).
478. M. Tabatabaeipour, J. Hettler, S. Delrue, and K. Van Den Abeele, Non-destructive ultrasonic examination of root defects in friction stir welded butt-joints, *NDT & E Int.* **80**, 23–34 (2016).
479. N. Gey, P. Bocher, E. Uta, L. Germain, and M. Humbert, Texture and microtexture variations in a near-a titanium forged disk of bimodal microstructure, *Acta Mater.* **60**, 2647–2655 (2012).
480. W. Woo, H. Choo, D. W. Brown, S. C. Vogel, P. K. Liaw, and Z. Feng, Texture analysis of a friction stir processed 6061-T6 aluminum alloy using neutron diffraction, *Acta Mater.* **54**, 3871–3882 (2006).
481. M. M. Z. Ahmed, B. P. Wynne, W. M. Rainforth, and P. L. Threadgill, Quantifying crystallographic texture in the probe-dominated region of thick-section friction-stir-welded aluminium, *Scripta Mater.* **59**, 507–510 (2008).
482. Y. Hovanski and T. W. Nelson, Characterization and prediction of deformation texture inherent in friction stir welding, in *Proc. from Joining of Advanced and Specialty Materials*, ASM International, St. Louis, MO, October 9–11, 2000. pp. 167–171.
483. S. H. C. Park, Y. S. Sato, and H. Kokawa, Effect of microtexture on fracture location in friction stir weld of Mg alloy AZ61 during tensile test, *Scripta Mater.* **49**, 161–166 (2003).
484. P. S. Pao, S. J. Gill, C. R. Feng, and K. K. Sankaran, Corrosion-fatigue crack growth in friction stir welded Al 7050, *Scripta Mater.* **45**, 605–612 (2001).
485. N. Akhtar and S. J. Wu, Macromechanics study of stable fatigue crack growth in Al-Cu-Li-Mg-Ag alloy, *Fatigue Fract. Eng. Mater. Struct.* **40**, 233–244 (2017).
486. D. Zhemchuzhnikova, S. Mironov, and R. Kaibyshev, Fatigue Performance of Friction-Stir-Welded Al-Mg-Sc Alloy, *Metall. Mater. Trans. A* **48A**, 150–158 (2017).
487. W. F. Xu, J. H. Liu, D. L. Chen, G. H. Luan, and J. S. Yao, Improvements of strength and ductility in aluminum alloy joints via rapid cooling during friction stir welding, *Mater. Sci. Eng. A* **548A**, 89–98 (2012).
488. R. W. Fonda and J. F. Bingert, Microstructural evolution in the heat-affected zone of a friction stir weld, *Metall. Mater. Trans. A* **35A**, 1487–1499 (2004).
489. M. F. Ashby and D. R. H. Jones, *Engineering Materials* **1**, Pergamon Press, Oxford, p. 105 (1980).
490. S. C. Tjong and H. Chen, Nanocrystalline materials and coatings, *Mater. Sci. Eng.* **R 45**, 1–88 (2004).
491. M. Furukawa, Y. Iwahashi, Z. Horita, M. Nemoto, N. K. Tsenev, R. Z. Valiev, and T. G. Langdon, Structural evolution and the Hall-Petch relationship in an Al-Mg-Li-Zr alloy with ultra-fine grain size, *Acta Mater.* **45**, 4751–4757 (1997).
492. H. Fujita and T. Tabata, The effect of grain size and deformation sub-structure on mechanical properties of polycrystalline aluminum, *Acta Metall.* **21**, 355–365 (1973).
493. N. Hansen, The effect of grain size and strain on the tensile flow stress of aluminium at room temperature, *Acta Metall.* **25**, 863–869 (1977).
494. G. R. Cui, Z. Y. Ma, and S. X. Li, The origin of non-uniform microstructure and its effects on the mechanical properties of a friction stir processed Al-Mg alloy, *Acta Mater.* **57**, 5718–5729 (2009).
495. Y. S. Sato, M. Urata, H. Kokawa, and K. Ikeda, Hall-Petch relationship in friction stir welds of equal channel angular-pressed aluminium alloys, *Mater. Sci. Eng. A* **354**, 298–305 (2003).
496. H. Hasegawa, S. Komura, A. Utsunomiya, Z. Horita, M. Furukawa, M. Nemoto, and T. G. Langdon, Thermal stability of ultrafine-grained aluminum in the presence of Mg and Zr additions, *Mater. Sci. Eng. A* **265**, 188–196 (1999).
497. M. Fairman, N. Afrin, D. L. Chen, X. J. Cao, and M. Jahazi, Microstructural evaluation of friction stir processed AZ31B-H24 magnesium alloy, *Can. Metall. Quart.* **46**, 425–432 (2007).
498. J. Luo, S. X. Li, W. Chen, J. F. Xiang, and H. Wang, Simulation of aluminum alloy flowing in friction stir welding with a multiphysics field model, *Int. J. Adv. Manuf. Technol.* **81**, 349–360 (2015).
499. M. Paidar, A. Khodabandeh, M. L. Sarab, and M. Taheri, Effect of welding parameters (plunge depths of shoulder, pin geometry, and tool rotational speed) on the failure mode and stir zone characteristics of friction stir spot welded aluminum 2024-T3 sheets, *J. Mech. Sci. Technol.* **29**, 4639–4644 (2015).
500. A. S. Golezani, R. V. Barenji, A. Heidarzadeh, and H. Pouraliakbar, Elucidating of tool rotational speed in friction stir welding of 7020-T6 aluminum alloy, *Int. J. Adv. Manuf. Technol.* **81**, 1155–1164 (2015).
501. M. Dhondt, I. Aubert, N. Saintier, and J.-M. Olive, Mechanical behavior of periodical microstructure induced by friction stir welding on Al-Cu-Li 2050 alloy, *Mater. Sci. Eng. A* **644**, 69–75 (2015).
502. S. Malopheyev, I. Vysotskiy, V. Kulitskiy, S. Mironov, and R. Kaibyshev, Optimization of processing-microstructure-properties relationship in friction-stir welded 6061-T6 aluminum alloy, *Mater. Sci. Eng. A* **662**, 136–143 (2016).
503. T. Hirata, T. Oguri, H. Hagino, T. Tanaka, S. W. Chung, Y. Takigawa, and K. Higashi, Influence of friction stir

welding parameters on grain size and formability in 5083 aluminum alloy, *Mater. Sci. Eng. A* **456**, 344–349 (2007).

504. S. S. Sabari, S. Malarvizhi, and V. Balasubramanian, The effect of pin profiles on the microstructure and mechanical properties of underwater friction stir welded AA2519-T87 aluminium alloy, *Int. J. Mech. Mater. Eng.* **11**(2016).
505. F. Heirani, A. Abbasi, and M. Ardestani, Effects of processing parameters on microstructure and mechanical behaviors of underwater friction stir welding of Al5083 alloy, *J. Manufact. Process.* **25**, 77–84 (2017).
506. Q. Z. Wang, Z. X. Zhao, Y. Zhao, K. Yan, and H. Zhang, The adjustment strategy of welding parameters for spray formed 7055 aluminum alloy underwater friction stir welding joint, *Mater. Des.* **88**, 1366–1376 (2015).
507. F. Rui–dong, S. Zeng–qiang, S. Rui–cheng, L. Ying, L. Hui–jie, and L. Lei, Improvement of weld temperature distribution and mechanical properties of 7050 aluminum alloy butt joints by submerged friction stir welding, *Mater. Des.* **32**, 4825–4831 (2011).
508. F. L, B. G, S. R, In-process heat treatments to improve FS-welded butt joints, *Int. J. Adv. Manuf. Technol.* **43**, 664–670 (2009).
509. Z. Zhang, B. L. Xiao, and Z. Y. Ma, Influence of water cooling on microstructure and mechanical properties of friction stir welded 2014Al-T6 joints, *Mater. Sci. Eng. A* **614**, 6–15 (2014).
510. Z. Zhang, B. L. Xiao, and Z. Y. Ma, Enhancing mechanical properties of friction stir welded 2219Al-T6 joints at high welding speed through water cooling and post-welding artificial ageing, *Mater. Character.* **106**, 255–265 (2015).
511. H. B. Chen, K. Yan, T. Lin, S. B. Chen, C. Y. Jiang, and Y. Zhao, The investigation of typical welding defects for 5456 aluminum alloy friction stir welds, *Mater. Sci. Eng. A* **433**, 64–69 (2006).
512. H. J. Liu, Y. C. Chen, and J. C. Feng, Effect of zigzag line on the mechanical properties of friction stir welded joints of an Al-Cu alloy, *Scripta Materialia* **55**, 231–234 (2006).
513. Y. Chen, H. Ding, Z.H. Cai, J. W. Zhao, J. Z. Li, Microstructural and mechanical characterization of a dissimilar friction stir-welded AA5083-AA7B04 butt joint, J Mater. Eng. Performance, 26, 530–539 (2017).
514. H. B. Chen, J. F. Wang, G. D. Zhen, S. B. Chen, and T. Lin, Effects of initial oxide on microstructural and mechanical properties of friction stir welded AA2219 alloy, *Mater. Des.* **86**, 49–54 (2015).
515. T. G. Nieh, J. Wadsworth, and O. D. Sherby, Superplasticity in metals and ceramics, Cambridge University Press, Cambridge, UK (1997).
516. T. G. Langdon, The mechanical properties of superplastic materials, *Metall. Trans.* **13A**, 689–701 (1982).
517. Z. Y. Ma, R. S. Mishra, M. W. Mahoney, and R. Grimes, Effect of friction stir processing on the kinetics of superplastic deformation in an Al-Mg-Zr alloy, *Metall. Mater. Trans. A* **36A**, 1447–1458 (2005).
518. H. Watanabe, T. Mukai, M. Mabuchi, and K. Higashi, High-strain-rate superplasticity at low temperature in a ZK61 magnesium alloy produced by powder metallurgy, *Scripta Mater.* **41**, 209–213 (1999).
519. R. Verma, A. K. Ghosh, S. Kim, and C. Kim, Grain refinement and superplasticity in 5083 Al, *Mater. Sci. Eng. A* **191**, 143–150 (1995).
520. K. T. Park, H. J. Lee, C. S. Lee, W. J. Nam, and D. H. Shin, Enhancement of high strain rate superplastic elongation of a modified 5154 Al by subsequent rolling after equal channel angular pressing, *Scripta Mater.* **51**, 479–483 (2004).
521. V. V. Patel, V. Badheka, and A. Kumar, Friction stir processing as a novel technique to achieve superplasticity in aluminum alloys: Process variables, variants, and applications, *Metallogr. Microstruct. Anal.* **5**, 278–293 (2016).
522. Z. Y. Ma and R. S. Mishra, in Friction Stir Superplasticity for Unitized Structures, Elsevier, Waltham, MA (2014).
523. R. K. Islamgaliev, N. F. Yunusova, R. Z. Valiev, N. K. Tsenev, V. N. Perevezentsev, and T. G. Langdon, Microstructure and retention of superplasticity of friction stir welded superplastic 2095 sheet, *Scripta Mater.* **49**, 467–472 (2003).
524. H. G. Salem, A. P. Reynolds, and J. S. Lyons, Microstructure and retention of superplasticity of friction stir welded superplastic 2095 sheet, *Scripta Mater.* **46**, 337–342 (2002).
525. M. M. Attallah and H. G. Salem, Influence of process parameters on superplasticity of friction stir processed nugget in high strength Al-Cu-Li alloy, *Mater Sci Technol* **20**, 1370–1376 (2004).
526. Z. Y. Ma, R. S. Mishra, and M. W. Mahoney, Superplasticity in cast A356 induced via friction stir processing, *Scripta Mater.* **50**, 931–935 (2004).
527. I. Charit and R. S. Mishra, Evaluation of microstructure and superplasticity in friction stir processed 5083 Al alloy, *J. Mater. Res.* **19**, 3329–3342 (2004).
528. L. B. Johannes, I. Charit, R. S. Mishra, and R. Verma, Enhanced superplasticity through friction stir processing in continuous cast AA5083 aluminum, *Mater. Sci. Eng. A* **464**, 351–357 (2007).
529. P. Ganesh and V. S. S. Kumar, Superplastic forming of friction stir welded AA6061-T6 alloy sheet with various tool rotation speed, *Mater. Manuf. Process.* **30**, 1080–1089 (2015).
530. A. Dutta, I. Charit, L. B. Johanners, and R. S. Mishra, Deep cup forming by superplastic punch stretching of friction stir processed 7075 Al alloy, *Mater. Sci. Eng. A* **A395**, 173–179 (2005).
531. Z. Y. Ma, R. S. Mishra, M. W. Mahoney, and R. Grimes, High strain rate superplasticity in friction stir processed Al-Mg-Zr alloy, *Mater. Sci. Eng. A* **A351**, 148–153 (2003).
532. K. Wang, F. C. Liu, Z. Y. Ma, and F. C. Zhang, Realization of exceptionally high elongation at high strain rate in a friction stir processed Al-Zn-Mg-Cu alloy with the presence of liquid phase, *Scripta Mater.* **64**, 572–575 (2011).
533. Z. Y. Ma, F. C. Liu, and R. S. Mishra, Superplastic deformation mechanism of an ultrafine-grained aluminum alloy produced by friction stir processing, *Acta Mater.* **58**, 4693–4704 (2010).
534. F. C. Liu and Z. Y. Ma, Achieving exceptionally high superplasticity at high strain rates in a micrograined Al-Mg-Sc alloy produced by friction stir processing, *Scripta Mater.* **59**, 882–885 (2008).

535. X. G. Jiang, J. Z. Cui, and L. X. Ma, The influence of the rolling direction on the mechanical behavior and cavity formation during superplastic deformation of 7075 A1 alloy, *Acta Metall. Mater.* **41**, 2721–2727 (1993).
536. F. C. Liu and Z. Y. Ma, Low-temperature superplasticity of friction stir processed Al-Zn-Mg-Cu alloy, *Scripta Mater.* **58**, 667–670 (2008).
537. K. T. Park, D. Y. Hwang, S. Y. Chang, and D. H. Shin, Low-temperature superplastic behavior of a submicrometer-grained 5083 Al alloy fabricated by severe plastic deformation, *Metall. Mater. Trans. A* **33A**, 2859–2867 (2002).
538. K. T. Park, D. Y. Hwang, Y. K. Lee, Y. K. Kim, and D. H. Shin, High strain rate superplasticity of submicrometer grained 5083 Al alloy containing scandium fabricated by severe plastic deformation, *Mater. Sci. Eng. A* **341**, 273–281 (2003).
539. I. C. Hsiao and J. C. Huang, Deformation mechanisms during low-and high-temperature superplasticity in 5083 Al-Mg alloy, *Metall. Mater. Trans. A* **33A**, 1373–1384 (2002).
540. H. P. Pu, F. C. Liu, and J. C. Huang, Characterization and analysis of low-temperature superplasticity in 8090 Al-Li alloys, *Metall. Mater. Trans. A* **26**, 1153–1166 (1995).
541. F. C. Liu and Z. Y. Ma, Contribution of grain boundary sliding in low-temperature superplasticity of ultrafine-grained aluminum alloys, *Scripta Mater.* **62**, 125–128 (2010).
542. R. S. Mishra, T. R. Bieler, and A. K. Mukherjee, Superplasticity in powder metallurgy aluminum alloys and composites, *Acta Metal. Mater.* **43**, 877–891 (1995).
543. M. G. Zelin and A. K. Mukherjee, Cooperative phenomena at grain boundaries during superplastic flow, *Acta Metal. Mater.* **43**, 2359–2372 (1995).
544. M. N. James, G. R. Bradley, H. Lombard, and D. G. Hattingh, The relationship between process mechanisms and crack paths in friction stir welded 5083-H321 and 5383-H321 aluminium alloys, *Fatigue Fract. Eng. Mater. Struct.* **28**, 245–256 (2005).
545. H. Lombard, D. G. Hattingh, A. Steuwer, and M. N. James, Optimising FSW process parameters to minimise defects and maximise fatigue life in 5083-H321 aluminium alloy, *Eng. Fract. Mechan.* **75**, 341–354 (2008).
546. M. N. James, D. G. Hattingh, and G. R. Bradley, Weld tool travel speed effects on fatigue life of friction stir welds in 5083 aluminium, *Int. J. Fatigue* **25**, 1389–1398 (2003).
547. M. Ericsson, L. Z. Jin, and R. Sandstrom, Fatigue properties of friction stir overlap welds, *Int. J. Fatigue* **29**, 57–68 (2007).
548. M. Ericsson and R. Sandstrom, Influence of welding speed on the fatigue of friction stir welds, and comparison with MIG and TIG, *Int. J. Fatigue* **25**, 1379–1387 (2003).
549. V. X. Tran, J. Pan, and T. Pan, Fatigue behavior of spot friction welds in lap-shear and cross-tension specimens of dissimilar aluminum sheets, *Int. J. Fatigue* **32**, 1022–1041 (2010).
550. V. X. Tran and J. Pan, Fatigue behavior of dissimilar spot friction welds in lap-shear and cross-tension specimens of aluminum and steel sheets, *Int. J. Fatigue* **32**, 1167–1179 (2010).
551. M. M. Shahri and R. Sandstrom, Fatigue analysis of friction stir welded aluminium profile using critical distance, *Int. J. Fatigue* **32**, 302–309 (2010).
552. C. Vidal, V. Infante, and P. Vilaca, Fatigue behavior in friction stir welded joints of AA2024 treated by improvement techniques, *Weld. World* **53**, 241–246 (2009).
553. S. Jana, R. S. Mishra, J. B. Baumann, and G. Grant, Effect of stress ratio on the fatigue behavior of a friction stir processed cast Al-Si-Mg alloy, *Scripta Mater.* **61**, 992–995 (2009).
554. S. S. Kim, C. G. Lee, and S. J. Kim, Fatigue crack propagation behavior of friction stir welded 5083-H32 and 6061-T651 aluminum alloys, *Mater. Sci. Eng. A* **478**, 56–64 (2008).
555. S. Hong, S. Kim, C. G. Lee, and S. J. Kim, Fatigue crack propagation behavior of friction stir welded 5083-H32 Al alloy, *J. Mater. Sci.* **42**, 9888–9893 (2007).
556. E. Kreyszig, H. Kreyszig, and E. J. Norminton, *Advanced Engineering Mathematics*, 10th ed., John Wiley & Sons, Inc., Hoboken, NJ (2011).
557. R. W. Fonda, P. S. Pao, H. N. Jones, C. R. Feng, B. J. Connolly, and A. J. Davenport, Davenport, microstructure, mechanical properties, and corrosion of friction stir welded Al 5456, *Mater. Sci. Eng. A* **519**, 1–8 (2009).
558. A. Tajiri, Y. Uematsu, T. Kakiuchi, and Y. Suzuki, Fatigue crack paths and properties in A356-T6 aluminum alloy microstructurally modified by friction stir processing under different conditions, *Frattura Ed Integrita Strutturale*, **34**, 347–354 (2015).
559. A. C. de. O. Miranda, A. Gerlich, and S. Walbridge, Aluminum friction stir welds: Review of fatigue parameter data and probabilistic fracture mechanics analysis, *Eng. Fract. Mechan.* **147**, 243–260 (2015).
560. L. Ceschini, I. Boromei, G. Minak, A. Morri, and F. Tarterini, Effect of friction stir welding on microstructure, tensile and fatigue properties of the AA7005/10 vol.%Al_2O_3p composite, *Compos. Sci. Tech.* **67**, 605–615 (2007).
561. M. Czechowski, Low-cycle fatigue of friction stir welded Al-Mg alloys, *J. Mater. Process Technol.* **164–165**, 1001–1006 (2005).
562. C. Li, A. H. Feng, X. J. Gu, and D. L. Chen, Localized cyclic strain measurements of friction stir welded aluminum alloy using a flat-clad optical fiber sensor array, *IEEE Sens. J.* **10**, 888–892 (2010).
563. W. F. Xu, J. H. Liu, D. L. Chen, and G. H. Luan, Low-cycle fatigue of a friction stir welded 2219-T62 aluminum alloy at different welding parameters and cooling conditions, *Int. J. Adv. Manuf. Technol.* **74**, 209–218 (2014).
564. W. F. Xu, J. H. Liu, D. L. Chen, G. H. Luan, and J. S. Yao, Change of microstructure and cyclic deformation behavior along the thickness in a friction-stir-welded aluminum alloy, *Scripta Mater.* **66**, 5–8 (2012).
565. N. E. Dowling, *Mechanical Behavior of Materials: Engineering Methods for Deformation, Fracture, and Fatigue*, Pearson-Prentice Hall, Upper Saddle River, NJ (2005).
566. W. Wang, K. Qiao, J. L. Wu, T. Q. Li, J. Cai, and K. S. Wang, Fatigue properties of friction stir welded joint of ultrafine-grained 2024 aluminium alloy, *Sci. Technol. Weld. Join.* **22**, 110–119 (2017).
567. D. Burford, C. Widener, and B. Tweedy, Advances in friction stir welding for aerospace applications, *Airframer*, 3–7 (2006).
568. D. G. Sanders, M. Ramulu, and P. D. Edwards, Mat. wiss. u. Werkstofftech., **39**, 353–357 (2008).

569. L. N. Brewer, M. S. Bennett, B. W. Baker, E. A. Payzant, and L. M. Kolbus, Characterization of residual stress as a function of friction stir welding parameters in oxide dispersion strengthened (ODS) steel MA956, *Mater. Sci. Eng. A* **647**, 313–321 (2015).
570. L. Q. Wang, J. Qu, L. Y. Chen, Q. Meng, L. Zhang, J. N. Qin, D. Zhang, and W. J. Lu, Investigation of Deformation Mechanisms in beta-Type Ti-35Nb-2Ta-3Zr Alloy via FSP Leading to Surface Strengthening, *Metall. Mater. Trans. A* **46A**, 4813–4818 (2015).
571. W. F. Xu, J. H. Liu, H. Q. Zhu, and L. Fu, Influence of welding parameters and tool pin profile on microstructure and mechanical properties along the thickness in a friction stir welded aluminum alloy, *Mater. Des.* **47**, 599–606 (2013).
572. W. F. Xu, J. H. Liu, and H. Q. Zhu, A study on the hardness and elastic modulus of friction stir welded aluminum alloy thick plate joints using micro-indentation, *J. Mater. Sci.* **46**, 1161–1166 (2011).
573. W. F. Xu, J. H. Liu, G. H. Luan, and C. L. Dong, Microstructure and mechanical properties of friction stir welded joints in 2219-T6 aluminum alloy, *Mater. Des.* **30**, 3460–3467 (2009).
574. F. Cioffi, J. I. Hidalgo, R. Fernández, T. Pirling, B. Fernández, D. Gesto, I. P. Orench, P. Rey, and G. G. Doncel, Analysis of the unstressed lattice spacing, d0, for the determination of the residual stress in a friction stir welded plate of an age-hardenable aluminum alloy – Use of equilibrium conditions and a genetic algorithm, *Acta Mater.* **74**, 189–199 (2014).
575. M. M. Z. Ahmed, B. P. Wynne, M. M. El–Sayed Seleman, and W. M. Rainforth, A comparison of crystallographic texture and grain structure development in aluminum generated by friction stir welding and high strain torsion, *Mater. Des.* **103**, 259–267 (2016).
576. M. Esmaily, N. Mortazavi, W. Osikowicz, H. Hindsefelt, J. E. Svensson, M. Halvarsson, J. Martin, and L. G. Johansson, Bobbin and conventional friction stir welding of thick extruded AA6005-T6 profiles, *Mater. Des.* **108**, 114–125 (2016).
577. J. He, Z. M. Ling, and H. M. Li, Effect of tool rotational speed on residual stress, microstructure, and tensile properties of friction stir welded 6061-T6 aluminum alloy thick plate, *Int. J. Adv. Manuf. Technol.* **84**, 1953–1961 (2016).
578. W. F. Xu and J. H. Liu, Microstructure evolution along thickness in double-side friction stir welded 7085 Al alloy, *Trans. Nonferr. Met. Soc. China* **25**, 3212–3222 (2015).
579. W. F. Xu, J. H. Liu, and D. L. Chen, Influence of test temperature on the tensile properties along the thickness in a friction stir welded aluminum alloy, *J. Mater. Sci. Technol.* **31**, 953–961 (2015).
580. S. D. Ji, Z. W. Li, Y. Wang, and L. Ma, Joint formation and mechanical properties of back heating assisted friction stir welded Ti-6Al-4V alloy, *Mater. Des.* **113**, 37–46 (2017).
581. S. S. Sahari, S. Malarvizhi, and V. Balasubramanian, Characteristics of FSW and UWFSW joints of AA2519-T87 aluminium alloy: Effect of tool rotation speed, *J. Manufact. Process.* **22**, 278–289 (2016).
582. S. D. Ji, Z. W. Li, L. G. Zhang, Z. L. Zhou, and P. Chai, Effect of lap configuration on magnesium to aluminum friction stir lap welding assisted by external stationary shoulder, *Mater. Des.* **103**, 160–170 (2016).
583. L. Shi, C. S. Wu, and H. J. Liu, Analysis of heat transfer and material flow in reverse dual-rotation friction stir welding, *Weld. World* **59**, 629–638 (2015).
584. Y. Morisada, H. Fujii, T. Mizuno, G. Abe, T. Nagaoka, and M. Fukusumi, Nanostructured tool steel fabricated by combination of laser melting and friction stir processing, *Mater. Sci. Eng. A* **505**, 157–162 (2009).
585. S. Kumar, Ultrasonic assisted friction stir processing of 6063 aluminum alloy, *Arch. Civil Mech. Eng.* **16**, 473–484 (2016).
586. G. K. Padhy, C. S. Wu, and S. Gao, Subgrain formation in ultrasonic enhanced friction stir welding of aluminium alloy, *Mater. Lett.* **183**, 34–39 (2016).
587. L. Shi, C. S. Wu, S. Gao, and G. K. Padhy, Modified constitutive equation for use in modeling the ultrasonic vibration enhanced friction stir welding process, *Scripta Mater.* **119**, 21–26 (2016).
588. J. Schwinn, M. Besel, and U. Mercado, Experimental determination of accurate fatigue crack growth data in tailored welded blanks, *Eng. Fract. Mechan.* **163**, 141–159 (2016).
589. T. Taavitsainen, P. Vilaca, and T. Mutanen, Production by FSW of free-shape hollow box profile in AA5754 for automotive application, *Weld World* **60**, 1121–1131 (2016).
590. E. Maggiolini, R. Tovo, L. Susmel, M. N. James, and D. G. Hattingh, Crack path and fracture analysis in FSW of small diameter 6082-T6 aluminium tubes under tension–torsion loading, *Int. J. Fatigue* **92**, 478–487 (2016).
591. M. Guillo and L. Dubourg, Impact & improvement of tool deviation in friction stir welding: Weld quality & real-time compensation on an industrial robot, *Robot. Comput.-Integr. Manufact.* **39**, 22–31 (2016).
592. J. Qin, F. Leonard, and G. Abba, Real-Time trajectory compensation in robotic friction stir welding using state estimators, *IEEE Trans. Control. Syst. Technol.* **24**, 2207–2214 (2016).
593. N. Mendes, P. Neto, M. A. Simao, A. Loureiro, and J. N. Pires, A novel friction stir welding robotic platform: welding polymeric materials, *Int. J. Adv. Manuf. Technol.* **85**, 37–46 (2016).
594. Y. Q. Mao, L. M. Ke, C. P. Huang, F. C. Liu, and Q. Liu, Formation characteristic, microstructure, and mechanical performances of aluminum-based components by friction stir additive manufacturing, *Int. J. Adv. Manuf. Technol.* **83**, 1637–1647 (2016).
595. W. F. Xu, W. Zhang, and X. L. Wu, Corrosion behavior of top and bottom surfaces for single-side and double-side friction stir welded 7085-T7651 aluminum alloy thick plate joints, *Metall. Mater. Trans. A* **48A**, 1078–1091 (2017).
596. W. F. Xu and J. H. Liu, Microstructure and pitting corrosion of friction stir welded joints in 2219-O aluminum alloy thick plate, *Corros. Sci.* **51**, 2743–2751 (2009).
597. M. Esmaily, J. E. Svensson, and L. G. Johansson, Technical note: A major loss in tensile strength of friction stir welded aluminum alloy joints resulting from atmospheric corrosion, *Corrosion* **72**, 1587–1596 (2016).
598. P. Atz Dick, G. H. Knörnschild, and L. F. P. Dick, Anodising and corrosion resistance of AA 7050 friction stir welds, *Corros. Sci.* **114**, 28–36 (2017).